Simulation of Friction and Wear Using the Method of Dimensionality Reduction

vorgelegt von

Master für Ingenieurwesen Qiang Li

aus Shanxi, V.R. China

von der

Fakultät V Verkehrs- und Machinensysteme

der Technischen Universität Berlin

zur Erlangung des akademisches Grades

Doktor der Ingenieurwissenschaften (Dr.-Ing)

genehmigte Dissertation

Promotionsausschuss

Vorsitzender: Univ.-Prof. Dr.-Ing. habil. Manfred W. Zehn

Gutachter: Univ.-Prof. Dr. rer. nat. Valentin L. Popov

Gutachter: Prof. Dr. Alexander E. Filippov

Tag der wissenschaftlichen Aussprache: 09.Oktober 2014

Berlin 2014

D83

Acknowledgement

The work presented in this thesis was carried out at the Department of System Dynamics and the Physics of Friction in the Technische Universität Berlin. This thesis would not have been possible without the help and support of many people. I would like to express my sincere gratitude to all of them.

I would like to first offer my gratitude to my supervisor, Prof. Valentin L. Popov. In the past four years he gave me lots of support, from the initial providing the opportunity to study in Germany, German learning, countless invaluable expert guidance to scientific research, and the final thesis writing. Without him this would have been never realized. Also, his words have inspired me a lot, not only for scientific ideas but also how to organize the work and life well.

I thank Prof. Filippov and Dr. Dimaki for many valuable discussions, suggestions and critical comments.

I am also grateful to my kind colleagues in the group. Many thanks to Natalie Milahin, Roman Pohrt, Jasminka Starcevic, Christine Koll, Rainer Heise, Birthe Grzemba, Silvio Kürschner, Elena Teidelt, Lars Voll, Robbin Wetter, Mikhail Popov and Stephan Kusche. In particular I thank Roman Pohrt for teaching me computational skills. He gave me also many excellent advices and patient explanations. I have learned much from him.

And last, but not least, my sincere thanks to my family and friends, especially to my wife. Thanks for her always being there with patience, understanding and love.

Abstract

Tribology focuses on the study and application of friction, wear and lubrication of interacting surfaces. In the present work, three areas of tribological applications are studied: (a) elastomer friction, (b) mixed and boundary lubrication, and (c) fretting wear. In analyzing above problems, we make use of the Method of Dimensionality Reduction (MDR), which enables to essentially simplify the theoretical and numerical analysis of tribological problems by mapping three-dimensional problems to one-dimensional ones.

(a) Elastomer friction. The friction between an elastomer and a hard rough substrate can be attributed to energy dissipation in the elastomer due to internal friction in the material. In the present work, the elastomer is modeled as a simple Kelvin body and the rigid surface as a plane or curved surface with a superimposed self-affine fractal roughness having a Hurst exponent in the range from 0 to 1. The resulting frictional force as a function of velocity always shows a typical structure: it first increases linearly, achieves a plateau and finally drops to another constant level. The coefficient of friction on the plateau depends only weakly on the normal force. At lower velocities, the coefficient of friction depends on two dimensionless combinations of normal force, sliding velocity, shear modulus, viscosity, rms roughness, rms surface gradient, the linear size of the system and its shape, as well as the Hurst exponent of roughness. The physical nature of different regions of the law of friction is discussed and an analytical relation is suggested to describe the coefficient of friction in a wide range of loading conditions. Based on the obtained analytical relations, a master curve procedure is suggested, allowing to "construct" the complete dependence of the coefficient of friction on velocity and normal force on the basis of partial empirical data. Furthermore, a study of the kinetics of the coefficient of friction of an elastomer due to abrupt changes of sliding velocity is presented. Numerical simulations reveal the same qualitative behavior which has been observed experimentally on different classes of materials: the coefficient of friction first jumps and then relaxes to a new stationary value. Parameters of the jump of the coefficient of friction and the relaxation time are determined as functions of material and loading parameters. Depending on velocity and the Hurst exponent, relaxation of friction with characteristic length or characteristic time is observed.

(b) Mixed lubrication. A new model of mixed and boundary lubrication is proposed in the framework of the MDR. The dynamic lubricated rolling contact with creep between rough surfaces is simulated based on the equations of elastohydrodynamic lubrication (EHL). In order to account for the breakthrough of the boundary layer in micro contacts, an additional criterion is imposed. For comparison, a twin-disc test rig is set up to measure the electrical resistance between two lubricated rolling surfaces under different normal forces, rotation speeds and temperatures. We investigate the probability of

boundary layer breakthrough for both experiment and simulation and find good agreement.

(c) Fretting wear. We investigate fretting wear of rotationally symmetric profiles. Proceeding from the recently suggested exact method to simulate wear within the MDR ([1] Dimaki et. al., Int. J. of Solids and Structures, 2014), we suggest an even faster numerical method which speeds up the calculation of wear by further several orders of magnitude.

Zusammenfassung

Die Tribologie befasst sich mit der wissenschaftlichen Beschreibung und Anwendung von Reibung, Schmierung und Verschleiß zwischen kontaktierenden Oberflächen. In der vorliegenden Arbeit werden drei verschiedene tribologische Anwendungen untersucht: (a) Elastomerreibung, (b) Misch- und Grenzschmierung, und (c) Verschleiß durch Fretting. Bei der Analyse der oben genannten Probleme verwenden wir die Methode der Dimensionsreduktion (MDR), die eine wesentliche Vereinfachung der theoretischen und numerischen Analyse tribologischer Probleme ermöglicht, indem dreidimensionale Probleme auf eindimensionale abgebildet werden.

(a) Elastomerreibung. Die Reibung zwischen einem Elastomer und einem rauen starren Körper kann auf die Energiedissipation in dem Elastomer durch innere Reibung zurückgeführt werden. In der vorliegenden Arbeit ist das Elastomer als Kelvin-Körper modelliert und die starre Oberfläche als eine ebene oder gekrümmte Fläche mit einer überlagerten, selbstaffinen, fraktalen Rauheit mit einem Hurst Exponent im Bereich von 0 bis 1. Die Reibungskraft als Funktion der Geschwindigkeit zeigt immer einen typischen Verlauf: Sie steigt zunächst linear an, erreicht dann ein Plateau und fällt schließlich auf einen anderen, konstanten Wert ab. Auf dem Plateau hängt der Reibungskoeffizient nur schwach von der Normalkraft ab. Bei niedrigen Geschwindigkeiten ist er als Funktion von zwei dimensionslosen Größen darstellbar, die Kombinationen von Normalkraft, Geschwindigkeit, Schubmodul, Viskosität, mittlerer Rauheit, Oberflächengradienten, Systemgröße, Systemform und Hurst Exponent sind. Die physikalische Natur des Reibungsgesetzes in den verschiedenen Bereichen wird diskutiert und eine analytische Beziehung gegeben, die den Reibungskoeffizient in einem breiten Intervall von Eingangsgrößen beschreiben kann. Auf der Grundlage einer so erhaltenen analytischen Formel wird ein Master-Kurven-Verfahren vorgestellt, mit dem die vollständige Abhängigkeit des Reibungskoeffizienten von Geschwindigkeit und Normalkraft konstruiert werden kann auf der Grundlage von wenigen empirischen Daten. Untersucht wird außerdem die Kinetik des Reibungskoeffizienten von Elastomeren unter Einwirkung einer abrupten Änderung der Gleitgeschwindigkeit. Numerische Simulationen zeigen das gleiche qualitative Verhalten, das experimentell bei verschiedensten Materialien beobachtet wurde: der Reibungskoeffizient steigt kurz an und nähert sich dann einem neuen stationären Wert. Die Eingangsgrößen des Sprungs des Reibungskoeffizienten und der Relaxationszeit werden als Funktion von Material und Belastungsparametern bestimmt. Je nach Geschwindigkeit und Hurst Exponent kann eine Relaxation der Reibung mit charakteristischer Länge oder charakteristischer Zeit beobachtet werden.

(b) Mischreibung. Ein neues Modell für Mischreibung und Grenzschmierung im Rahmen der MDR wird vorgestellt. Der dynamische, geschmierte Rollkontakt mit Gleiten zwischen rauen Oberflächen wird simuliert auf der Grundlage von Rechnungen der elastohydrodynamischen Schmierung (EHL). Um dem Durchbruch einer Grenzschicht im lokalen Mikrokontakt Rechnung zu tragen, wird ein zusätzliches Kriterium eingeführt. Zum Abgleich dient ein Zweischeiben-Prüfstand, bei dem der elektrische Widerstand zwischen zwei geschmierten Rollflächen unter verschiedenen Normalkräften, Drehzahlen und Temperaturen bestimmt werden kann. Die relative Häufigkeit eines Grenzschicht-Durchbruchs wird in Experiment und Simulation untersucht, wobei sich eine gute Übereinstimmung zeigt.

(c) Verschleiß durch Fretting. Wir untersuchen den Verschleiß durch Fretting von rotationssymmetrischen Profilen. Ausgehend von der vor Kurzem vorgeschlagenen, exakten Methode, um den Verschleiß mittels MDR zu simulieren ([1] Dimaki et. al., Int. J. of Solids and Structures, 2014), präsentieren wir eine noch schnellere numerische Methode, die Verschleißberechnungen um mehrere Größenordnungen beschleunigen kann.

Contents

List of Figures and Tables

List of Symbols

Symbol	unit	Definition
a	m	Contact radius
B_{1D}	m	1D Amplitude spectrum
B_{2D}	m	3D Amplitude spectrum
C_{1D}	m^3	1D Power spectrum
C_{2D}	m^4	3D Power spectrum
c	m	Radius of stick region
$\overline{c}$	1	Dimensionless radius of stick region
D	m	Contact diameter
D_f	1	Fractal dimension
D_l	m	Local contact length
d	m	Indentation depth
$\overline{d}$	1	Dimensionless indentation depth
E	Pa	Elastic modulus
E^*	Pa	Effective elastic modulus
$F_x,\ F_N$	N	Tangential / Normal force
$\overline{F}_N$	1	Dimensionless force
f	m	3D profile
$\overline{f}$	1	Dimensionless 3D profile
$f_0,\ f_\infty$	m	Initial / limiting 3D profile
$f_x,\ f_z$	N	Tangential / Normal force of a spring
G	Pa	Shear modulus

G^*	Pa	Effective shear modulus
G'	Pa	Storage modulus
G''	Pa	Loss modulus
g	m	1D profile
$\overline{g}$	1	Dimensionless 1D profile
g_0, g_∞	m	Initial / limiting 1D profile
H	1	Hurst exponent / dimensionless film thickness
H_0	1	Dimensionless central film thickness
$H_{\min}$	1	Dimensionless minimum film thickness
h	m	rms roughness / film thickness
h	m	Surface topography
h_0	m	Central film thickness
h_c	m	Critical thickness of boundary layer
$h_{\min}$	m	Minimum film thickness
Δh	m	Linear wear
$K_{i,j}$	m^3/N	Stiffness matrix
k	1	Wear coefficient
Δk_x, Δk_z	N/m	Tangential / Normal stiffness of an element
k_x, k_z	N/m	Tangential / Normal stiffness
L, L_{cont}	m	System length (Contact length)
L'	m	Cylinder length
N	1	Number of elements
N	1	Number of cycles
$\overline{N}$	1	Dimensionless number of cycles
q	1/m	Wave number

$q_{\min}$, $q_{\max}$	1/m	Minimum / maximum Wave number
q_z	N/m	Linear force density
R	m	Radius
R^*	m	Equivalent radius
R_c	Ω	Electrical contact resistance
r	m	Coordinate
ΔT	K	Change of temperature
T_0	K	Room temperature
t	s	Time
$\overline{t}$	1	Dimensionless time
U	1	Dimensionless rotation speed
$U^{(0)}$	m	Amplitude of oscillation
u_x, u_z	m	Displacement in horizontal / vertical direction
v	m/s	Velocity
$\overline{v}$	1	Dimensionless velocity
W	1	Dimensionless load
x , z	m	Coordinates
Δx	m	Spacing distance
∇z , ∇z_{cont}	1	rms gradient of the surface profile (real contact)
α	1	Dimensionless constant
β	1	Dimensionless constant
$\Delta\gamma$	$\text{N}\cdot\text{s/m}$	Damping coefficient
δ	m	Elastic deformation
$\overline{\delta}$	1	Dimensionless elastic deformation
ε	1	Strain

ζ	1	Coefficient
η , η_0	$\mathrm{Pa \cdot s}$	Viscosity (at atmosphere pressure)
$\overline{\eta}$	1	Dimensionless viscosity
θ	1	Angle
λ	W/K	Thermal conductivity
μ	1	Coefficient of friction
μ_1 , μ_2	1	Coefficient of friction at velocity v_1 and v_2
μ^*	1	Difference of coefficient of friction μ_1 - μ_2
$\Delta\overline{\mu}_0$, $\Delta\mu_0$	1	(Dimensionless) difference of $\mu(t_0) - \mu_2$
$\overline{\mu}$	1	Normalized coefficient of friction
ξ	1	Dimensionless variable / coefficient
ρ	Ωm	Resistivity of contacting material
ρ	$\mathrm{Kg/m^3}$	Lubricant density
$\overline{\rho}$	1	Dimensionless lubricant density
σ	Pa	Stress
σ_0	Pa	Hardness
τ	s	Relaxation time
τ_0	Pa	Limiting shear modulus
ν	1	Poisson's ratio
ϕ	1	Phase angle
ω	Hz	Frequency

Chapter 1 Introduction

1.1 Contact mechanics and tribology

As defined by Johnson [2], "the theory of contact mechanics is concerned with the stresses and deformation which arise when the surfaces of two solid bodies are brought into contact." One of the most prominent contributions to contact mechanics is the classic work of Heinrich Hertz "Über die Berührung fester elastischer Körper" in 1882 [3]. Hertz solved the contact problem for two elastic solids with curved surfaces. Using an analogy with known solutions in potential theory of electrostatic problems, he developed a theory to calculate the contact area and stress between two surfaces pressed against each other. This theory still remains one of the bases of engineering design, for example, of the coupling parts in mechanical engineering such as bearings and gears. The Hertz theory did not consider Van der Waals interactions of contacting bodies; thus the effects of adhesion were not taken into account. In 1771, almost one hundred years later, Johnson, Kendall and Roberts extended the Hertz theory by including the adhesive interactions [4]. Almost at the same time a similar theory, known as DMT (Derjaguin, Muller and Toporov) theory was proposed [5] where Van der Waals interactions are taken into account outside the elastic contact region. After fierce discussion, both theories were proved correct but for very special limits [6][7].

This work deals with different aspects of tribology. The term "tribology" was introduced by Perter Jost in 1966 and is defined usually as "the science and technology of interacting surfaces in relative motion and of related subjects and practices" [8]. It covers and connects a large range of knowledge from theory of elasticity and plasticity, viscoelasticity, material science, fluid mechanics and so on. This very broad scope embraces the study and application of friction, wear and lubrication. Tribological phenomena occur everywhere in our daily life. A simple example is walking: the friction between our feet (or shoes) and road pushes us to move forward. Without friction we cannot move on, write, drive and have a meal. Other than the name "tribology", the tribological praxis is very old, as humans surely dealt with friction long before the recorded history. Thousands years before Christ our ancestors have known the creation of fire through the friction of wooden sticks. The Egyptians used liquid as a lubricant to reduce the friction for the transportation of colossus. A prehistoric rock carving found in Rodoy Island, Norway showed a skiing man about 4000 years ago (Fig. 1.1). In mechanical engineering, tribology plays an essential role, especially for structure safety and energy saving. Its application can be widely observed, such as rail-wheel contacts, bearings, clutches, gaskets, brake pads and so on.

Fig. 1.1 A stamp with ski symbol of prehistoric rock carving, c. 2000 BC.

Many examples show how early the human being dealt with tribology. However, the scientific study of tribology is thought to begin with Leonardo da Vinci in the 15th century, even if he did not publish his findings. In his diaries, he describes the law of friction which could be formulated as two statements: (a) the frictional force is proportional to the weight and (b) it is independent of contact area. Later many scientists and mathematicians formalized the knowledge in tribology, including the often quoted Amontons, Euler and Coulomb. Tribology includes a great variety of applications from industrial applications to bionics, it considers processes an object from the nano- and micro meter scale to the scale of technical plates. It is impossible to list all scientists and their main works and the history of tribology, which can be read in detail in Dowson [9] and Popov's book [10]. Some more details to the history of tribology will be mentioned in the following in connection with particular research areas of this work.

(a) Friction of elastomers

In description of history of elastomer friction, I follow partly the work [11] (Li, et. al. Phys. Rev. Lett. 111, 034301, 2013) and [12] (..., Li et. al. Sci. Rep. 4, 3750, 2014). As already have been mentioned above, friction is a phenomenon that people have been interested in for thousands of years but its physical reasons are not clarified completely yet. Not only is it still not possible to predict the frictional force theoretically, there are also no reliable empirical laws of friction which would satisfy the needs of modern technology. In practice, the simplest Amontons' law of dry friction is usually used, stating that the force of friction is proportional to the normal force. According to Amontons, the coefficient of friction does not depend on the normal force and the contact area. Amontons did not differentiate between the static and the sliding coefficients of friction, nor even between different materials (he states that the ratio of the frictional force to the normal force is "roughly" one third of the normal force, independently of the contacting materials as long as they are not lubricated [13]). However, already Coulomb knew that the coefficient of friction, even between the same material pairing, can change by a factor of about four depending on the contact size and on the normal force [14]. As a

matter of fact, there are no obvious reasons for the validity of Amontons' law. On the contrary, much effort has been made in the 1940's to 60's years to understand why Amontons' law is approximately valid [17][18]. In a more general context, the strong violations of Amontons' law were studied experimentally and theoretically in recent papers [17][18]. Deviations from Amontons' law can be due to macroscopic interfacial dynamics [21]-[21] or they can be connected with the contact mechanics of rough surfaces.

It is generally accepted that the surface roughness plays a central role in friction processes since classical works by Bowden and Tabor . Greenwood and Tabor [22] have shown that the friction of elastomers can be attributed to deformation losses in the elastomer. In 1963, Grosch supported this idea by a series of experiments of friction between rubber and hard surfaces with controlled roughness [23]. In the following years, the basic understanding of the role of rheology [26] and of surface roughness [25][26] in elastomer friction has been achieved. The load dependence of the elastomer friction was studied experimentally by Schallamach in 1952 [27]. However, the dependence of the sliding coefficient of friction on normal force was not studied in detail yet. Therefore, we study the sliding friction of elastomers and formulate rules for constructing generalized laws of friction beyond the regions of validity of Amontons' law.

(b) Mixed and boundary lubrication

Stribeck curve is well known to describe the lubrication condition for the lubricated sliding surfaces. It reflects the influence of viscosity η, rotation speed v and load P on the coefficient of friction. According to it, friction regimes for contact between lubricated surfaces were categorized into four parts: boundary lubrication, mixed lubrication (or partial lubrication), elastohydrodynamic lubrication (EHL) and hydrodynamic lubrication.

The coefficient of friction between lubricated surfaces in different conditions has become an important topic of research since the lubricant testing in 1879 from Thurston who gave the value of the coefficients of friction at different loads, speeds and temperatures. The results showed clearly the minimum now known as the transition between the full hydrodynamic lubrication and the partial lubrication with asperities interaction [28]. Later in 1902, Stribeck studied this variation of friction systematically as function of speed for different loads [29]. After about 10 years Gümbel firstly plotted the friction coefficient against the dimensionless lubrication parameter $\eta v/P$ with Stribeck's experiment data and he divided the friction regimes into boundary, mixed and hydrodynamic lubrication [30] With the development of investigation on EHL, Dowson proposed a new categorization of lubrication regimes in Stribeck curve as seen in Fig. 1.2 (below) [31]. Nowadays the Stribeck curve is still being studied numerically and experimentally for different rough surfaces [32].

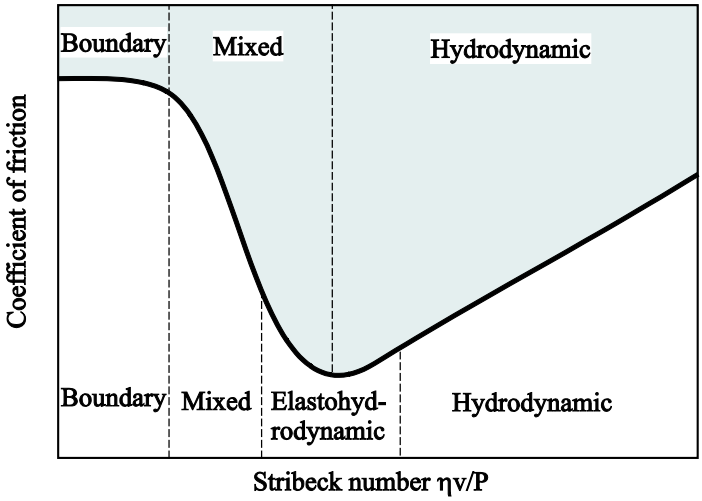

Fig. 1.2 Schematic Stribeck curve and partitioning into different frictional regimes according to Gümbel (top) and Dowson (bottom).

Comparing with the others, mixed lubrication is most complicated because it is necessary to handle both hydrodynamic lubrication and asperity contacts. Here I describe the historical research on mixed lubrication following the introduction of work [33] (Li et. al. FACTA Univ. Ser. Mech. Eng. 11, 123–131, 2013). The earliest way of modeling mixed lubrication was considering the influence of roughness in hydrodynamic systems where the film thickness is considerably larger than the roughness [34]. In 1970s Tallian and Johnson considered both asperity contact and hydrodynamic lubrication. Tallian studied the cases where asperities deformed elastically and plastically while Johnson only considered the elastic deformation based on the Greenwood and Williamson model [35][36]. Later micro-EHL models and combined micro-EHL and asperity contact models included the interaction of surface roughness, film thickness and pressure [37]. A stochastic analysis was developed by Zhu and Cheng (1988) [38]. It combined Patir and Cheng's average flow model (1978) [39] for hydrodynamic lubrication and Greenwood and Tripp's load compliance relation (1970) [40] for asperity contacts. With the rapid development of numerical simulation techniques and faster computers, researchers were able to investigate more complicated lubrication problems. Therefore more realistic transient, rough surface, thermal and non-Newtonian lubrication problems were studied in the past decade. A deterministic model for mixed lubrication in point contacts was developed by Jiang et al. (1999) and the contact between asperities was studied when they moved through the EHL region [41] . Wang et al. (2004) developed a thermal model for mixed lubrication in point contact [42]. In this thesis we try a simple model for the mixed lubrication and compare its results with experiment.

(c) Fretting wear

Dry friction is always accompanied by wear. Wear is the loss of the material on the surfaces caused by the relative motion of contacting bodies due to mechanical or

chemical action. The study of wear started relatively late. It was probably the adhesive model of friction by Bowden and Tabor which started intensive wear research. However, already as early as 1860, Reye came to the physical conclusion that the wear volume of material is proportional to the work done by frictional force [43]. Later, in 1953 Archard also proposed a similar model used to describe wear based on the contact of asperities [44]. The simple but today still broadly used wear equation, that wear volume is proportional to load and sliding distance and inversely proportional to the hardness of the weared material, was derived and experimentally justified by Khrushchov in 1960 for abrasive wear [45] and by Archard in 1956 for adhesive wear [46].

According to different physical mechanisms, there are different types of wear mainly including adhesive wear, abrasive wear, fretting wear, surface fatigue and erosive wear. Fretting wear occurs when the surfaces are rubbed and materials at the edge of contact area are removed due to an oscillatory motion with small amplitude of the contacting surface under load. Fretting wear is said to be one of the most insidious causes for failure of engineering components and has been studied intensively in connection with such applications as fretting of tubes in steam generators [47]-[49], medical applications [50], electrical contacts [51], fretting fatigue of dovetail blade roots [52][52][53] and many others. Most theoretical results are provided by use of numerical modelling techniques, such as finite element method or boundary element method which require very much computing time. In this thesis we consider this problem of fretting wear in the framework of the MDR.

1.2 Method of Dimensionality Reduction (MDR)

The method of dimensionality reduction is a method used for fast calculation and simulation of contacts problems for elastic and viscoelastic bodies. It was firstly proposed by Popov and Psakhie in 2007 for a reduced description of classical tribology system [54]. With this method some kinds of three dimensional contact problems are mapped onto one-dimensional simple contacts with elastic or viscoelastic foundations. Later Geike, Heß and Popov applied this method to elastic and viscoelastic contact problems, including normal and tangential contacts, with and without adhesion [55]-[57]. Even more, it is also available for randomly rough fractal self-affine surfaces and for arbitrary bodies of revolution [58][59]. This “mapping” is not an approximation, but exact. With this method, all parameters that depend on the force-displacement relationship can be easily calculated, such as contact stiffness and related electrical resistance and thermal conductivity, and also dissipated energy and frictional force for elastomers. Recently this method was applied to solve wear problems [60]. Besides the simplification and easy understanding, an obvious advantage of usage of MDR is sharply reduced computing time. Compared with other numerical methods, such as finite element method and boundary element method, the computing time with MDR reduces by several orders of magnitude. The details are presented in Chapter 2.

1.3 Outline of the thesis

Since the MDR was proposed, many problems in contact mechanics and tribology have been studied. In this thesis we try to investigate some hot topics in these three fields of tribology.

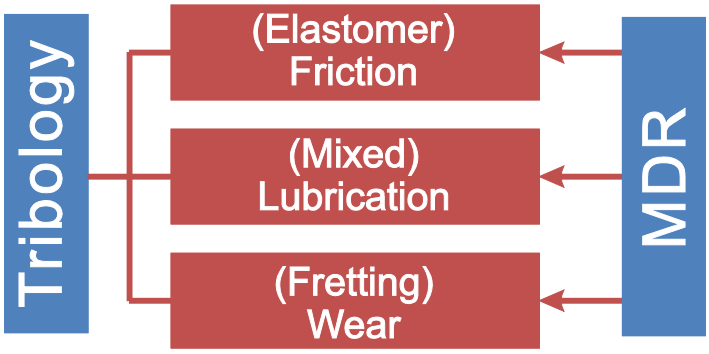

Fig. 1.3 Structure of thesis.

The thesis is organized as followings (see Fig. 1.3). After a short introduction to fundamentals of the MDR in chapter 2, the friction of elastomers is considered in chapter 3 and chapter 4 where chapter 3 presents a general law of friction between elastomer and differently shaped rigid bodies with random roughness and chapter 4 presents a further study of dynamic frictional behavior of elastomers. In chapter 5 the mixed boundary lubrication is studied with MDR. In chapter 6 the study of fretting wear is described. All of researches on these themes are in the frame of the MDR. Finally the conclusions and possible future works are reported in chapter 7.

This thesis is partially based on the following publications:

1. [11] Li, Q., Popov, M., Dimaki, A., Filippov, A. E., Kürschner, S. & Popov, V. L. Friction between a viscoelastic body and a rigid surface with random self-affine roughness. *Phys. Rev. Lett.* 111, 034301 (2013).
2. [12] Popov, V. L., Lars, V., Li, Q., Chai, Y. S. & Popov, M. Generalized law of friction between elastomers and differently shaped rough bodies. *Sci. Rep.* 4, 3750 (2014).
3. [61] Li, Q., Dimaki, A. V., Popov, M., Psakhie, S. G. & Popov, V. L. Kinetics of the coefficient of friction of elastomers. *Sci. Rep.* 4, 5795 (2014).
4. [33] Li, Q. & Pohrt, R. Mixed and Boundary Lubrication in Rolling Contact: Experiment and Simulation. *FACTA Univ. Ser. Mech. Eng.* 11, 123–131 (2013).
5. [62] Li, Q., Filippov, A. E., Dimaki, A. V., Chai, Y. S. & Popov, V. L. Simplified simulation of fretting wear using the method of dimensionality reduction. *Phys. Mesomech.* 17, 236–241 (2014).

Chapter 2 Method of Dimensionality Reduction

This chapter briefly reviews the necessary fundamentals of method of dimensionality reduction (MDR). According to rules of MDR, only two main steps are necessary for the mapping of three-dimensional contact onto one-dimensional. Sequentially we firstly introduce the elastic (or viscoelastic) foundations then come to the transformation of three-dimensional profile to one-dimensional. The axially-symmetric profile and randomly rough profile are presented separately.

2.1 Introduction to MDR

MDR has been developed by the group of Popov in recent few years. Compared with other numerical methods, such as finite element method (FEM), boundary element method (BEM), MDR is relative new, but increasing evidences show that it can be applied well for a variety of contact and frictional problems. With this method three-dimensional contacts are mapped onto one-dimensional ones with properly defined elastic or viscoelastic foundations. MDR provides exact solutions for normal contact problem of axially symmetric and self-affine fractal surfaces as well as exact solutions for tangential contact problem with a constant coefficient of friction. All properties which depend on the force-displacement relationship such as contact stiffness, electrical resistance and thermal conductivity, as well as frictional force for elastomers can be analyzed with this method. The very detailed principles, proofs and applications are described in the books [63] [64]. In this chapter we only give short sketch of the fundamentals of the method.

In this thesis we study the contact of both profiles (rough surfaces for viscoelastic contact and mixed boundary lubrication, and axially-symmetric profiles for fretting wear). Therefore, these rules are described separately in the following two sections.

2.2 Axially-symmetric profile

We consider a contact between two elastic bodies with moduli of elasticity of E_1 and E_2, Poison's numbers of ν_1 and ν_2, and shear moduli of G_1 and G_2. According to "handbook" in [65], two steps have to be done to replace the complete three-dimensional problem with a simple one-dimensional system.

2.2.1 One-dimensional foundations

At first, the three-dimensional elastic or viscoelastic bodies are replaced by one-dimensional foundations. The foundation consists of an array of elements having independent degrees of freedom and a sufficiently small distance Δx. For elastic contact, the elements are linear springs having normal stiffness Δk_z and tangential stiffness Δk_x:

$$\Delta k_z = E^* \Delta x \text{ with } \frac{1}{E^*} = \frac{1-\nu_1^2}{E_1} + \frac{1-\nu_2^2}{E_2}, \tag{2.1}$$

$$\Delta k_x = G^* \Delta x \text{ with } \frac{1}{G^*} = \frac{2-\nu_1}{4G_1} + \frac{2-\nu_2}{4G_2}. \tag{2.2}$$

Here E^* and G^* are effective elastic and shear moduli. For viscous materials, the elements are linear dampers with damping coefficients $\Delta\gamma$:

$$\Delta\gamma = 4\eta\Delta x. \tag{2.3}$$

Here η is viscosity of material. It is known that elastomers can be modeled as different combinations of springs and dampers. For example, the element in Kevin-Voigt model is a combination of parallel connected spring and damper and in standard model a spring and a Maxwell element in parallel. These rules are also valid for the contact between a viscoelastic and a rigid body. These foundations are illustrated in Fig. 2.1.

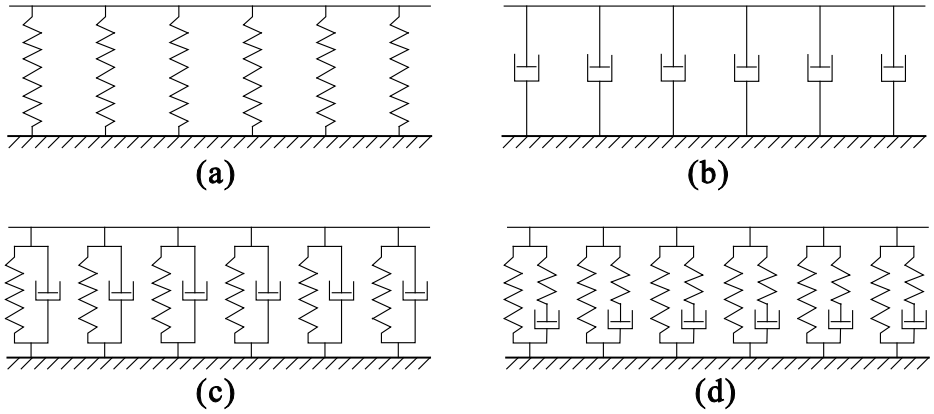

Fig. 2.1 One-dimensional foundation of (a) elastic body, (b) viscous body, and (c) viscoelastic body with Kelvin-Voigt model (d) viscoelastic body with standard model.

2.2.2 Transformation of three-dimensional profiles

The second step is a transformation of the three-dimensional profile to a one-dimensional profile. We notate the three-dimensional profile $z = f(r)$, r being the polar radius in the contact plane, and the and the one-dimensional $g(x)$. According to [65], the three-dimensional profile is transformed into one-dimensional profile $g(x)$ according to equation

$$g(x) = |x| \int_0^{|x|} \frac{f'(r)}{\sqrt{x^2 - r^2}} \mathrm{d}r. \tag{2.4}$$

The reverse transformation is given by

$$f(r)=\frac{2}{\pi}\int_0^r \frac{g(x)}{\sqrt{r^2-x^2}}\mathrm{d}x\,. \tag{2.5}$$

This transformation is illustrated schematically in the Fig. 2.2. For instance, the transformed profile of a sphere formulated as $f(r)=\frac{r^2}{2R}$ is expressed as $g(x)=\frac{x^2}{R}$, and in the case of a cone $f(r)=r\tan\theta$, the corresponding one-dimensional profile is given by $g(x)=\frac{\pi}{2}|x|\tan\theta$.

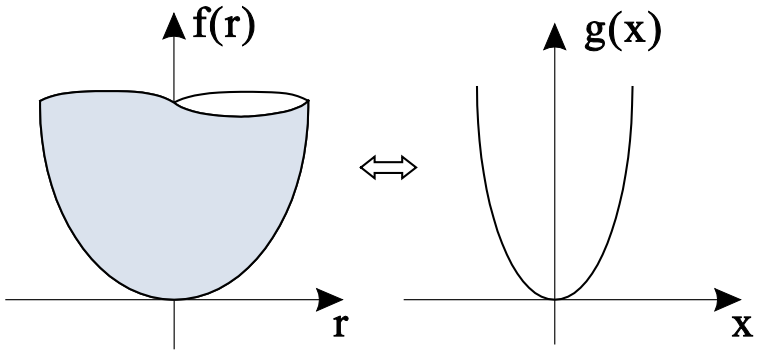

Fig. 2.2 Schematic of profile tranformation for axially-symmetric body.

2.2.3 Calculation procedures in the case of elastic contact

We consider an example of simple elastic contact between an axially-symmetric profile and a half-space without adhesion. The profile can be parabolic, conical shape or an arbitrary power function. Under the normal load F_N the indenter is pressed into elastic half-space (Fig. 2.3). The normal force of a spring on the foundation is proportional to the displacement of this spring:

$$f_z(x)=\Delta k_z u_z(x), \tag{2.6}$$

and the linear force density is equal to

$$q_z(x)=\frac{f_z(x)}{\Delta x}=E^* u_z(x)\,. \tag{2.7}$$

The contact radius a is determined by the condition

$$g(a)=d\,, \tag{2.8}$$

where d is indentation depth. The sum of forces over all springs in contact must equal to the normal load

$$F_N=\sum_{i=\text{contact}}\Delta k_z u_z(i)\,. \tag{2.9}$$

In the limiting case of sufficiently small distance $\Delta x \to \mathrm{d}x$, it becomes the integral:

$$F_N = E^* \int_{-a}^{a} u_z(x)\mathrm{d}x = 2E^* \int_0^a \left[d - g(x)\right]\mathrm{d}x. \tag{2.10}$$

If the linear force density (2.7) is known, the normal stress distribution in the initial three-dimensional contact can be calculated by the following transformation [65]

$$p(r) = -\frac{1}{\pi}\int_r^{\infty} \frac{q_z'(x)}{\sqrt{x^2 - r^2}}\mathrm{d}x. \tag{2.11}$$

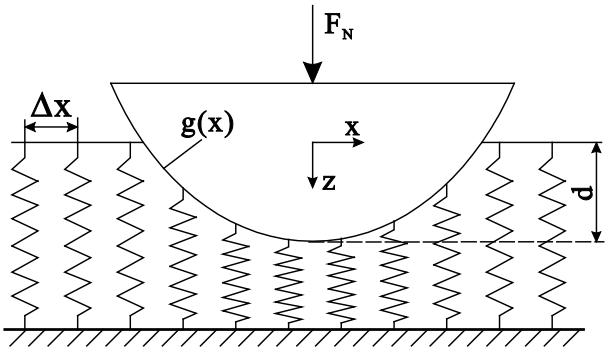

Fig. 2.3 One-dimensional contact between an indenter and an elastic foundation.

With the new simple one-dimensional system, further calculations, such as determination of the dependence of force on indentation can be easily carried out. Such procedures together with transformation and reverse transformation of profile allow the MDR to quickly solve many contact problems, including the tangential and adhesive contact problems. In the Chapter 6, the MDR for axially-symmetric profiles will be applied to the problem of fretting wear.

2.3 Fractal profile

Almost all surfaces of materials in our everyday life are rough, even those of the well-polished glasses. Since Bowden and Tabor's classic work, roughness has played an important role in study of contact mechanics. More and more sophisticated instruments have been developed to measure surface topography. The statistical parameters, such as root mean square (rms), skewness, amplitude probability distribution, structure function and power spectral density and so on, are applied for description of surface characteristic. In this section, we focus on the theoretical model of rough surfaces, and show the relation between three-dimensional surface and corresponding one-dimensional "line" (Fig. 2.4). Finally the generation of the fractal "surface" with random roughness is presented which will be used for the study in latter Chapters, i.e. contact of rough surfaces for elastomers and mixed boundary lubrication.

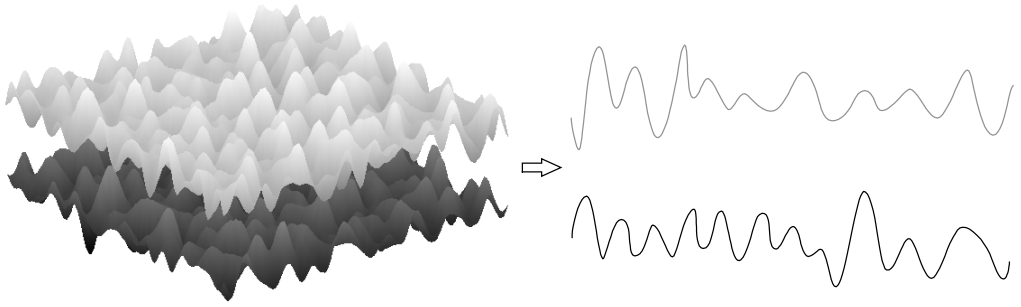

Fig. 2.4 Schematic of three-dimensional surface and corresponding one-dimensional "line".

2.3.1 Characterization of fractal surface

In the model of Greenwood and Williamson, it is assumed that all asperities on the surface have the same radius of curvature and that their heights vary randomly following a Gaussian distribution. If the contacting asperities are far enough away from each other, their deformation can be considered to be independent on each other. Thus, only the distribution of the heights of asperities and the radii of curvature are important [66]. So the one-dimensional system should have the necessary statistical distributions of heights and radii of curvature. For simplification, we assume that the topographies of three-dimensional surface and of its one-dimensional mapping are unambiguously characterized by their roughness power spectra $C_{2D}(\boldsymbol{q})$ and $C_{1D}(q)$, which are defined by

$$C_{2D}(\boldsymbol{q}) = \frac{1}{(2\pi)^2}\int \langle h(\boldsymbol{x})h(\boldsymbol{0})\rangle e^{-i\boldsymbol{q}\cdot\boldsymbol{x}}\mathrm{d}^2x \quad \text{for a surface} \tag{2.12}$$

$$C_{1D}(q) = \frac{1}{2\pi}\int \langle h(x)h(0)\rangle e^{-iqx}\mathrm{d}x \quad \text{for a line} \tag{2.13}$$

where $h(\boldsymbol{x})$ is the height profile measured from the average plane so that $\langle h\rangle = 0$, and $\langle\cdots\rangle$ means averaging over the statistical ensemble. We assume that the statistical properties of surface topography are homogeneous and isotropic, so that its power spectrum $C_{2D}(\boldsymbol{q})$ only depends on the magnitude of the wave vector $\boldsymbol{q}$.

A large number of real surfaces are composed of many length scales of roughness which are superimposed on each other. Such a surface can be considered self-affine fractal and its power spectrum often has the following power law behavior:

$$C_{2D}(q) = \text{const}\cdot\left(\frac{q}{q_0}\right)^{-2H-2} \quad \text{for a surface,} \tag{2.14}$$

$$C_{1D}(q) = \text{const} \cdot \left(\frac{q}{q_0} \right)^{-2H-1} \quad \text{for a line,} \tag{2.15}$$

where H is the Hurst exponent directly related to the fractal dimension of an original two-dimensional surface through $D_f = 3 - H$. Fig. 2.5 shows a schematic of the power spectral density of a fractal surface in a logarithmic diagram.

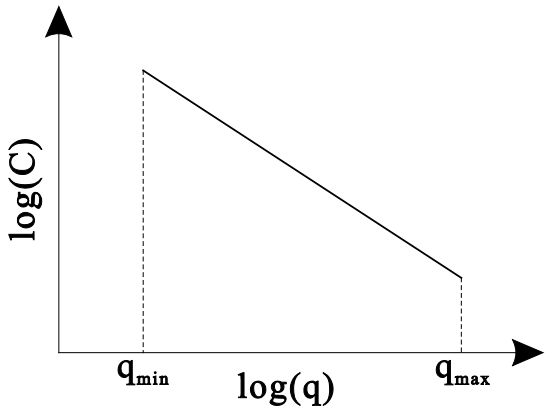

Fig. 2.5 Schematic of the power spectral density of roughness.

The two-dimensional surface topography can be calculated with the help of power spectrum according to

$$h(\boldsymbol{x}) = \sum_{\boldsymbol{q}} B_{2D}(\boldsymbol{q}) \exp\left(i\left(\boldsymbol{q} \cdot \boldsymbol{x} + \phi(\boldsymbol{q}) \right) \right) \tag{2.16}$$

with

$$B_{2D}(\boldsymbol{q}) = \frac{2\pi}{L} \sqrt{C_{2D}(\boldsymbol{q})} = \overline{B}_{2D}(\boldsymbol{-q}). \tag{2.17}$$

In one-dimensional case the line is generated by

$$h(x) = \sum_{q} B_{1D}(q) \exp\left(i\left(qx + \phi(q) \right) \right) \tag{2.18}$$

with

$$B_{1D}(q) = \frac{2\pi}{L} \sqrt{C_{1D}(q)} = \overline{B}_{1D}(-q). \tag{2.19}$$

The phases above have $\phi(\boldsymbol{q}) = -\phi(\boldsymbol{q})$ and are assumed to be distributed randomly[1] in the interval $[0, 2\pi)$.

[1] Such surfaces are called “randomly rough”.

In the paper [55], it was suggested, that in order to produce a one-dimensional system with the same contact properties as the three-dimensional system, the one-dimensional power spectrum must be used according to the rule

$$C_{1D}(q) = \pi q C_{2D}(q). \tag{2.20}$$

The root mean square roughness $\langle h^2 \rangle^{1/2}$ for the two-dimensional and one-dimensional cases, respectively, are determined by

$$\langle h^2 \rangle_{2D} = 2\pi \int_0^\infty q C_{2D}(q) \mathrm{d}q, \tag{2.21}$$

$$\langle h^2 \rangle_{1D} = 2 \int_0^\infty C_{1D}(q) \mathrm{d}q. \tag{2.22}$$

They are the same when $C_{1D}(q) = \pi q C_{2D}(q)$. The corresponding root mean square of the surface gradient $\langle \nabla z^2 \rangle$ and curvature $\langle \kappa^2 \rangle$ also coincide in this case. The rms gradients are related to the power spectral density through

$$\langle \nabla z^2 \rangle_{2D} = 2\pi \int_0^\infty q^3 C_{2D}(q) \mathrm{d}q, \tag{2.23}$$

$$\langle \nabla z^2 \rangle_{1D} = 2 \int_0^\infty q^2 C_{1D}(q) \mathrm{d}q. \tag{2.24}$$

2.3.2 Generation of randomly rough "surface"

With above Eq. (2.14) to (2.19), a fractal three-dimensional surface or one-dimensional profile with random roughness can be generated. We consider only the one-dimensional line having the power spectral density $C_{1D} \propto q^{-2H-1}$. This one-dimensional power density corresponds to the two-dimensional power density of the form (2.14) $C_{2D} \propto q^{-2H-2}$. The spectral density was defined in the interval from [$q_{\min}$, $q_{\max}$] with long distance roll-off wave vector $q_{\min} = 2\pi/\lambda_{\max}$ and short distance cut-off wave vector $q_{\max} = 2\pi/\lambda_{\min}$. According to Eq. (2.22), the roughness amplitude of surface can be calculated as

$$\langle h^2 \rangle_{1D} = \int_{q_{\min}}^{q_{\max}} \mathrm{const} \cdot q^{-2H-1} \mathrm{d}q = \mathrm{const} \cdot \left(q_{\max}^{-2H} - q_{\min}^{-2H} \right) \approx \frac{\mathrm{const}}{2H} \cdot q_{\min}^{-2H} \tag{2.25}$$

if $q_{\max} >> q_{\min}$. From Eq. (2.24) the root mean square of the surface gradient $\langle \nabla z^2 \rangle$ follows the relation

$$\langle \nabla z^2 \rangle_{1D} = \int_{q_{\min}}^{q_{\max}} \mathrm{const} \cdot q^{-2H+1} \mathrm{d}q = \frac{\mathrm{const}}{2-2H} \left(q_{\max}^{2-2H} - q_{\min}^{2-2H} \right). \tag{2.26}$$

For a fractal rough profile with a short cut-off wave vector $q_{\max}$ we have the following estimation

$$\left\langle \nabla z^2 \right\rangle_{1D} \approx \frac{\text{const}}{2-2H} q_{\max}^{2-2H}. \tag{2.27}$$

Thus, from Eq. (2.25) and (2.27) we see that surface topography is characterized by the rms roughness, which is dominated by the long wavelength components of the power spectrum and the rms gradient of the surface is dominated by the short wavelength part of the spectrum.

Let us illustrate the above said with several numerical examples. In the following, we will define the power spectral density C_{1D} in the interval $\frac{2\pi}{L} < |q| < \frac{\pi}{\Delta x}$, where L is the system size and Δx discretization space which determines the upper cut-off wave vector. The minimal and maximal values $q_{\min} = 2\pi/L$ and $q_{\max} = \pi/\Delta x$ mean that there is neither roll-off nor cut-off at the lower and upper limit except for the natural cut-off due to the finite size of system length and spacing. In Fig. 2.6, the lines are generated numerically with the same phase and roughness for different Hurst exponents. The number of points on the lines are 5000. It is clearly seen that higher values of Hurst exponent indicate a smoother trend and less volatility.

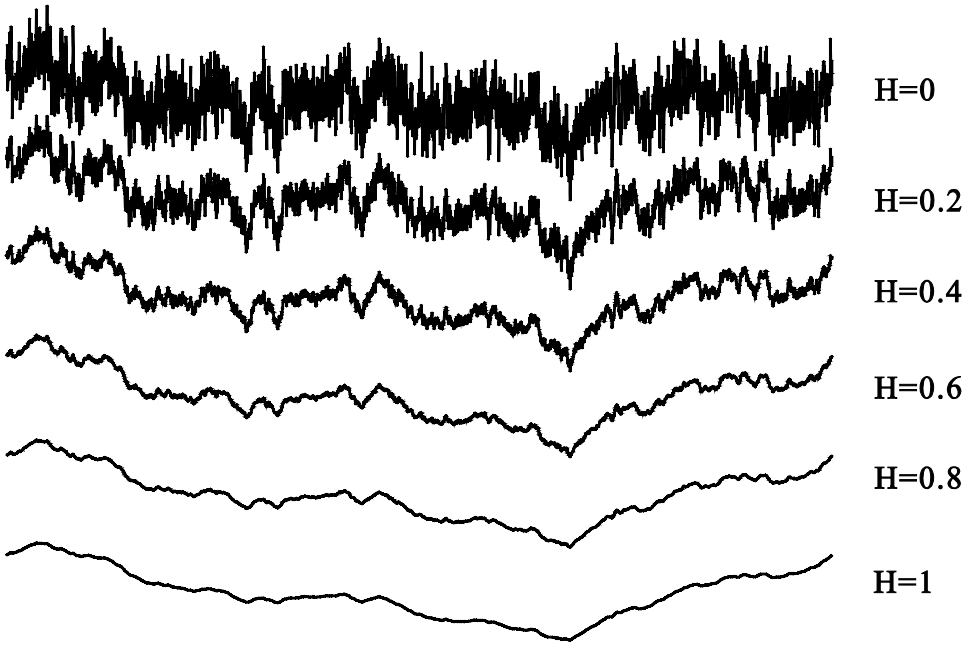

Fig. 2.6 One-dimensional profiles with different Hurst exponents. These lines are generated numerically with the same distribution of phase.

2.4 Summary

We shortly reviewed the basics of method of dimensionality reduction. The rules for contact of axially-symmetric bodies and rough surfaces introduced in two separate sections will be used as a basis of studies in the following chapters.

Chapter 3 Friction Law of Elastomers

In this and next chapter the frictional behaviors of elastomer contacting with a rigid surface will be described using MDR. Chapter 3 presents the friction law for the contact between an elastomer and differently shaped rigid surface (planar, parabolic and conical profiles with random roughness). Firstly a brief introduction to elastomers and their physical properties is given in Section 3.1. Then the models of viscoelasticity, focusing on Kelvin model, are described in Section 3.2. Section 3.3 and 3.4 present very detailed simulations and discussions for the friction law of elastomer. In the same way, a further study concerning, kinetic coefficient of friction for elastomer contact is presented in Chapter 4.

To achieve the basic understanding of this nonlinear frictional behavior, the following simple model is proposed:

- the elastomer is modeled as a simple Kelvin body, which is completely characterized by its static shear modulus and viscosity;
- the non-disturbed surface of the elastomer is plane and frictionless;
- the rigid counter body is assumed to have a randomly rough, self-affine fractal surface without long wave cut-off;
- no adhesion or capillarity effects are taken into account;
- one-dimensional model is considered.

These simple assumptions still result in non-trivial and complicated frictional behavior. Here, we avoid the well discussed subject of the temperature dependence and concentrate our efforts completely on the force dependence.

The work in section 3.2 and 3.3 appears in paper [11] (Li, Q. *et al.* Friction between a viscoelastic body and a rigid surface with random self-affine roughness. *Phys. Rev. Lett.* 111, 034301 (2013)) and [12] (Popov, V. L., Lars, V., Li, Q., Chai, Y. S. & Popov, M. Generalized law of friction between elastomers and differently shaped rough bodies. *Sci. Rep.* 4, 3750 (2014)). My contributions to these papers are described at the beginning of the two sections.

3.1 Elastomers and their applications

Elastomers are usually related to a group of polymers with some common properties, such as high elasticity, viscoelasticity and glass transition temperature. The name “elastomer”, driven from “elastic polymer”, is often used with the term “rubber”. As a material, it plays an important role in many applications in industry and human life, such as tires, seals, shoe soles as well as some dampening elements [67].

The chemical structure of elastomers determines its properties. Rubber materials are composed of long chainlike molecules. Normally the long polymer chains are irregularly coiled to each other. If a stress is acted on the elastomer, the molecules start to stretch. After the remove of load, they spontaneously return to the coiled state. This cross-linking structure ensures that the elastomer will recover their original shape when the stress is removed (Fig. 3.1).

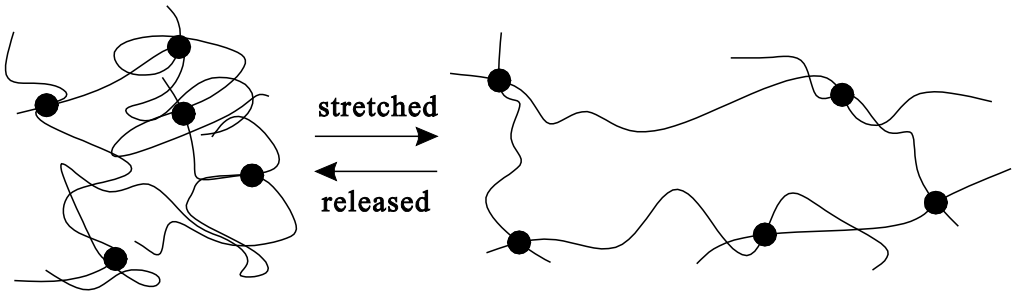

Fig. 3.1 Polymer chains in original shape and under stress.

Compared with other solids, elastomers have the following characteristic properties:

(1) very small elastic modulus (ca. 1~10 MPa, about 10^4 to 10^5 times smaller than the ordinary metals);
(2) very large elastic deformations;
(3) incompressibility: elastomers can be considered in a good approximation as incompressible media. Correspondingly, their Poisson's ratio is almost equal to 0.5;
(4) unlike ordinary metals, their elastic deformation is time-dependent, which is so-called relaxation. The related phenomena, such as stress relaxation, creep and hysteresis loss are due to the viscoelasticity of elastomer which essentially determines the contact and frictional properties.

These properties enable rubber materials to be widely applied in mechanical engineering and human life, such as vehicle tires, frictional components (sealing, bearings), and gloves and so on. Since the 1950s, rubber products have developed fast and the demand for a clear understanding of rubber tribology is correspondingly growing quickly. There are a number of papers in the field considering elastomer friction in the framework of the rheology paradigm. Many of them concentrate on the dependence of the coefficient of friction on velocity. On the contrary, the dependency of the coefficient of friction on the normal force was practically out of scope of all previous studies. In this chapter, we try to overcome this shortage and to formulate generalized laws of friction including the dependencies of both sliding velocity and normal force.

Kelvin model of linear viscoelasticity

The viscoelastic behavior of elastomer material can be modeled with linear combinations of Hookean elastic springs and Newtonian dampers. For example, Maxwell model is a

spring connected with a dashpot in series (Fig. 3.2a), and Kelvin model (also known as Kelvin-Voigt model) (Fig. 3.2b) in parallel. Standard Linear Solid model combines a Maxwell element and a linear spring (Fig. 3.2c). In this dissertation we used the Kelvin model for the viscoelastic material. This model can explain the creep behavior of rubber material. If a constant stress is applied on the material, it will deform gradually to a steady state due to the viscosity. When the stress is released, it relaxes slowly to the original state.

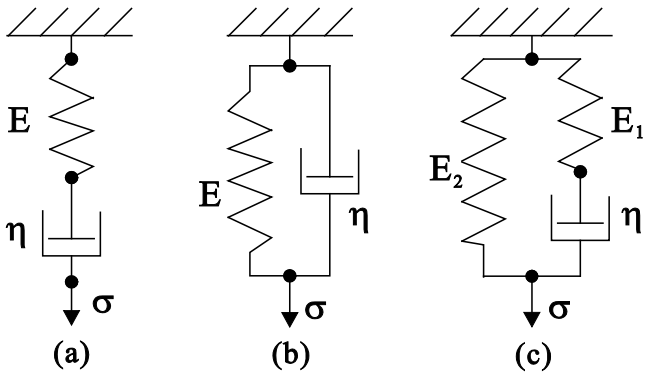

Fig. 3.2 Models of linear viscoelasticity: (a) Maxwell Model; (b) Kelvin Model; (c) Standard Linear Solid model.

The elastic component is modeled as spring with elastic modulus E, which follows Hooke's law:

$$\sigma = E \cdot \varepsilon . \tag{3.1}$$

Here σ is the stress and ε strain under the stress. The viscous component is modeled as dashpot with viscosity η, which is Newtonian fluid:

$$\sigma = \eta \cdot \frac{\mathrm{d}\varepsilon}{\mathrm{d}t} . \tag{3.2}$$

From the Kelvin model, spring is connected with the damper in parallel so that the relation between stress and strain is given as

$$\sigma(t) = E \cdot \varepsilon(t) + \eta \cdot \frac{\mathrm{d}\varepsilon(t)}{\mathrm{d}t} . \tag{3.3}$$

With the applied constant stress σ_0, the above equation can be written as

$$\frac{\sigma_0}{E} = \varepsilon + \frac{\eta}{E}\frac{\mathrm{d}\varepsilon}{\mathrm{d}t} . \tag{3.4}$$

The solution of this equation is

$$\varepsilon(t) = \frac{\sigma_0}{E}\left(1 - e^{-\frac{t}{\tau}}\right) . \tag{3.5}$$

Where τ is relaxation time and generally defined as $\tau = \frac{\eta}{E}$.

Eq. (3.5) describes the behavior of the time-dependent creep of rubber material as shown in Fig. 3.3.

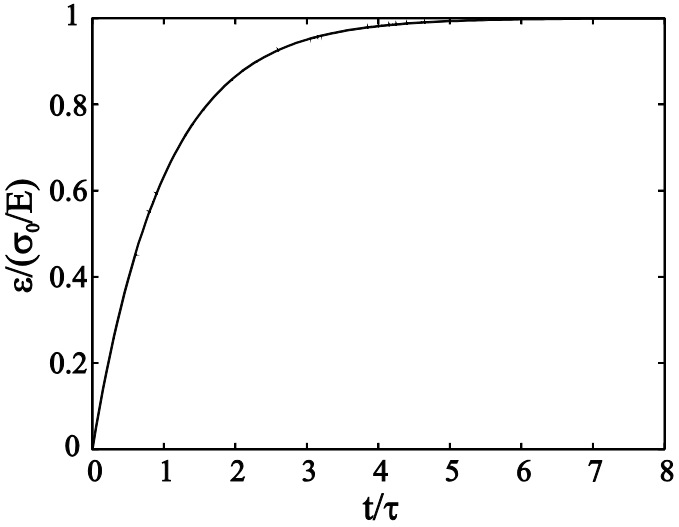

Fig. 3.3 Creep behavior of rubber with Kelvin model.

3.2 Contact between elastomer and a rigid body

We consider the contact between a viscoelastic half-space and a rigid profile. The generation of the rigid profile is presented in section 2.3.2. For simplification, the viscoelastic body, modeled with Kelvin element, is assumed to be flat. Under a normal force the rigid body is pressed into the elastomer and then dragged to move horizontally with a constant velocity (Fig. 3.5). What we are interested in is the frictional behavior and the dependence of the friction coefficient on the load, sliding velocity, material and system parameters.

The work in this section appears in paper [11] (Li, Q. *et al.* Friction between a viscoelastic body and a rigid surface with random self-affine roughness. *Phys. Rev. Lett.* 111, 034301 (2013)). My contribution to [11] (in accordance with the content of this section) is the following: Li Q carried out the numerical simulation. The details of the numerical calculation are described in section 3.2.1 including Fig. 3.4 to Fig. 3.6 and Eq. (3.6) to Eq. (3.10). Popov M and Filippov AE provided initial versions of the code. Popov VL and Li Q analyzed the simulation results (section 3.3.2) and formulated them in equations including Eq. (3.11) to Eq. (3.15). Li Q prepared the figures illustrated in Fig. 3.7 to Fig. 3.11. Popov VL, Filippov AE, Li Q and Kürschner S discussed the results (section 3.2.3) and gave an analytical support in Eq. (3.16) to Eq. (3.23). All the authors contributed in preparing the manuscript of paper [11].

3.2.1 Theoretical model

According to the principle of MDR, the elastomer is modeled as a row of independent elements with a small spacing Δx, each element consisting of a spring with normal stiffness $\Delta k_z = 4G\Delta x$ and a dashpot having the damping constant $\Delta\gamma = 4\eta\Delta x$ as shown in section 2.2.1, where G is the shear modulus and η, the viscosity of the elastomer (Fig. 3.4).

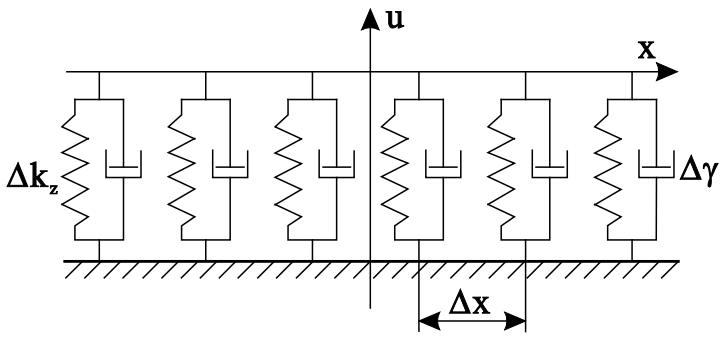

Fig. 3.4 Viscoelastic foundation of elastomer.

The counter body is a rough line having the power spectral density $C_{1D} \propto q^{-2H-1}$. This one-dimensional power density corresponds to the two-dimensional power density of the form $C_{2D} \propto q^{-2H-2}$. The spectral density was defined in the interval from $q_{\min} = 2\pi / L$, where L is the system size, to the upper cut-off wave vector $q_{\max} = \pi / \Delta x$. The spacing Δx determines the upper cut-off wave vector and is an essential physical parameter of the model. The characterization and generation of the rigid surface topography were described in detail in section 2.3.2. The periodic boundary conditions were used. The elastomer was pressed against the rigid surface with a constant normal force F_N and moved tangentially with a constant velocity v. A typical configuration of the contact is shown in Fig. 3.5.

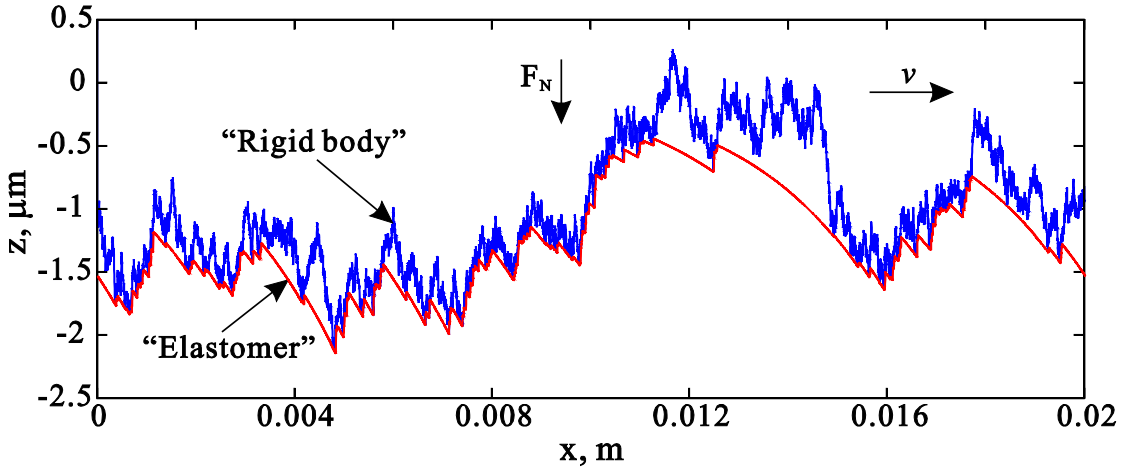

Fig. 3.5 One-dimensional contact between a rough surface and a visco-elastic elastomer. Note the difference in vertical and horizontal units.

If the rigid profile is given by $z = z(x - vt)$, and the profile of the elastomer by $u = u(x,t)$, then the normal force in each particular element of the viscoelastic foundation is given by

$$f = -4\Delta x\left\{Gu(x) + \eta\dot{u}(x,t)\right\}. \tag{3.6}$$

For the elements in contact with the rigid surface, this means that

$$f = 4\Delta x\left\{G\left[d - z(x,t)\right] + \eta v z'(x,t)\right\}, \tag{3.7}$$

where d is the indentation depth. For these elements, the condition of remaining in contact, $f > 0$, was checked in each time step. Elements out of contact were relaxed according to equation $f = 0$: $Gu(x) + \eta\dot{u}(x,t) = 0$, and the non-contact condition $u < z$ was checked. The indentation depth d was determined to satisfy the condition of the constant normal force

$$F_N = 4\int_{(\text{real cont})}\left[G\left(d - z(x)\right) + \eta v z'(x)\right]\mathrm{d}x, \tag{3.8}$$

where the integration is only over points in contact. The tangential force was calculated by multiplying the local normal force in each single element with the local surface gradient and subsequently summing over all elements in contact:

$$F_x = -4\int_{(\text{real cont})} z'(x)\left[G\left(d - z(x)\right) + \eta v z'(x)\right]\mathrm{d}x. \tag{3.9}$$

Due to the independence of the degrees of freedom, the algorithm is not iterative and there are no convergence problems.

The coefficient of friction is calculated as the ratio of tangential force (3.9) and normal force (3.8)

$$\mu = \frac{F_x}{F_N}. \tag{3.10}$$

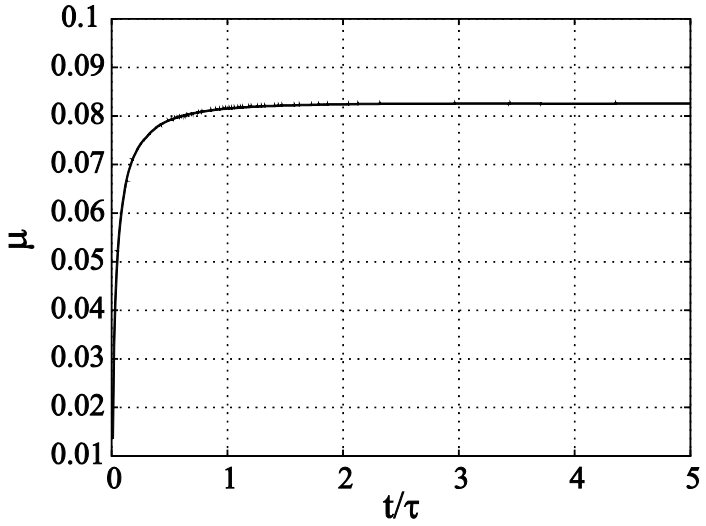

Fig. 3.6 Coefficient of friction changing with time.

Generally, the friction of coefficient changes with time: it gradually approaches a constant value in a steady state as seen in Fig. 3.6. To obtain a general law of friction, we consider only the value in the steady state. The details of dynamic contacts are shown in Chapter 4.

3.2.2 Numerical results

The one-dimensional model is computationally efficient and allows carrying out extensive parameter studies. The following ranges of parameters have been covered in the present study. The length of the system was $L = 0.02$ m and the number of elements $N = L/\Delta x$ was typically 5000 with exception of cases where the dependence on Δx was studied. Instead of viscosity, the relaxation time $\tau = \eta / G = 10^{-3}$ s was used. 11 values of Hurst exponent ranging from 0 to 1 were studied. All values shown below were obtained by averaging over 200 realizations of the rough surface for each set of parameters. Parameter studies have been carried out for 20 different normal forces F_N ranging from 10^{-3} to 10^{2} N, 20 values of the G modulus from 10^{3} to 10^{9} Pa, 20 values of rms roughness h from 10^{-9} to 10^{-5} m, and 20 values of the spacing Δx from 10^{-5} to 10^{-7} m, while in each simulation series only one parameter was varied. The presented results are based on approximately $3.5 \cdot 10^{6}$ single simulations with the total net computation time of about 50 h. It is well known that the maximum value of the coefficient of friction μ in the medium range of velocities is proportional to the rms gradient of the surface profile [10]. We, therefore, present the normalized friction coefficient $\mu / \nabla z$ instead of μ in this thesis.

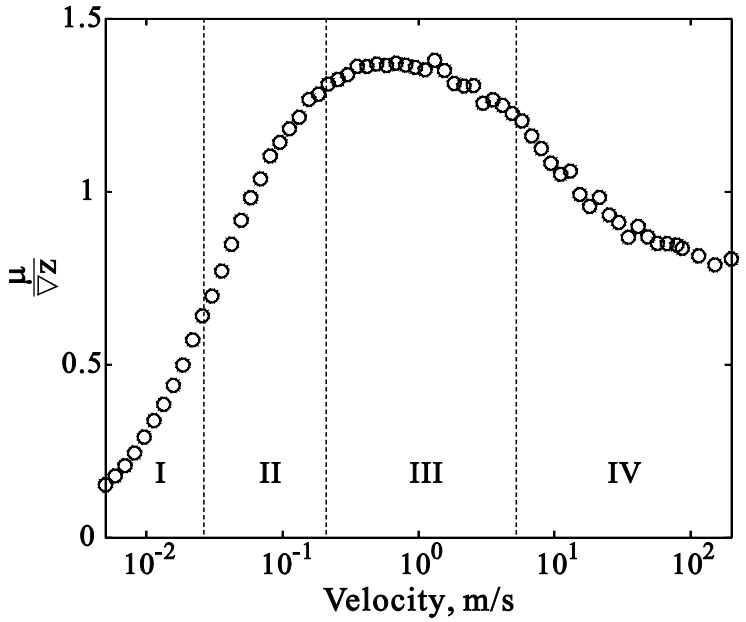

Fig. 3.7 A typical dependence of the normalized coefficient of friction on the velocity. In this particular case, the results were obtained for the following set of parameters: $F_N = 1.5$ N, $G = 10^7$ Pa, $h = 5 \cdot 10^{-7}$ m, and $H = 0.7$.

A typical dependence of the coefficient of friction on the sliding velocity is shown in Fig. 3.7. At first, it increases linearly with velocity (region I), it then achieves a plateau (region III) and decreases again to a new constact value (region IV). We also marked an intermediate region (II) where transition from the linear velocity dependence to the plateau takes place. This region covers one decade of velocities, and the coefficient of friction increases here by a factor of two. Fig. 3.8 shows the velocity dependence in double logarithmic scale for 6 different Hurst exponents. It is obvious that at small velocities, the coefficient of friction increases linearly with velocity. The absence of the decreasing region IV in Fig. 3.7 (and Fig. 3.8 at high loads) is only due the fact that for high forces this region is outside the scope of practical velocities and is therefore not shown in these figures.

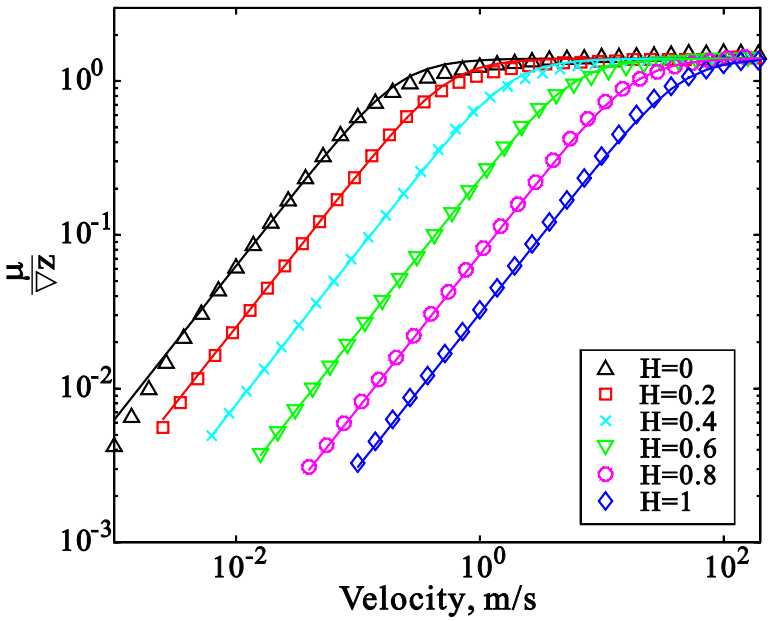

Fig. 3.8 Dependence of friction coefficient on velocity for different Hurst exponents and $F = 10$ N , $G = 10^7$ Pa , $h = 5 \cdot 10^{-7}$ m . Solid lines correspond to the analytical approximation (3.17).

Fig. 3.9 presents velocity dependencies of the coefficient of friction for 20 different normal forces. One can see that the form of the dependence for different forces is approximately the same, only shifted along the axis of the logarithmus of velocity. There are two distinctly different regions: in zone 1 there is a partial contact of the rigid surface and the elastomer, while in the zone 2 they are in complete contact. In both of the zones, the shift factor increases linearly with the logarithm of force, the coefficient of friction, thus, being a power function of the normal force. Simulations with different rms gradients of the surface (which were varied by changing the spacing Δx) show that the coefficient of friction in this region is very accurately proportional to ∇z^2 and depends on the force and shear modulus only over the ratio F_N / G. The only form of the dependence which fits these empirical observations and meets the dimensional demands is

$$\mu = \beta \frac{\tau v \nabla z^2}{h} \left(\frac{GhL}{F_N} \right)^{\alpha}, \tag{3.11}$$

where α and β are dimensionless constants. Empirical values of these constants extracted from numerical data are shown in Fig. 3.10.

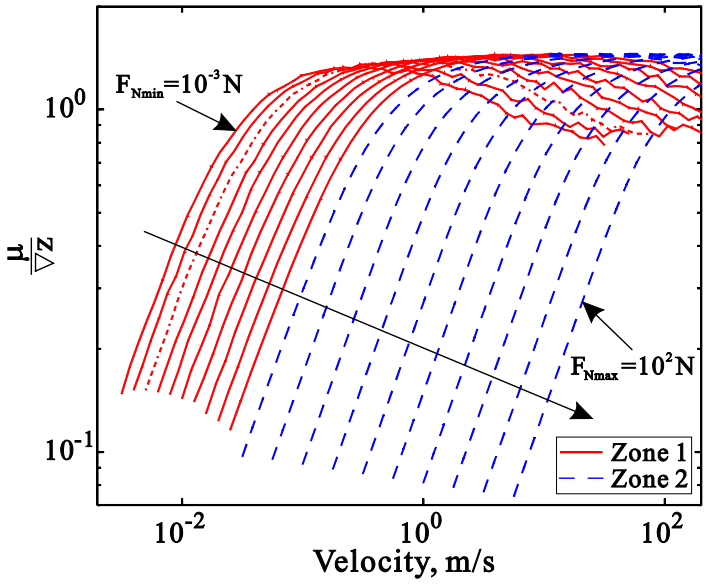

Fig. 3.9 Double logarithmic presentation of the dependence of the normalized friction coefficient on velocity for 20 exponentially increasing normal forces ranging from 10^{-3} to 10^{2} N , as indicated by the arrow ($G = 10^{7}$ Pa , $h = 5 \cdot 10^{-7}$ m , and $H = 0.7$). The dotted line (third from the left) corresponds to the data shown in Fig. 3.7.

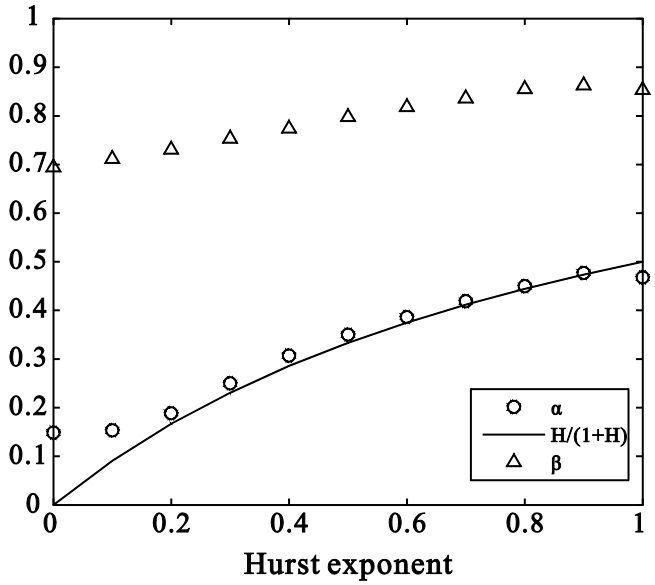

Fig. 3.10 Dependence of α and β (see Eq. (3.11) on the Hurst exponent in zone 1 (see Fig. 3.9). Analytical estimation of the exponent α according to (3.13) is shown with bold line. For $0.2 < H < 0.8$, it fits numerical data very well.

3.2.3 Theoretical analysis and discussions

Let us support this result with an analytical estimation. At low velocities, the values of z in the border points of each partial contact region in the Eq. (3.9) are the same ($z = d$),

thus, the integral $\int_{\text{real cont}} z'(x)\left[G\left(d-z(x)\right)\right]\mathrm{d}x$ vanishes identically. For the coefficient of friction we get

$$\mu = \frac{4L_{\text{cont}}\eta\nabla z_{\text{cont}}^2}{F_N}\cdot v\,. \tag{3.12}$$

Here, L_{cont} is the total contact length, and ∇z_{cont} the rms slope in the region of real contact. The rms slope is dominated by the short wavelength part of the spectrum. It can be approximately replaced by the average rms slope of the entire surface $\nabla z_{\text{cont}} \approx \nabla z$. At the end of the section, we discuss the weak dependence of ∇z_{cont} on loading parameters in more detail.

For small forces, in zone 1, the contact length is a power function of the normal force [68]: $L_{\text{cont}} \propto F^{1/(1+H)}$, and the coefficient of friction will be given by $\mu \propto F^{-H/(1+H)}$. Comparing this with Eq. (3.11) provides an analytical estimation for the exponent α:

$$\alpha = \frac{H}{1+H}\,. \tag{3.13}$$

For large normal forces, in zone 2, the contact length achieves a saturation value of $L_{\text{cont}} = L$. The coefficient of friction becomes

$$\mu = \frac{4L\eta\nabla z^2}{F_N}\cdot v\,, \tag{3.14}$$

which is exactly confirmed by numerical simulations. Finally, in the plateau region, the coefficient of friction shows only a weak dependence on the Hurst exponent (Fig. 3.11). In the range of $0.2 < H < 0.8$ and for not too small forces, it is almost constant and can be approximated as

$$\mu \approx \sqrt{2}\cdot\nabla z_{\text{cont}}\,. \tag{3.15}$$

This result has a simple physical meaning. In the plateau region, the elastomer behaves practically as a viscous fluid: the elasticity does not play any role and all contacts are "one-sided." The normal and tangential forces reduce to $F_x = 4\int_{(\text{real cont})}\eta v\left(z'(x)\right)^2\mathrm{d}x$, $F_N = 4\int_{(\text{real cont})}\eta v\left|z'(x)\right|\mathrm{d}x$. For the normalized coefficient of friction we get

$$\mu = \frac{\int_{(\text{real cont})}\left(z'(x)\right)^2\mathrm{d}x}{\int_{(\text{real cont})}\left|z'(x)\right|\mathrm{d}x} = \nabla z_{\text{cont}}\,\frac{\left(\int_{(\text{real cont})}\left(z'(x)\right)^2\mathrm{d}x\right)^{1/2}\cdot L_{\text{cont}}^{1/2}}{\int_{(\text{real cont})}\left|z'(x)\right|\mathrm{d}x}\,. \tag{3.16}$$

For an exponential probability distribution function of the gradient of the surface, the ratio of $\frac{\left(\int_{(\text{real cont})} \left(z'(x)\right)^2 \mathrm{d}x\right)^{1/2} \cdot L_{\text{cont}}^{1/2}}{\int_{(\text{real cont})} \left|z'(x)\right| \mathrm{d}x}$ in (3.16) is equal to $\sqrt{2}$, in accordance with (3.15), and it depends only weakly on the form of the distribution function.

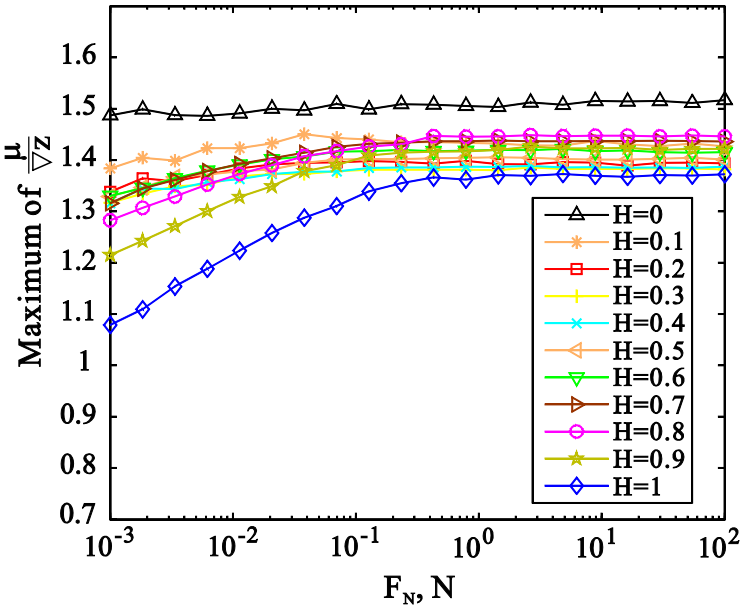

Fig. 3.11 Dependence of the normalized coefficient of friction in the region III (plateau). The coefficient of friction decreases at very small forces. This effect is closely related to the decrease of the coefficient of friction at high sliding velocities, Fig. 3.7, region IV.

The results (3.11), (3.13), (3.14) and (3.15) can be combined in the following equation providing an interpolation between the three regions I, II, and III:

$$\mu = \left[\frac{1}{2\nabla z_{\text{cont}}^2} + \left(\frac{F_N}{4L\eta\nabla z_{\text{cont}}^2 v} \right)^2 + \left(\frac{h}{\beta\tau\nabla z_{\text{cont}}^2 v} \left(\frac{F_N}{GhL} \right)^{\frac{H}{1+H}} \right)^2 \right]^{-1/2} . \tag{3.17}$$

The quality of this interpolation can be seen in Fig. 3.8 where the numerical results for six Hurst exponents are plotted together with analytical dependencies (3.17). This equation can be rewritten in the dimensionless form

$$\overline{\mu} = \left[1 + \frac{\left(\left(\overline{F}_N/4\right)^2 + \left(\overline{F}_N\right)^{\frac{2H}{1+H}} \right)}{\overline{v}^2} \right]^{-1/2} , \tag{3.18}$$

with a normalized coefficient of friction $\overline{\mu} = \mu \Big/ \left(\sqrt{2} \nabla z_{\text{cont}} \right)$, dimensionless velocity

$$\overline{v} = \frac{\tau v \nabla z_{\text{cont}}}{\sqrt{2} h}, \tag{3.19}$$

and dimensionless force

$$\overline{F}_N = \frac{F_N}{GhL}. \tag{3.20}$$

Let us discuss the physical meaning of the quantities $\overline{v}$ and $\overline{F}_N$. The condition $\overline{F}_N \approx 1$ gives the order of magnitude of the force at which complete contact is achieved, while the condition $\overline{v} \approx 1$ determines the order of magnitude of velocity at which the elastomer is detached from the rigid surface on the trailing side of any asperity and all the contacts become "one-sided." Indeed, according to (3.7), the condition of detachment $f = 0$ means $d - z(x) + \eta v z'(x) = 0$. Taking into account that $d - z$ has the order of magnitude of h and z' has the order of magnitude of ∇z_{cont}, we come to the conclusion that the one-sided detachment of the elastomer will occur if $(\eta / G) v \nabla z_{\text{cont}} > h$ or $\overline{v} > 1$. Note that the same conditions are valid in the corresponding three-dimensional problem: for achieving the plateau value of contact stiffness ($\overline{F}_N \approx 1$, [68]) and for the one-sided detachment of the elastomer ($\overline{v} \approx 1$).

Let us discuss the decrease of the coefficient of friction beyond the region of validity of approximation (3.18), at large velocities (region IV in Fig. 3.7). Such a decrease at large velocities is typical for elastomer friction and is usually associated with a decrease in the "rheological factor" $\operatorname{Im} G(\omega) / |G(\omega)|$ at high frequencies [26], where $G(\omega)$ is the complex modulus of the elastomer and $\operatorname{Im} G(\omega)$, its imaginary part. For the case of the Kelvin body, however, the rheological factor is equal to $\eta\omega / \sqrt{G^2 + (\eta\omega)^2}$; it increases monotonously and tends towards 1 at high frequencies. In this case, the decrease of the coefficient of friction is not related to the rheology but rather to the dependence of the rms slope on the size of the real contact. Indeed, for randomly rough surfaces, the rms slope in the contact region can be estimated as

$$\nabla z_{\text{cont}} = \left(2 \int_{q_{\text{cont}}}^{q_{\max}} C_{1D}(q) q^2 \mathrm{d}q \right)^{1/2} \propto \left(\frac{\left[q_{\max}^{-2(1-H)} - q_{\text{cont}}^{-2(1-H)} \right]}{2(1-H)} \right)^{1/2}, \tag{3.21}$$

where the lower integration limit $q_{\text{cont}} \approx 2\pi / L_{\text{cont}}$ decreases with increasing size of the real contact. For $0 < H < 1$, the integral (3.21) depends only weakly on the lower integration limit unless the contact length becomes extremely small so that q_{cont}

approaches $q_{\max}$. Thus, the coefficient of friction in the region of plateau will decrease with decreasing indentation depth. This happens either at extremely high sliding velocities (Fig. 3.7, region IV) or at extremely low normal forces as illustrated in Fig. 3.11. The dependence of ∇z_{cont} on the contact size and, thus, on velocity and force is less pronounced for small Hurst exponents, $H \approx 0$, and gets stronger for $H \approx 1$. Note that the increase of rms slope with increasing indentation is closely associated with the assumption of the "randomness" of roughness, as the estimation (3.21) is only valid if the Fourier components of roughness with different wave vectors have uncorrelated phases. One can say that randomly rough surfaces are always rougher on the slopes of waviness than on the summits. Real surfaces, on the contrary, may have different kinds of correlated roughness. One can easily imagine a surface, which is rougher on the summits than on the slopes; for such surfaces, the rms slope of roughness would decrease with indentation. The general and robust statement, which is independent of the kind of the roughness correlation, is only that the rms slope in the contact region is a function of indentation depth and, thus, a function of the non-dimensional force (3.20). This statement even remains valid if the linear viscoelastic behavior of the material breaks down at the micro-scale. Indeed, the statement that the frictional force will depend on the indentation depth is correct for any kind of processes at the micro-scale. The indentation depth, however, is governed by the contact stiffness which is dominated by the largest wavelength in the power spectrum of the roughness. The general conclusion that the non-dimensional force (3.20) is a governing parameter of the friction process will, therefore, remain valid independently of the particular character of the microscopic processes. We can summarize our results to the following general scaling relation:

$$\mu = \nabla z_{\text{cont}}\left(\overline{F}_N\right) \cdot g\left(\overline{v} \,/\, f\left(\overline{F}_N\right)\right), \tag{3.22}$$

or, in explicit form,

$$\mu = \nabla z_{\text{cont}}\left(\frac{F_N}{GhL}\right) \cdot g\left(\frac{\tau v \nabla z_{\text{cont}}}{\sqrt{2}h} \Big/ f\left(\frac{F_N}{GhL}\right)\right). \tag{3.23}$$

This scaling relation means that the dependence of the coefficient of friction on velocity in the double logarithmic presentation has the same form for different values of all parameters appearing in this equation: force F_N, size of the system L, and relaxation time τ. Changing of any of these parameters will only shift the curves horizontally by the factor of $\approx \log\left(\frac{\tau \nabla z}{\sqrt{2}h} \Big/ f\left(\frac{F_N}{GhL}\right)\right)$ and vertically by the factor of $\log \nabla z_{\text{cont}}\left(F_N / GhL\right)$. In particular, the curves will be shifted by changes of temperature (which influences the relaxation time). The shifting procedure with regard to temperature is well known and widely used in the physics of friction of elastomers for constructing “master curves” describing the friction coefficient at any velocity and temperature (see, e.g., [69]). Eq.

(3.23) means that the master curve procedure can be generalized to dependencies on other loading and system parameters. While the particular form (3.17) of the law of friction is limited by the assumptions of simple visco-elastic rheology, the general scaling relation (3.23) should have a wider range of application and it should be possible to validate it experimentally.

3.3 Contact between elastomer and rigid bodies having different macroscopic shape

In section 3.2 we studied the friction law of elastomer contacting with a macroscopically plane rough surface, now we consider other shapes of contacting body: rough parabolic and conical profile. The model for elastomer is still same as in the previous Section, i.e., Kelvin body.

The work in this section appears in paper [12] (Popov, V. L., Lars, V., Li, Q., Chai, Y. S. & Popov, M. Generalized law of friction between elastomers and differently shaped rough bodies. *Sci. Rep.* 4, 3750 (2014). My contribution to [12] (in accordance with the content of this section) is the following: Li Q carried out the numerical simulation. The details of model is described in section 3.3.1 and the results are illustrated in Fig. 3.12, Fig. 3.14 and Fig. 3.15 and formulated in Eq. (3.38) to Eq. (3.40) (section 3.3.2). Voll L set up the experiment (Fig. 3.16) and carried out the measurement (section 3.3.4). Popov VL, Voll L and Li Q analyzed the collected data (Fig. 3.17 to Fig. 3.19). Li Q prepared the Fig. 3.12, Fig. 3.14, Fig. 3.15 and Fig. 3.17 to Fig. 3.19. Popov M provided initial version of the simulation program. All authors of paper [12] discussed the results and contributed in preparing the manuscript of [12].

3.3.1 Theoretical model

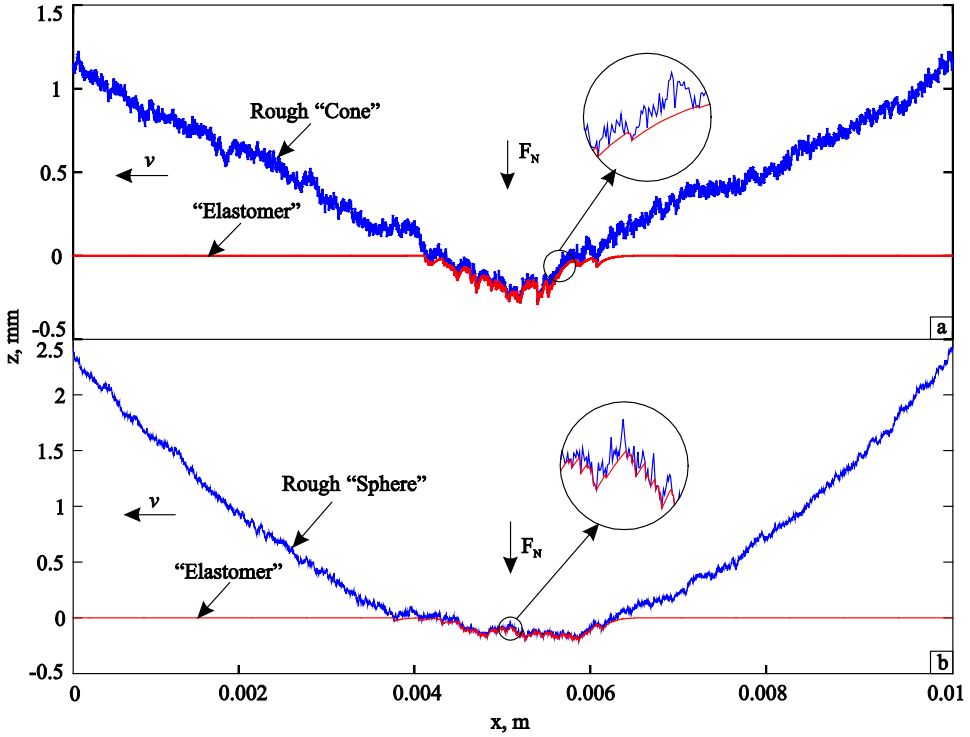

Fig. 3.12 One-dimensional contact between a viscoelastic body and (a) a rough "cone"; (b) a rough "sphere". The configuration is shown for the following parameters defined in text: $F_N = 1$ N , $G = 10^6$ Pa , $v = 0.1$ m/s , $h = 5 \cdot 10^{-5}$ m , $\tau = 10^{-3}$ s , (a) $\theta = 10°$ and $H = 0.1$; (b) $R = 10^{-2}$ m and $H = 0.2$. Note the difference in vertical and horizontal units.

Let us consider a rigid indenter having the form

$$z = g(x) = g_0(x) + h(x) \tag{3.24}$$

consisting of the macroscopic power-shaped profile

$$g_0(x) = c_n |x|^n \tag{3.25}$$

and a superimposed roughness $h(x)$, as shown in Fig. 3.12. It can be said that $g_0(x) = 0$ for the rigid profile in last section 3.2.

Coordinates x and z are measured from the minimum of the macroscopic form, so that $g_0(0) = 0$. The ensemble average of the rough profile is assumed to be zero: $\langle h(x) \rangle = 0$. The roughness was assumed to be a self-affine fractal having the power spectral density $C_{1D} \propto q^{-2H-1}$, and it is same as the rigid profile in the previous Section. We assume that the indentation depth of the indenter, d , is much larger than the rms value of the roughness, $h << d$. This means that the large-scale configuration of the contact is primarily determined by the macroscopic form of the indenter and does not depend on the roughness (Fig. 3.13).

The rigid indenter is pressed into a viscoelastic foundation to the depth d and is moved in tangential direction with velocity v (Fig. 3.12), so that at time t it is described by the equation

$$z = g(x+vt) - d = g(\tilde{x}) - d\,. \tag{3.26}$$

For convenience, we introduced the coordinate $\tilde{x} = x + vt$ in the coordinate system moving together with the rigid indenter.

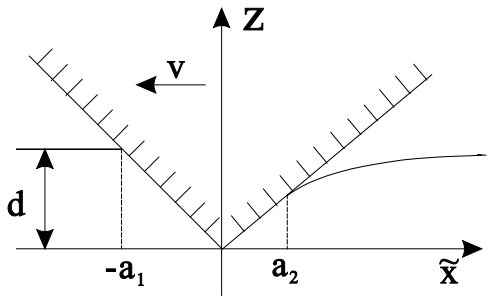

Fig. 3.13 A "large scale picture" of a contact of an elastomer and a rigid conical indenter moving left with velocity v.

The normal force in each particular element of the viscoelastic foundation is given by

$$f = -4\Delta x\left[Gu(x) + \eta\dot{u}(x,t)\right]. \tag{3.27}$$

where u is the vertical displacement of the element of the viscoelastic foundation. For elements in contact with the rigid surface, this means that

$$f = 4\Delta x\left[G\left(d - g(\tilde{x})\right) - \eta v g'(\tilde{x})\right]. \tag{3.28}$$

The normal and the tangential force are determined through equations

$$F_N = 4\int_{-a_1}^{a_2}\left[G\left(d - g(\tilde{x})\right) - \eta v g'(\tilde{x})\right]\mathrm{d}\tilde{x}\,, \tag{3.29}$$

$$F_x = -4\int_{-a_1}^{a_2} g'(\tilde{x})\left[G\left(d - g(\tilde{x})\right) - \eta v g'(\tilde{x})\right]\mathrm{d}\tilde{x}\,. \tag{3.30}$$

3.3.2 Numerical results and discussions

(a) Friction at low sliding velocity

We first consider the force of friction at very low velocities. The contact configuration is then approximately equal to the static contact. The uppermost left and uppermost right points $-a_1$ and a_2 of the contact (see Fig. 3.13) are then both determined by the condition $g(-a_1) - d \approx g(a_2) - d = 0$. Because of the relation $g(-a_1) = g(a_2)$, the integrals $\int_{-a_1}^{a_2}\eta v g'(\tilde{x})\mathrm{d}\tilde{x}$ and $\int_{-a_1}^{a_2} g'(\tilde{x})G\left(d - g(\tilde{x})\right)\mathrm{d}\tilde{x}$ in (3.29) and (3.30) vanish. Therefore,

$$F_N = 4\int_{-a_1}^{a_2} G\left(d - g(\tilde{x})\right)\mathrm{d}\tilde{x} \approx 4\int_{-a_1}^{a_2} G\left(d - g_0(\tilde{x})\right)\mathrm{d}\tilde{x}\,, \tag{3.31}$$

$$F_x = 4\eta v\int_{-a_1}^{a_2} \left[g'(\tilde{x})\right]^2 \mathrm{d}\tilde{x} \approx 4\eta v\int_{-a_1}^{a_2} \left[\,{g_0}'(\tilde{x})^2 + h'(\tilde{x})^2\,\right]\mathrm{d}\tilde{x}\,. \tag{3.32}$$

We assume that the gradient of the macroscopic shape of the indenter is much smaller than that of the roughness, $\left\langle {g_0}'(x)^2 \right\rangle << \left\langle h'(x)^2 \right\rangle$, so that

$$F_x \approx 4\eta v\int_{-a_1}^{a_2} h'(x)^2\,\mathrm{d}\tilde{x} \approx 4\eta v \nabla z^2 L_{\mathrm{cont}}\,, \tag{3.33}$$

where ∇z is the rms value of the surface gradient and $L_{\mathrm{cont}} = a_1 + a_2$ the contact length. For the coefficient of friction, we get

$$\mu \approx \frac{4L_{\mathrm{cont}}v\eta}{F_N}\nabla z^2 = \frac{4GL_{\mathrm{cont}}v\tau}{F_N}\nabla z^2\,. \tag{3.34}$$

This equation shows, that both the macroscopic shape of the indenter and the microscopic properties of surface topography determine the coefficient of friction: the contact length is primarily determined by the macroscopic properties (shape of the body and the normal force) while the rms gradient is primarily determined by the roughness at the smallest scale.

(b) Friction at high sliding velocity

Consider the opposite case of high sliding velocities. If the indentation depth is much larger than the roughness of the profile, then we see from Eq. (3.28) that one-sided detachment of the elastomer from the indenter will take place if

$$d\,/\left(\tau v \nabla z\right) \approx 1 \tag{3.35}$$

where ∇z is the characteristic value of the surface gradient. In that case, the friction coefficient achieves an approximately constant value of

$$\mu \approx \sqrt{2}\nabla z\,. \tag{3.36}$$

For the macroscopic power law shape, the indentation depth and contact radius are given by

$$a = \left(\frac{F_N\left(n+1\right)}{8Gc_n n}\right)^{\frac{1}{n+1}},\; d = \left(\frac{F_N\left(n+1\right)c_n^{\,1/n}}{8Gn}\right)^{\frac{n}{n+1}}. \tag{3.37}$$

Substituting the contact length $L_{\mathrm{cont}} = 2a$ into Eq. (3.34), we obtain the coefficient of friction at low velocities:

$$\bar{\mu} = \xi \,, \tag{3.38}$$

where we introduced dimensionless variables

$$\bar{\mu} = \frac{\mu}{\sqrt{2}\nabla z}, \quad \xi = \frac{v\tau\nabla z}{\sqrt{2}}\left(\frac{8G}{F_N}\right)^{\frac{n}{n+1}}\left(\frac{n+1}{c_n n}\right)^{\frac{1}{n+1}} \tag{3.39}$$

(c) Simulation results

Numerical simulations presented in Fig. 3.14 for the case of a rough cone show that all data in the coordinates $(\bar{\mu}, \xi)$ collapse to one master curve with a slope equal to one. The validity of Eq. (3.38) was numerically confirmed for the following ranges of parameters. The reference length of the system was $L = 0.01$ m and the number of elements $N = L/\Delta x$ was typically 5000. 11 values of Hurst exponent ranging from 0 to 1 were studied. All values shown below were obtained by averaging over 200 realizations of the rough surface for each set of parameters. Parameter studies have been carried out for 20 different normal forces F_N ranging from 10^{-1} to 10^{1} N, 20 values of the G modulus from 10^5 to 10^7 Pa, 20 values of rms roughness h from 10^{-6} to 10^{-4} m, and 20 values of the spacing Δx from 10^{-7} to 10^{-5} m, 20 values of angles θ ranging from 5 to 75°, and 20 relaxation times τ ranging from 10^{-4} to 10^{-2} s, while in each simulation series only one parameter was varied.

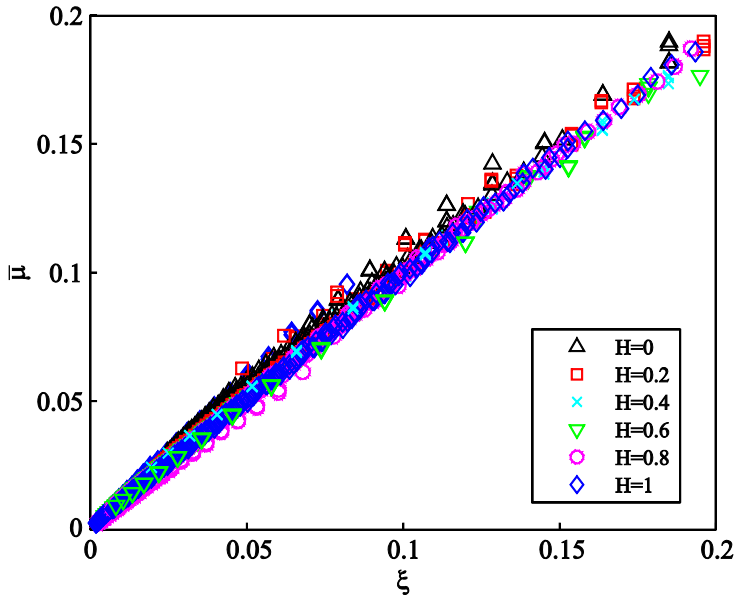

Fig. 3.14 Dependence of $\bar{\mu}$ on ξ at low velocities. Different symbols correspond to different sets of parameters H, v, F_N, G, θ, τ and ∇z. All data collapse to one master curve described by Eq. (3.38).

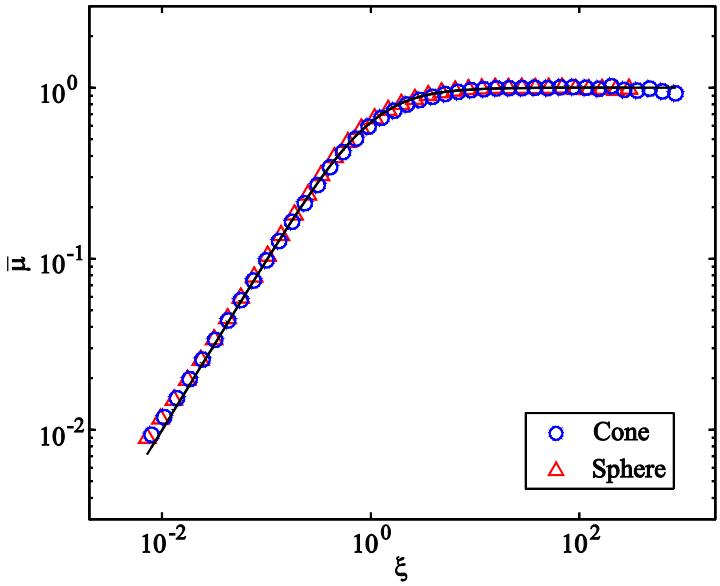

Fig. 3.15 Dependence of $\bar{\mu}$ on ξ for the following set of parameters: $F_N = 10$ N, $G = 10^6$ Pa, $h = 5 \cdot 10^{-5}$ m, $\tau = 10^{-3}$ s, $H = 0.4$ and $\theta = 10°$ (conical indenter) or $R = 10^{-2}$ m (parabolic indenter). The solid line corresponds to the analytical approximation (3.40) with $\alpha = 1.5$.

It is easily seen that we can get both limits (3.34) and (3.36) by writing

$$\frac{\mu}{\sqrt{2}\nabla z} = \left(1 + \xi^{-\alpha}\right)^{-1/\alpha}. \tag{3.40}$$

where α is a dimensionless fitting parameter. Numerical simulations (Fig. 3.15) show that this dependence is valid for all parameter sets used in our simulations, while the best fit is achieved with $\alpha = 1.5$. Interestingly, parameter α seems not to depend on the macroscopic shape of the indenter.

3.3.3 Friction law for a general linear rheology and the "force master curves"

Now we discuss friction of elastomers with a more realistic rheology, which is characterized by the frequency dependent complex shear modulus $G(\omega) = G'(\omega) + iG''(\omega)$, where G' is the storage modulus, and G'' the loss modulus [10]. At low frequencies, the shear modulus tends towards its static value G_0. For simplicity, we will assume that the macroscopic contact mechanics of the indenter is completely governed by the static shear modulus G_0, which is correct for sufficiently small sliding velocities. On the other hand, the frictional force is almost completely determined by the smallest wavelength components in the spectrum of roughness and thus by high frequency rheology. The frictional force at low velocities can be therefore estimated by using Eq. (3.33) and substituting $\eta \to G''(\omega_{\max}) / \omega_{\max}$, where $\omega_{\max} \approx v q_{\max}$:

$$F_x \approx \frac{4G''(\omega_{\max})v\nabla z^2 L_{\text{cont}}}{\omega_{\max}} = \frac{4G''(q_{\max}v)\nabla z^2 L_{\text{cont}}}{q_{\max}}. \tag{3.41}$$

The contact length is completely determined by the macroscopic contact mechanics of the indenter, Eq. (3.37), where we substitute the constant static shear modulus G_0. For the friction coefficient, we therefore get

$$\mu = \frac{4G''(q_{\max}v)}{q_{\max}F_N}\left(\frac{F_N(n+1)}{8G_0c_n n}\right)^{\frac{1}{n+1}}\nabla z^2. \tag{3.42}$$

At high frequencies, the plateau value of $\sqrt{2}\nabla z$ will be achieved. An interpolation between (3.42) and this value is provided by

$$\frac{\mu}{\sqrt{2}\nabla z} \approx \left(1+\left[\frac{q_{\max}F_N}{2\sqrt{2}G''(q_{\max}v)\nabla z}\left(\frac{8G_0c_n n}{F_N(n+1)}\right)^{\frac{1}{n+1}}\right]^{\alpha}\right)^{-1/\alpha} \tag{3.43}$$

with $\alpha \approx 1.5$. This Eq. shows that the coefficient of friction for rigid bodies having macroscopic power-law shape has the general form

$$\mu \approx Q(F_N \cdot p(v)) \tag{3.44}$$

where $p(v)$ is a function of velocity, which depends on the rheological properties of the elastomer. Since $F_N \cdot p(v) = \exp\left(\log F_N + \log p(v)\right)$, this means that the dependencies of the coefficient of friction as a function of $\log F_N$ will have the same shape for arbitrary velocities, only shifted along the $\log F_N$-axis by a velocity-dependent shift factor. This property gives the possibility to construct dependencies of the coefficient of friction on the normal force and the sliding velocity using a "master curve procedure" similar to those used for determining dependencies of the coefficient of friction on velocity from measurements at different temperatures [23]: Experimental results for the friction coefficient are presented as a function of $\log F_N$ at various velocities in Fig. 3.17. Following this hypothesis, we assume that at different velocities, the measured curves are only shifted pieces of the same curve. Now, one attempts to shift the curves such that they form a single "master curve" (Fig. 3.18). The resulting curve gives the dependence of the coefficient of friction in a wider range of forces than the range used in the experiment. At the same time, the shift factors at different velocities will provide the dependence of the coefficient of friction on velocity. The result is a complete dependence of the coefficient of friction in a wide range of velocities and forces. Repeated for different temperatures and using the standard master curve procedure [23], this will lead to restoring the complete law of friction as function of velocity, temperature and normal

force. However, in the present thesis, we avoid the well discussed subject of the temperature dependence and concentrate our efforts completely on the force dependence.

Note that the main logic of the result (3.44) is not dependent on the details of the model and even on its dimensionality. The scaling relation (3.44) follows solely from the assumption that the macroscopic form of the contact is determined by the macroscopic properties of material and do not depend on microscopic details, and on the other hand, that the microscopic properties are determined mainly by the indentation depth. These general assumptions are equally valid for one-, two- and three dimensional models. Below we explain this important point in more detail.

It is well known, that if a rigid body of an arbitrary shape is pressed against a homogeneous elastic half-space then the resulting contact configuration is only a function of the indentation depth d. At a given indentation depth, the contact configuration does not depend on the elastic properties of the medium, and it will be the same even for indentation of a viscous fluid or of any linearly viscoelastic material. This general behavior was recognized by Lee and Radok [70] [71] and was verified numerically for fractal rough surfaces [72]. Further, the contact configuration at a given depth remains approximately invariant for media with thin coatings [73] or for multi-layered systems, provided the difference of elastic properties of the different layers is not too large [74]. In [75], it was argued that this is equally valid for media which are heterogeneous in the lateral direction (along the contact plane). Along with the contact configuration, all contact properties including the real contact area, the contact length, the contact stiffness, as well as the rms value of the surface gradient in the contact area will be unambiguous functions of the indentation depth. The indentation depth is thus a convenient und robust "governing parameter" for contact and frictional properties of media with linear rheology. Note, that this is equally valid for tangential contact. This can easily be illustrated with the example of contact of a rigid body with an incompressible elastic half-space: For a circular contact with an arbitrary radius a, the ratio of the normal stiffness k_z and the tangential stiffness k_x is constant and given by the Cattaneo-Mindlin factor [76] [77], for incompressible media $k_z / k_x = 1.5$. From this follows that for a frictional contact with the coefficient of friction μ, the maximum tangential displacement to the onset of complete sliding is determined solely by the indentation depth and is equal to $u_{x,\max} = 1.5\mu d$. This result does not depend on the form of the body and is valid for arbitrary bodies of revolution [78] and even for randomly rough fractal surfaces [79]. This fact, that the contact configuration is solely determined by the indentation depth is as a matter of fact the only physical reason needed to get the simple scaling relations for the coefficient of friction between rough rigid bodies and linearly viscoelastic elastomers described by Eq. (3.44). While the particular form (3.43) can depend on the model used, the general

functional form (3.44) is a universal one and is not connected with the method of dimensionality reduction used in this thesis.

3.3.4 Experimental

The experiment described in the following was set up and carried out by Voll L [12] (…Voll, Li et.al. Sci. Rep. 4, 3750, 2014). For completeness of the description, I introduce here his measurement results.

Our numerical and theoretical analysis shows that under some conditions the dependencies of the coefficient of friction on the normal force, presented in double logarithmic axes, is self-similar at different velocities and can be mapped onto each other by a simple shifting along the force axis. To prove this hypothesis, we measured the coefficient of friction between a band of polyurethane (PU) and a steel ball with radius $R = 50$ mm.

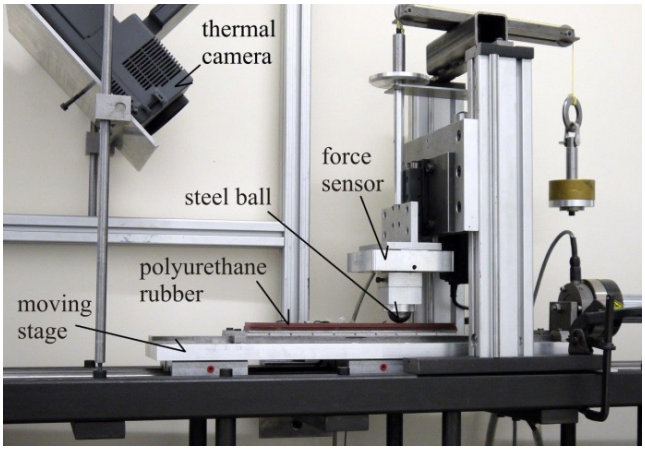

Fig. 3.16 Experimental set-up for measuring the coefficient of friction. (Set up by Voll. L [12])

The experimental set-up for measuring elastomer friction is shown in Fig. 3.16. The rubber band with a size of $300 \times 50 \times 5$ mm was glued to a moving stage using solvent-free two-component epoxy glue. The maximum pressure in the contact area was, in all experiments, at least one order of magnitude smaller than the latter, so that there was no plastic deformation of rubber. The stage could be moved with the aid of a hydraulic actuator with controlled velocity in the range of $5 \cdot 10^{-4}$ m/s to 0.58 m/s. The normal and tangential forces were measured with a 3D force sensor, on which the steel ball was mounted. The ambient temperature was 25.5 °C (± 0.5) and the relative air humidity 30% (± 5). Under these conditions the dynamic friction coefficient was measured at constant normal force and horizontal velocity. A total of 1680 measurements were taken. Data for any parameter set (normal force and temperature) was averaged over six measurements. Every measurement series was started at the smallest normal force, and increased in steps. At every level of normal force, the measurement was made with 28 horizontal velocities. Before proceeding to the next force level the material was examined

for wear both visually and with a microscope, and cleaned with pressurized air. At low normal forces wear was virtually non-existent, and remained weak even at higher forces. Chemical cleaning agents were not used to treat the surface of the rubber.

Measurements were carried out in a smaller velocity range of $3 \cdot 10^{-3}$ m/s to $2 \cdot 10^{-2}$ m/s for normal forces in the range of 1 N to 100 N. The lower velocity bound was chosen because the sliding at lower velocities was instationary. The maximum velocity was chosen to avoid significant temperature changes in the contact. The local temperature rise due to frictional heat can be estimated as $\Delta T \approx 2\mu G_0 dv / \lambda$, where $\lambda \approx 20$ $\mathrm{Wm^{-1}K^{-1}}$ is the thermal conductivity of the steel ball [10], which almost completely controls the thermal flow, and $G_0 \approx 3 \cdot 10^6$ Pa the static shear modulus of the used rubber. For the largest force of $F_N = 10^2$ N, we get an indentation depth of $d = \left(3F_N / 16 G_0 R^{1/2}\right)^{2/3} \approx 4 \cdot 10^{-5}$ m. With $\mu \approx 0.5$ and $v = 10^{-2}$ m/s we can estimate the average temperature rise as $\Delta T \approx 0.06$ K. Maximum temperature changes in micro contacts can be estimated as $\Delta T \approx 2\mu G_\infty h_0 v / \lambda$, where $G_\infty \approx 1.5 \cdot 10^9$ Pa is the glass modulus [80] of the used rubber and $h \approx 10^{-7}$ m the rms roughness of the ball, which was determined using a white light interferometric microscope. For velocity $v = 10^{-2}$ m/s we get an estimation $\Delta T \approx 0.08$ K which is of the same order of magnitude as the average temperature rise. Due to repeated sliding, the temperature change can get larger than the above estimation. The temperature changes of the rubber surface were controlled in experiments by an infrared camera (see Fig. 3.16). We found empirically that the temperature change does not exceed 1 K for the following range of velocities: up to $v \approx 4 \cdot 10^{-2}$ m/s for $F_N \approx 10^2$ N, up to $v \approx 2 \cdot 10^{-2}$ m/s for $F_N \approx 10$ N and up to $v \approx 10^{-2}$ m/s for $F_N \approx 100$ N.

The measured coefficients of friction as a function of force are shown in Fig. 3.17.

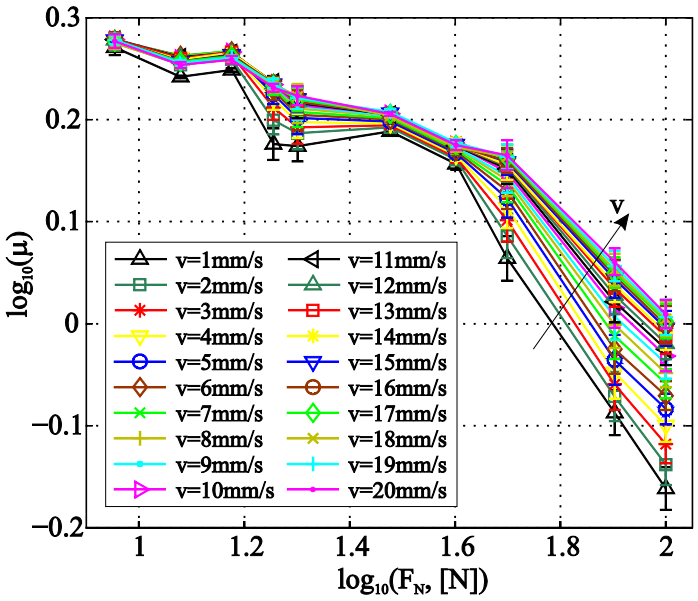

Fig. 3.17 Measured dependencies of $\log_{10}\mu$ on $\log_{10}F_N$ at various velocities at the temperature $25.5\pm0.5\ ^{\circ}C$. (Data from: Voll. L [12])

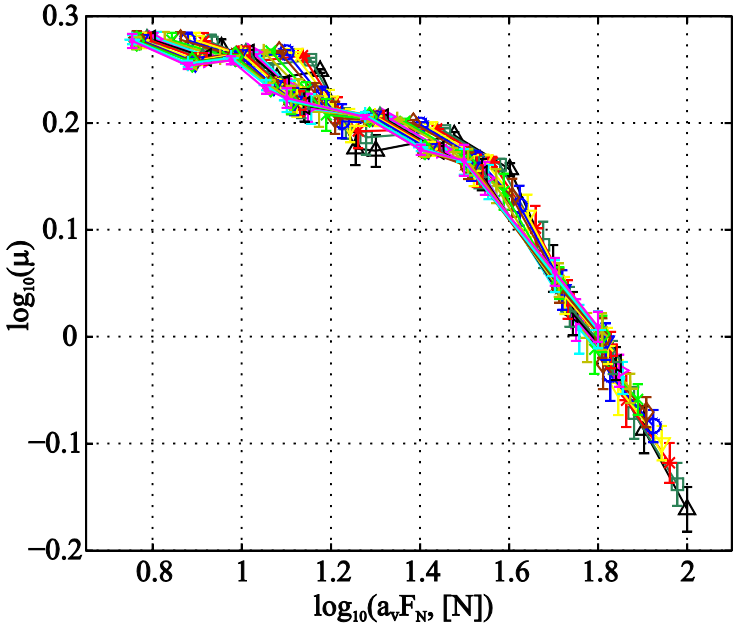

Fig. 3.18 Horizontal shifting of the curves shown in Fig. 3.17 relative to the curve at the reference velocity of 1 mm/s provides a "master curve". It has two distinct linear parts. (Data from: Voll. L [12])

If the shifting procedure formulated in section 3.3.3 is valid, all the curves shown in this figure have to be considered as different parts of the same curve shifted along the $\log F_N$-axis. Fig. 3.17 illustrates that it is indeed possible to shift all the curves to produce one single "master curve". It is interesting to note that the resulting master curve has two

distinct linear regions, meaning a power dependence of the coefficient of friction on the normal force. The crossover between different powers occurs at the force $F_N \approx 40$ N which coincides with the force $F_N^* \approx (2/3)G_0 D^3 / R \approx 40$ N, at which the contact diameter $2a$ becomes equal to the thickness of the rubber layer $D = 5 \cdot 10^{-3}$ m. At this force the stiffness-force dependence changes from the Hertzian $k \propto F^{1/3}$ to $k \propto F^{1/2}$ [10], and we expect a change of the scaling relation.

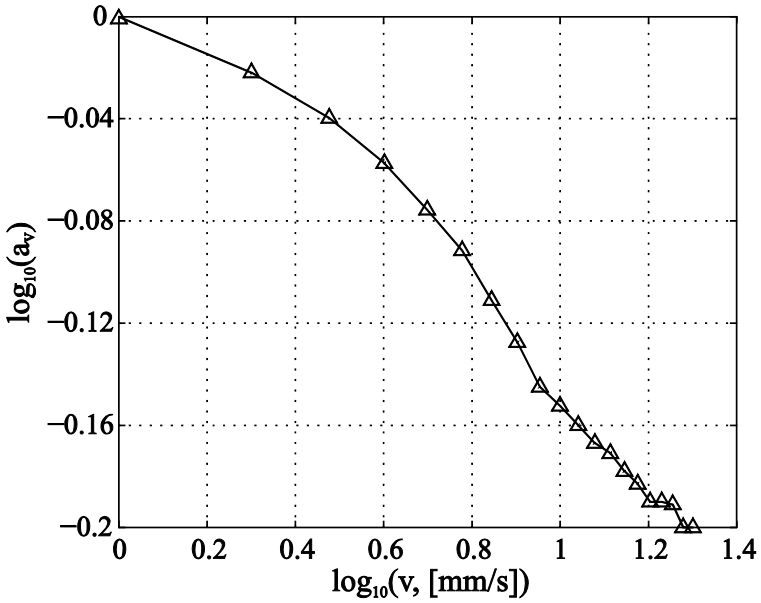

Fig. 3.19 Shifting factors as a function of the sliding velocity.

Fig. 3.19 shows the dependence of the shifting factor on the sliding velocity. Roughly speaking, the shifting factor is a linear function of the logarithm of velocity with the slope -0.15. This result can be interpreted as follows. In the intermediate frequency range, the loss modulus G'' often is a power function of frequency:

$$G''(\omega) = \tilde{G} \cdot \left(\omega / \omega_0\right)^{\beta} \tag{3.45}$$

where ω_0 is a reference frequency and β a power typically in the range of 0.1 to 0.5 (see e.g. [69]). In this case Eq. (3.43) can be rewritten as (here for a sphere with radius R, $n = 2$, $c_n = 1/R$):

$$\frac{\mu}{\nabla z \sqrt{2}} \approx \left\{ 1 + \left[\frac{q_{\max}^{1-\beta}}{2\sqrt{2}\tilde{G}\nabla z} \left(\frac{16 G_0}{3R} \right)^{\frac{1}{3}} \left(\frac{F_N^2}{v^{3\beta}} \right)^{\frac{1}{3}} \right]^{\alpha} \right\}^{-1/\alpha} \tag{3.46}$$

In this case, the shift factor is a linear function of $\log v$ with the slope $-3\beta/2$. Comparing this with the experimental value of -0.15 gives $\beta \approx 0.1$. This is compatible

both with the rheological data for the used rubber compound and with data from literature.

3.4 Summary

In this Chapter we firstly gave a brief introduction of one-dimensional contacting bodies: rough profile of the "rigid surface" and Kelvin body of elastomer, then analyzed the friction behavior of elastomers in detail.

In Section 3.2, we have shown that the law of friction between a linear viscoelastic body and a rigid fractal surface can be formulated in terms of two dimensionless variables (3.19) and (3.20) which are proportional to the sliding velocity and the normal force, correspondingly. Over these variables, the force of friction generally depends on all material, loading, and roughness parameters: sliding velocity, normal force, shear modulus, viscosity, rms roughness, rms slope, and even the size of the system. Generally, the force of friction is not proportional to the normal force, thus, Amonton's law is violated. However, in the plateau region, where the coefficient of friction achieves its maximum, it is proportional to the rms slope of the roughness in the contact region and depends only weakly on the normal force or any other system parameter. We provided physical interpretation of the dimensionless variables and a simple interpolation equation summarizing all numerical and analytical data for a surface with self-affine roughness having Hurst exponents in the rage from 0 to 1. One of the implications of the obtained analytical results is the genaralization of the "master curve procedure" to further variables such as the normal force and the size of the system. We argued that the main physics of the frictional process are dimension-invariant. In particular, the general scaling relations should retain their validity for three-dimensional systems.

In Section 3.3, we analyzed the frictional behavior of elastomers contacting with other shaped profiles under the following simplifying assumptions: (a) the rigid counter body has a power law shape (e.g. parabolic or conical), (b) the macroscopic contact mechanics of the indenter is governed mainly by the low frequency shear modulus, which can be assumed to be approximately constant, (c) the friction is governed by the corrugations with the smallest wavelength in the spectrum of the surface roughness. Under these assumptions, we have shown that the coefficient of friction is a function of a dimensionless argument, which is a multiplicative function of powers of velocity and force. The exact form of this argument depends both on the rheology and the macroscopic form of the indenter. But independently of the exact form, the dependence of the coefficient of friction in the range from very small velocities to the plateau occurs to be a universal function of this argument, suggesting a generalization of the known "master curve procedure": if the dependence of μ on the normal force is presented in double logarithmic coordinates, it will have the same shape for arbitrary velocities, only shifted along the velocity axis. We have proven this procedure with experimental results

obtained on polyurethane rubber. In combination with the widely used shifting procedure for varying temperature [23], it allows to determine generalized laws of friction as functions of velocity, temperature and normal force. The results of the present study generalize and validate the results of the pioneering work by Schallamach [27].

Chapter 4 Kinetics of the Coefficient of Friction of Elastomers

In the previous Chapter, we have studied the friction law of elastomers where the dragging velocity of rigid profile in a certain contact condition keeps always constant and the friction is considered only at steady-state. With the same basic model we will analyze the kinetics of the coefficient of friction of an elastomer due to abrupt changes of sliding velocity in this Chapter.

The work in this chapter appears in paper [61] (Li, Q., Dimaki, A. V., Popov, M., Psakhie, S. G. & Popov, V. L. Kinetics of the coefficient of friction of elastomers. *Sci. Reports* (2014)). My contribution (in accordance with the content of this chapter) is the following: Li Q carried out the numerical simulation. The details of the numerical calculation are described in section 4.2. Popov M and Dimaki AV provided initial program code. Popov VL and Li Q analyzed the simulation results and formulated them in equations including Eq. (4.5) to Eq. (4.12) (section 4.3). Li Q prepared Fig. 4.1 to Fig. 4.7. Popov VL and Li Q discussed the results including Eq. (4.13) to Eq. (4.15) (section 4.4) and contributed in preparing the manuscript of [61]. All authors of [61] reviewed the manuscript [61].

4.1 Introduction

Already Coulomb [14] knew that the coefficient of sliding friction depends on sliding velocity and normal force and that static friction depends approximately logarithmically on time [81]. The explicit dependence of the coefficient of friction on time became a hot topic in the 1970s in the context of earthquake dynamics. Based on the experimental work on rocks by Dieterich [82] [83], Rice and Ruina [84] have formulated a kinetic equation for friction, which became one of the most influential generalized "rate-state models". Similar kinetic behavior of the coefficient of friction was observed on a variety of different materials including metals, paper and polymers [85][89]. Most physical interpretations of rate-state friction are based on the concept by Bowden and Tabor [15] emphasizing the influence of the interaction of rough surfaces; they include direct observations of the contacting surfaces [90] as well as theoretical analysis [91][92]. Other models for the kinetics of the friction coefficient were proposed based on the development of surface topography due to wear (Ostermeyer [93] [94]) or shear melting of thin surface layers [95]. Heslot et. al. [96] provided a very detailed experimental analysis of the dynamics of systems obeying the rate-state law of friction. The kinetics of the coefficient of friction is an essential factor for the stability of systems with friction [97][99], the break-out instabilities [100] as well as for the design of feedback control systems [101][103] and remains a topic of high scientific and technological interest. Most rate-state formulations of frictional laws contain a characteristic length scale, at which a transition from sticking to sliding occurs. The existence of this length is typically

associated with a characteristic size of asperities or with other structural peculiarities at the micro scale [104] [105].

In spite of the intensive research in the field of generalized laws of friction, both the form of the rate-state friction equations and their parameters can still only be determined empirically. In the present chapter, we provide a theoretical analysis of the kinetics of the friction coefficient for elastomers. For these materials, parameters of the kinetic law of the coefficient of friction are connected with material, loading and surface parameters. We simulate the standard type of loading used to experimentally determine the parameters of the rate-state laws: One of the bodies in contact first slides with a constant velocity; at some moment of time, the sliding velocity changes abruptly, and the jump of friction as well as the subsequent relaxation is observed. From these simulations we derive closed-form relations for the jump of friction and the characteristic time of the following relaxation.

The one-dimensional model of elastomers and rigid body is exactly same as described in Chapter 3.

4.2 Theoretical model

The two contacting bodies and their models are exactly same as described in Chapter 3, i.e. viscoelastic foundation with Kelvin body for elastomer and rigid profile with randomly rough roughness.

The model is described in detail in Chapter 3. Here we reproduce for convenience only the basic equations. If the rigid profile is given by $z = z(x - vt)$, and the profile of the elastomer by $u = u(x,t)$, then the normal force in each particular element of the viscoelastic foundation is given by

$$f = -4\Delta x\left(Gu(x) + \eta\dot{u}(x,t)\right). \tag{4.1}$$

For the elements in contact with the rigid surface, this means that

$$f = 4\Delta x\left(G\left(d - z(x)\right) + \eta v z'(x)\right), \tag{4.2}$$

where d is the indentation depth, and $z'(x)$ denotes a derivative with respect to x. For these elements, the condition of remaining in contact, $f > 0$, is checked in each time step. Elements out of contact are relaxed according to the Eq. $f = 0$: $Gu(x) + \eta\dot{u}(x,t) = 0$, and the non-contact condition $u < z$ is checked. The indentation depth d is determined to satisfy the condition of the constant normal force

$$F_N = -4\int_{(\text{real cont})}\left[G\left(d - z(x)\right) + \eta v z'(x)\right]\mathrm{d}x, \tag{4.3}$$

where the integration is only over points in contact. A typical configuration of the contact is shown in Fig. 3.5. The tangential force is calculated by multiplying the local normal force in each single element with the local surface gradient and subsequently summing over all elements in contact:

$$F_x = -4\int_{(\text{real cont})} z'(x)\left[G\left(d - z(x)\right) + \eta v z'(x)\right]\mathrm{d}x\,. \tag{4.4}$$

The coefficient of friction μ was calculated as the ratio of the tangential and normal force.

Due to the independence of the degrees of freedom, the algorithm is not iterative and there are no convergence problems. The length of the system was $L = 0.01$ m and the number of elements $N = L/\Delta x$ was typically 5000. The shear modulus was $G = 10^7$ Pa. Instead of viscosity, the relaxation time $\tau = \eta/G = 10^{-3}$ s was used. The following ranges of parameters were covered in the present study: 11 values of the Hurst exponent ranging from 0 to 1; Normal forces F_N ranging from 10^{-2} to 10^2 N; Δx ranging from 10^{-7} m to 10^{-5} m; roughness ranging from 10^{-6} m to 10^{-4} m; velocities v_1 from 10^{-4} to 10^1 m/s; velocity jumps Δv from $-0.2v_1$ to $0.3v_1$. All values shown below were obtained by averaging over 200 realizations of the rough surface for each set of parameters.

4.3 Numerical results

The following numerical experiments were carried out: The rigid surface was pressed against the elastomer with a normal force F_N and moved tangentially with a constant velocity v_1.At the time moment t_0 the velocity was abruptly changed to a new value v_2 which could be larger or smaller than the initial value. A typical behavior of the coefficient of friction before, during and after the velocity jump is shown in Fig. 4.1.

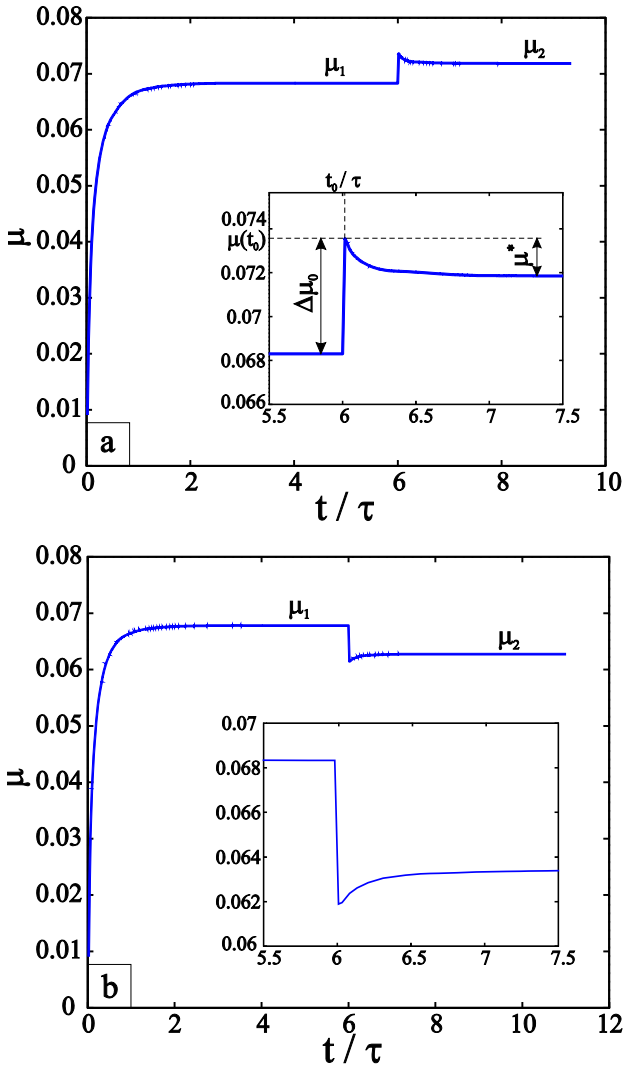

Fig. 4.1 The kinetics of the coefficient of friction after a positive (a) $v_2 = 1.2 \cdot v_1$ and negative (b) $v_2 = 0.8 \cdot v_1$ velocity jumps for the parameters: $F = 0.1$ N, $v_1 = 0.1$ m/s, $L = 0.01$ m, $h = 10^{-5}$ m, $G = 10^7$ Pa, $\tau = 10^{-3}$ s and $H = 0.7$.

The initial value of the coefficient of friction before jump and the final value after relaxation are of course just the values of the dependence of the coefficient of friction on velocity at stationary sliding which have been studied in previous Chapter and are reproduced for one set of material and loading parameters in Fig. 4.2a. With the same parameters, Fig. 4.2b shows the kinetic coefficients of friction changing with time for all the velocities in the whole range in Fig. 4.2a where the sliding velocity is increased by 20% at the moment $t/\tau = 10$. In the present chapter, we studied the complete range of velocities from the region I where the friction coefficient increases approximately linearly with velocity over the transition region II up to the plateau III (Fig. 4.2a).

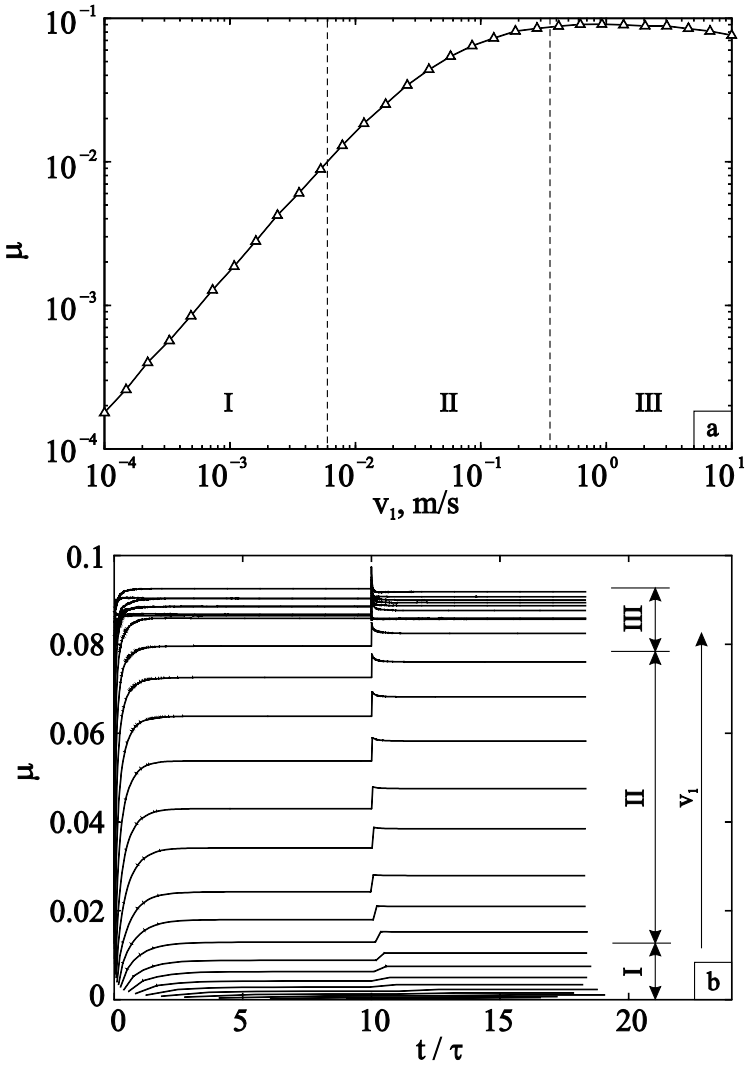

Fig. 4.2 (a) Dependence of the coefficient of friction on the sliding velocity during stationary sliding; (b) kinetic coefficient of friction for the 30 velocities in Fig. 4.2(a) with $\Delta v = 0.2 v_1$. Other parameters: $L = 0.01$ m, $h = 10^{-5}$ m, $G = 10^7$ Pa, $\tau = 10^{-3}$ s, $H = 0.7$, $F_N = 0.1$ N.

The relaxation of the coefficient of friction after the jump can be accurately fitted by an exponential function of the form

$$\mu(\bar{t}) = \mu^* \cdot e^{-b \cdot \bar{t}} + \mu_2, \tag{4.5}$$

where

$$\bar{t} = (t - t_0) / \tau . \tag{4.6}$$

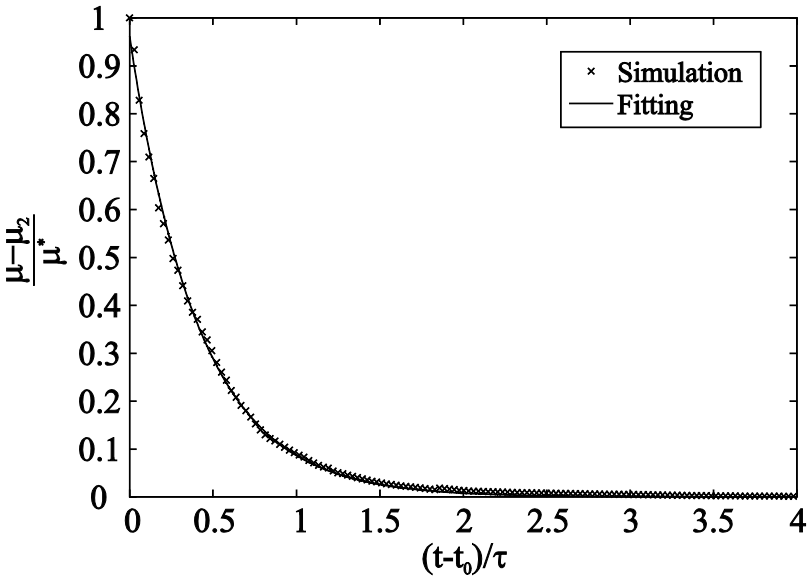

Fig. 4.3 Fitting with an exponential function Eq. (4.5) ($b = 2.4$) for the data set: $L = 0.01$ m, $h = 10^{-5}$ m, $G = 10^7$ Pa, $\tau = 10^{-3}$ s, $H = 0.7$, $F_N = 1.2$ N, $\Delta v = 0.2 v_1$ and $v_1 = 0.05$ m/s.

An example of fitting is shown in Fig. 4.3. .According to Eq.(4.5), the coefficient of friction at the moment $t = t_0$ is equal to $\mu(t_0) = \mu^* + \mu_2 = \mu_1 + \Delta\mu_0$, therefore

$$\mu^* = \mu_1 - \mu_2 + \Delta\mu_0 = -\mu'(v) \cdot \Delta v + \Delta\mu_0 . \tag{4.7}$$

The kinetic behavior is therefore completely determined by the value $\Delta\mu_0$ of the jump of the coefficient of friction and its relaxation time.

4.3.1 Jump of the coefficient of friction

We firstly consider the value $\Delta\mu_0$ at the time of jump $t = t_0$. From the numerical results it is shown that for very small velocity jumps, both the immediate increase of the coefficient of friction, $\Delta\mu_0$, and the difference between the asymptotic values $\mu_2 - \mu_1$, are proportional to the velocity change:

$$\frac{\Delta\mu_0}{\mu_1} = \zeta \frac{\Delta v}{v_1}, \quad \frac{\mu_2 - \mu_1}{\mu_1} = \xi \frac{\Delta v}{v_1} . \tag{4.8}$$

In the limit of small velocities, (region I, corresponding to the linear dependence of the coefficient of friction on velocity), both ζ and ξ are close to "1". It means that μ jumps directly to the value μ_2, so that there is practically no subsequent relaxation. This behavior can be clearly observed in Fig. 4.2b.

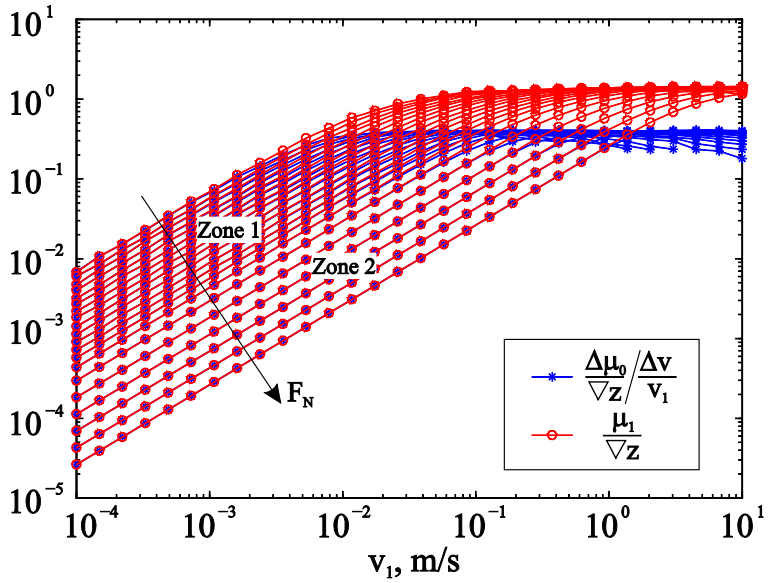

Fig. 4.4 Dependence $\frac{\mu_1}{\nabla z}$ and $\frac{\Delta\mu_0}{\nabla z}\Big/\frac{\Delta v}{v_1}$ on velocity for 20 exponentially increasing normal forces F_N from 10^{-2} to 10^{2} N. Other parameters: $\Delta v = 0.2 v_1$, $L = 0.01$ m, $h = 10^{-5}$ m, $G = 10^{7}$ Pa, $\tau = 10^{-3}$ s and $H = 0.7$.

Fig. 4.4 shows that the velocity dependence of $\Delta\mu_0$ is similar to that of the coefficient of friction μ_1 which is studied in previous Chapter. In particular, $\Delta\mu_0$ first increases linearly with velocity and then approaches a plateau. The results from simulations with different Δv and different Hurst exponents prove that the linear part of this dependency can be universally described by

$$\frac{\Delta\mu_0}{\nabla z} = \frac{\mu_1}{\nabla z}\cdot\frac{\Delta v}{v_1} \tag{4.9}$$

while at the plateau the relation

$$\frac{\Delta\mu_0}{\nabla z} = \frac{\mu_1}{\nabla z}\cdot 0.4 \tag{4.10}$$

is valid. These equations can be combined to the following interpolation equation

$$\Delta\bar{\mu}_0 = \frac{\Delta v}{v_1}\left[\frac{1}{\bar{\mu}_1^{\,2}} + \frac{1}{0.4^2}\right]^{-1/2}. \tag{4.11}$$

where we introduced normalized quantities $\Delta\bar{\mu}_0 = \Delta\mu_0 / \nabla z$ and $\bar{\mu}_1 = \mu_1 / \nabla z$. The quality of this approximation is illustrated in Fig. 4.5 by comparison with numerical results for 11 Hurst exponents.

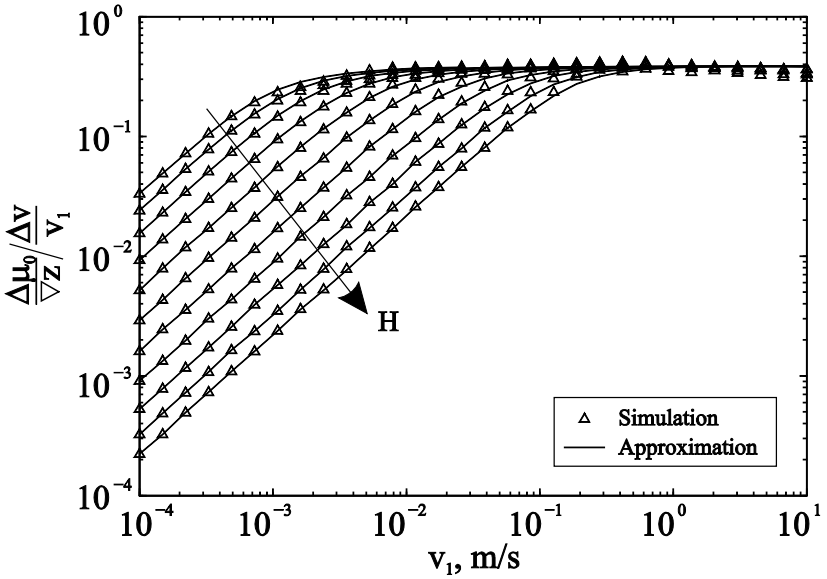

Fig. 4.5 Approximation of Eq. (4.11) with $\alpha = 2$ for 11 Hurst exponents from 0 to 1. Other parameters: $\Delta v = 0.2 v_1$, $L = 0.01$ m, $F_N = 1.2$ N, $h = 10^{-5}$ m, $G = 10^7$ Pa, $\tau = 10^{-3}$ s.

4.3.2 Relaxation of the coefficient of friction

Let us now consider the relaxation behavior after the jump. We found that the simulation results for the coefficient b in Eq. (4.5) can be described accurately by the empirical Eq.

$$b = \beta \cdot \left(v_1 \tau q_{\max} \right)^{\alpha}, \tag{4.12}$$

where α is a coefficient which depends only on the Hurst exponent.

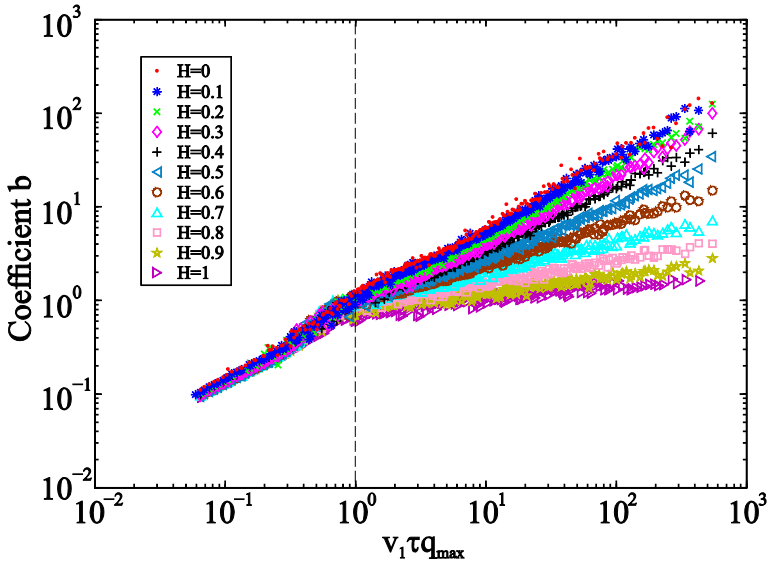

Fig. 4.6 Dependence of the coefficient b on $v_1 \tau q_{\max}$ for different Hurst exponents with the data set: $L = 0.01$ m, $h = 10^{-5}$ m, $G = 10^7$ Pa, 20 normal forces F_N ranging from 10^{-2} to 10^2 N, 20 velocities v_1 ranging from 10^{-4} m/s to 10^{-1} m/s, 20 Δx ranging from 10^{-7} m to 10^{-5} m.

Fig. 4.6 shows the dependence of the coefficient b on the combination $v_1\tau q_{\max}$ for different Hurst exponents. For $v_1\tau q_{\max} < 1$ (left part in Fig. 4.6), the coefficient α is practically constant: $\alpha \approx 1$, while for $v_1\tau q_{\max} > 1$ it can be approximated as $\alpha \approx 1 - H$ (Fig. 4.7).

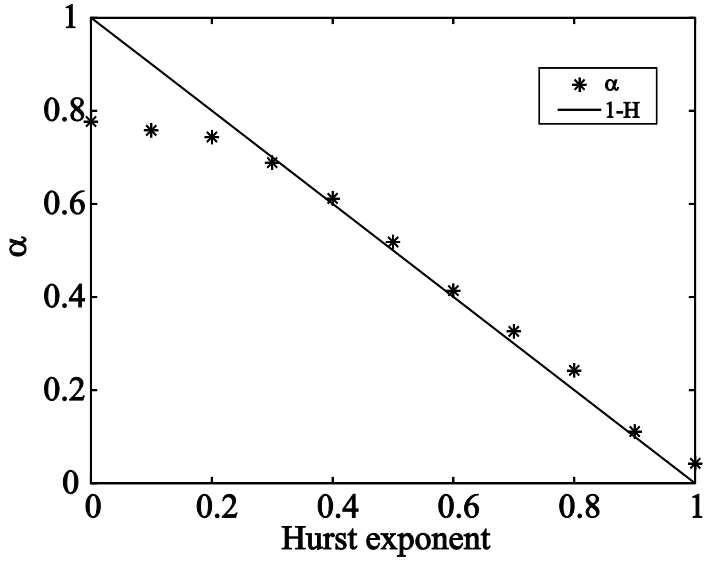

Fig. 4.7 Dependence of the power α in Eq. (4.12) on Hurst exponent for $v_1\tau q_{\max} > 1$.

4.4 Discussions

We investigated the kinetics of the coefficient of friction after a jump of sliding velocity for a model elastomer. We found a simple general structure of the kinetics: the coefficient of friction first experiences a jump, followed by relaxation according to an exponential law to the new stationary value. The jump $\Delta\mu_0$ of the coefficient of friction and the relaxation time are thus the only quantities which describe completely the kinetics of the coefficient of friction. For the model elastomer studied, we found closed form relations for both $\Delta\mu_0$ and the relaxation time as functions of material and loading parameters. The character of the relaxation is governed by the quantity $v\tau q_{\max}$, which can be considered as ratio of two characteristic times of the system: the relaxation time τ of the elastomer and the typical time of contact of micro asperities $1/(vq_{\max})$. For $v_1\tau q_{\max} < 1$, the coefficient b in Eq. (4.5) is approximately equal to $b \approx v_1\tau q_{\max}$, so the relaxation of the coefficient of friction is given by the Eq.

$$\mu(v_1 + \Delta v, t - t_0) = \mu(v_1) + \Delta v \cdot \left\{ \mu'(v_1) + \left[\frac{1}{v_1} \left(\frac{1}{\mu^2(v_1)} + \frac{1}{(0.4\nabla z)^2} \right)^{-1/2} - \mu'(v_1) \right] \cdot e^{-v_1 q_{\max} \cdot (t - t_0)} \right\}. \quad (4.13)$$

Note that in this region relaxation of the coefficient of friction occurs at a characteristic length $D_c = 1/q_{\max}$, which has the same order of magnitude as the size of micro contacts between the bodies, in accordance with the initial concept of Dieterich et. al. [90]. For $v_1 \tau q_{\max} > 1$, the relaxation of the coefficient of friction is described as

$$\mu\left(v_1 + \Delta v, t - t_0\right) = \mu\left(v_1\right) + \Delta v \cdot \left\{ \mu'\left(v_1\right) + \left[\frac{1}{v_1} \left(\frac{1}{\mu^2\left(v_1\right)} + \frac{1}{\left(0.4 \nabla z\right)^2} \right)^{-1/2} - \mu'\left(v_1\right) \right] \cdot e^{-\frac{(t-t_0)}{t_{relax}}} \right\} \tag{4.14}$$

with the characteristic relaxation time

$$t_{relax} = \tau^H \left(v q_{\max}\right)^{H-1}. \tag{4.15}$$

Eq. (4.14) covers the limiting cases of relaxation at a characteristic length $1/q_{\max}$ (in the limit $H = 0$) and of relaxation at a characteristic time τ (in the limit $H = 1$).

Chapter 5 Mixed Boundary Lubrication

In this chapter we come to another important topic in the area of tribology – lubrication. As described in Chapter 1, mixed lubrication is the most difficult problem due to coexistence of both asperity contact and lubricated contact. We firstly give a short review on elastohydrodynamic lubrication (EHL). Based on the results from EHL, a new model of mixed lubrication is proposed in the framework of the MDR. In this model the dynamic lubricated rolling contact between rough surfaces is simulated. In order to account for the break-through of the additional boundary layer on a local micro contact area, an additional criterion is imposed. For comparison, a twin-disc test rig is set up to measure the electrical resistance between two lubricated rolling surfaces under different normal forces, rotation speeds and temperatures. We investigate the probability of boundary layer breakthrough for both experiment and simulation and find good agreement.

Part of the work in this chapter appears in the paper [33] (Li, Q. & Pohrt, R. Mixed and Boundary Lubrication in Rolling Contact: Experiment and Simulation. *FACTA Univ. Ser. Mech. Eng.* 11, 123–131 (2013)). My contribution to [33] (in accordance with the content of this chapter) is the following: both authors proposed the numerical model (section 5.2) and contributed to analysis from EHL contact (section 5.2.1) to breakthrough of boundary layer (section 5.2.2). Li Q carried out the numerical calculation and prepared the figures. The simulation results are illustrated in Fig. 5.5 and Fig. 5.7a. Pohrt R set up experiment (Fig. 5.8) and both authors carried out measurement and collected data (Fig. 5.7b). Both authors discussed the results from numerical calculation and experiment measurement (Fig. 5.9 and Fig. 5.10). Both authors contributed in preparing the manuscript of [33].

5.1 Introduction

Countless examples in mechanical engineering require lubrication between components that are in relative motion. It is known from experience that practically no wear at all occurs when these components operate under conditions, where the surfaces and their roughness features are completely separated by a fluid film. On the other hand, current trends in engineering are at a disadvantage to the creation of a fluid film:

- Downsizing mechanical components demand for higher pressures
- Low-viscosity oil increases efficiency but decreases film thickness
- Start/stop cycles force the system through low-speed relative motion

As a consequence, it is common practice for mechanical components such as gears, bearings and cams to operate in mixed lubrication mode. Typically the surface roughness of contacting bodies is of the same order as the lubricant film thickness, so that the top micro roughness features (asperities) will enter into contact and part of the load and shearing will be carried by these asperity contacts. Under this regime, various wear and

damage types can occur. In experiments the contact condition for a lubricated system can be observed by measurement of the electrical contact resistance R_c (Fig. 5.1) which is expressed as [106]

$$\frac{1}{R_c} = \frac{\sum 2a_i}{\rho} = \frac{L_{\text{cont}}}{\rho}, \tag{5.1}$$

where ρ is the resistivity of contacting materials and a_i is the radius of each single contact spot. L_{cont} is the total resulting contact length and defined as the sum of contact diameters.

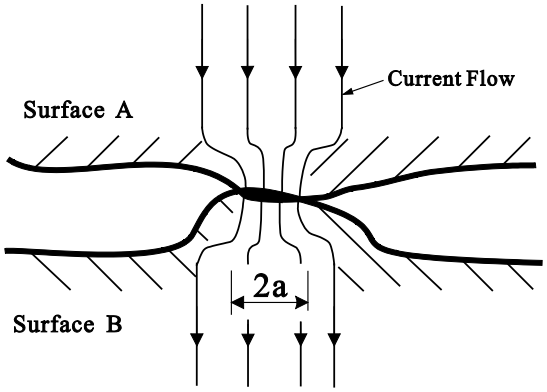

Fig. 5.1 Electrical contact for a single spot between two surfaces.

In the case of full hydrodynamic lubrication, the rough surfaces are completely separated by the lubricant film, so the resistance measured will be very high. In contrast, when the asperity contacts carry a major part of the load, a large number of contact spots are formed, thereby decreasing the electrical resistance dramatically.

5.2 Numerical Model

We deal with the lubricated rolling contact between rough surfaces of cylinders where a boundary layer is present on the two surfaces. Most non-conforming lubricated contacts such as roller bearings, journal bearings, cam and followers or gear teeth can be viewed as such systems. Therefore, we impose a new model for the micromechanical contact between asperities including the physically or chemically absorbed boundary layer (Fig. 5.2) and apply it to the conditions found in lubricated rolling contacts.

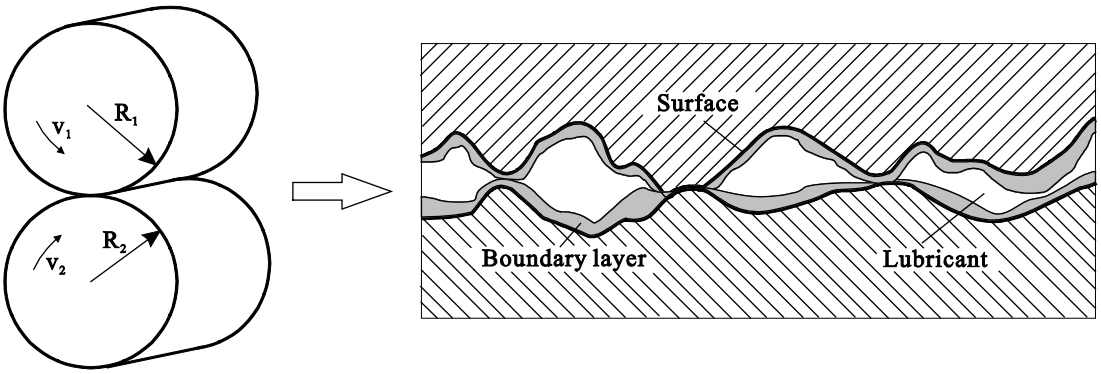

Fig. 5.2 Schematic contact between two cylinders and its view of contact area in micro scale. Surfaces may either have a positive gap width, be separated by a boundary layer or be in intimate contact. The contact conductance only has a considerable value, when there is intimate contact, or the boundary layer has decreased to molecular scale.

The basic idea is following. From the EHL analysis the oil film thickness between an elastic cylinder and a rigid plane is obtained for some load, rotation speed and materials parameters, the latter being dependent on temperature. Based on that, the simulation with the reduction method focuses on the micro contacts within the Hertzian contact zone and assumes the average distance between the rough surfaces to be the same as the oil film thickness resulting from EHL. During the rotation at each moment the number of micro contacts was calculated including the consideration of boundary layer break-through and each local contact length was obtained. The total contact length with rotation angle (or time) is compared with experiment by measuring electrical resistance. Research scheme is in Fig. 5.3.

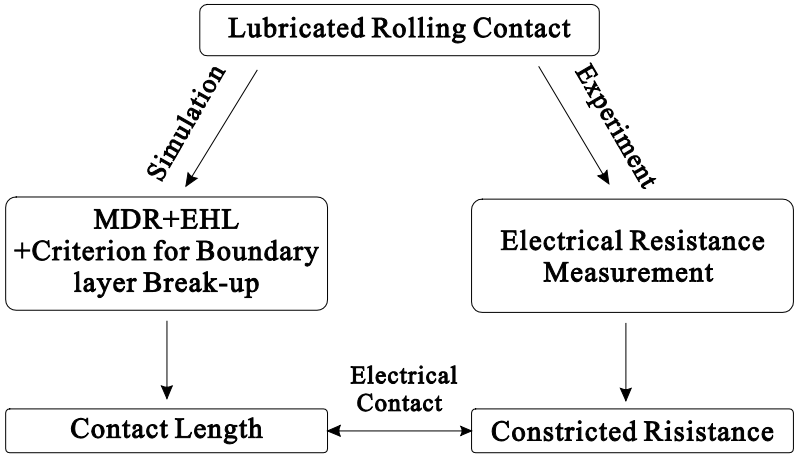

Fig. 5.3 Research scheme.

5.2.1 EHL contact

The contact between two elastic cylinders is known for having an equivalent in the contact between a rigid plane and an elastic cylinder with the equivalent modulus of

elasticity $\frac{1}{E^*}=\frac{1-\upsilon_1^2}{E_1}+\frac{1-\upsilon_2^2}{E_2}$ and radius $\frac{1}{R^*}=\frac{1}{R_1}+\frac{1}{R_2}$, where E_1 and E_2 are moduli of elasticity, υ_1 and υ_2 are Poisson's ratios, R_1 and R_2 are radii of both cylinders. According to Hertzian contact theory, the contact width $2a$ under load F_N is equal to

$$a=\sqrt{\frac{4F_N R^*}{\pi L' E^*}} \tag{5.2}$$

where L' is length of cylinder. For elastohydrodynamic lubricated rolling contact the bodies are separated by an oil film and its thickness over the whole contact area $2a$ is almost uniform, except for the trailing edge where a small decrease in the film thickness occurs (the numerical solution is in Appendix B). A common formula of central film thickness was given by Hamrock from numerical studies [107]

$$h_0=\frac{2.992\alpha^{0.470}\left(\eta_0 v\right)^{0.692}R^{*0.474}}{\left(F_N/L'\right)^{0.166}\left(2E^*\right)^{0.056}} \tag{5.3}$$

where v is mean surface velocity $v=\left(v_1+v_2\right)/2$. The values of η_0 (viscosity at atmosphere pressure) and α (pressure-viscosity coefficient) are properties of the lubricating medium and are usually temperature-dependent. Thus in a case of a known operation scenario, the film thickness excluding roughness can be calculated.

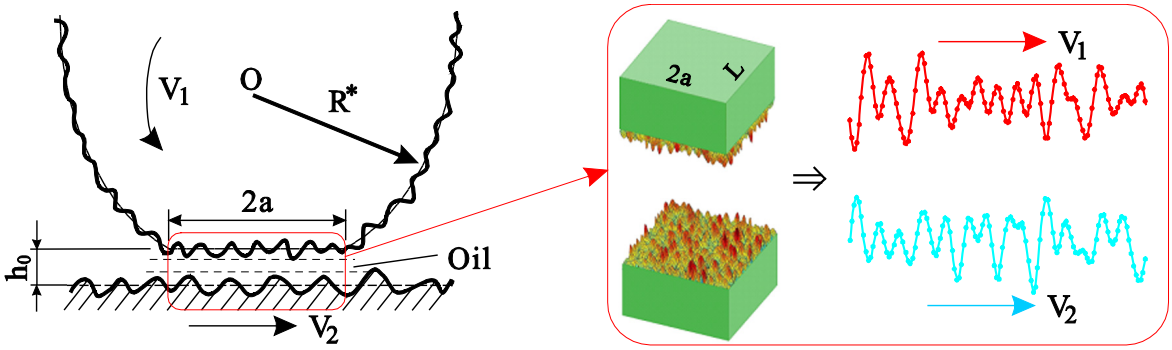

Fig. 5.4 Reduced model for lubricated contact. The original 3D problem consists of two rough opposing bodies with a clearance stemming from the lubricant film. Surfaces constantly move tangentially, so new asperity contacts may form. The problem is transformed with the MDR onto two one-dimensional rough lines.

The lubricated contact area in three dimensional (Fig. 5.4), consists of two moving rectangles with width and length L that are separated by an oil film with average distance h_0 where some asperity contacts may happen.

5.2.2 Reduced model

We treat the contact problem in this zone using the MDR. Coordinates x and z are seen in Fig. 5.5. The average of the rough rigid profile is assumed to be zero and the rough roller is a superposition of a parabolic line and roughness. The roughness has the power spectral density $C_{1D} \propto q^{-2H-1}$, where q is the wave vector and H is the Hurst exponent. In this case, the lines are generated with 10^6 points, corresponding to the perimeter of the roller used in experiments. The spectral density is defined from $q_{\min} = 2\pi/2a_{\max}$ to $q_{\max} = 2\pi/10\Delta x$, where $a_{\max}$ is half the contact width and $H = 0.7$.

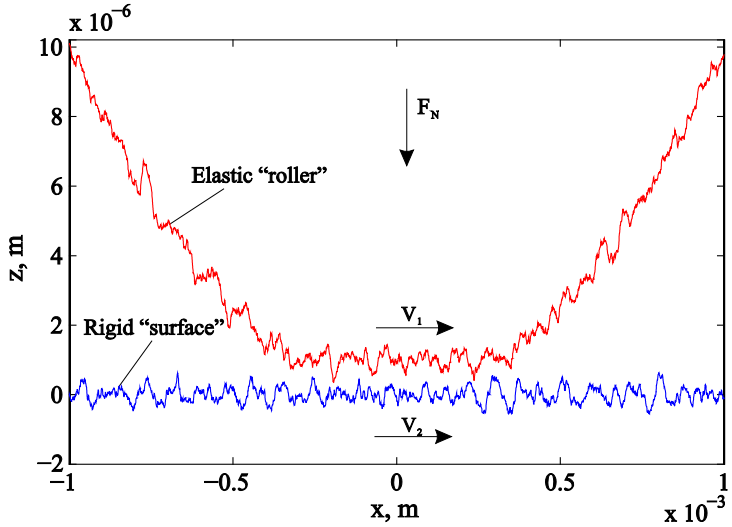

Fig. 5.5 One-dimensional contact between an elastic "roller" and a rigid body. The mean gap width between both is obtained by EHL theory, the resulting micro contacts are analyzed by means of the MDR.

From the results of EHL, the macroscopic shape of the "parabolic line" in the interval $[-a, a]$ is assumed to be flattened out and the average distance between the elastic "roller" and rigid profile is equal to the thickness of oil film h_0. With the applied normal force F and rotation speed v_1 and v_2 (and also temperature), the value of contact width $2a$ and film thickness h_0 can be calculated according to Eq. (5.2) and Eq. (5.3). Therefore, the initial contacting profiles at $t = 0$ are determined. Then, the points on the lines enter and transit through the contact width with different velocities v_1 and v_2. At each time step we check the contact condition. It can be easily observed that some points are in geometrical contact (Fig. 5.6), but in this thesis we consider the boundary layer between two contacting bodies, therefore based on this geometrical contact, the failure of boundary layer must be calculated.

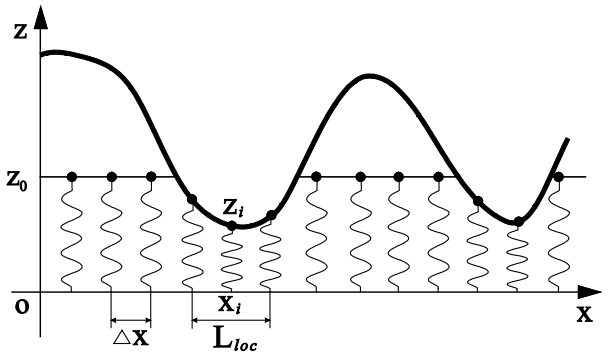

Fig. 5.6 One-dimensional model for the deformation of an elastic body. The 3D surface topography is transformed to give an equivalent line.

For the break-through of the boundary layer, we consider the model of a perfectly plastic material. It is known [10] that if two plates with radius R are pressed together under normal force F and separated by a layer of material with low limiting shear stress τ_0, a film remains with thickness

$$h = \frac{2\pi}{3}\frac{\tau_0 R^3}{F}. \tag{5.4}$$

According to the rules of MDR [108], the elastic body is modeled as a series of parallel springs with the normal stiffness $\Delta c = E^* \Delta x$, where Δx is the discrete step (Fig. 5.6). The force on each spring is defined as

$$f(x_i) = E^* \cdot \Delta x \cdot \Delta z(x_i). \tag{5.5}$$

Here Δz is the displacement of indentation. In the reduced model Eq. (5.4) is written as

$$h_l = \frac{\pi\tau_0}{12}\frac{D_l^3}{F_l}. \tag{5.6}$$

Here D_l is the local contact length and equal to Δx times the number of contacting points and F_l is the normal force on this local area and equal to $F_l = E^* \Delta x \sum \Delta z_i$ from Eq. (5.5). For each "geometrical contact" if the value h_l calculated according to Eq. (5.6) is smaller than a critical thickness of a boundary layer h_c, it is defined that the layer is broken up and asperities are in intimate contact. The thickness of boundary layer due to adsorption and chemical reactions is about 1…10 nm [109]. In the simulation we considered $h_c = 5$ nm and $\tau_0 = 10^6$ Pa.

In a single operation case, the change of total contact length on time is recorded as Fig. 5.7(a). It is seen that at some moments there is no asperity in contact at all. Based on it a general contact condition in this operation case can be obtained from it, which is named the probability of boundary layer breakthrough in the thesis and calculated as time

percentage when real contact occurs. In a well lubricated condition, the probability is close to zero.

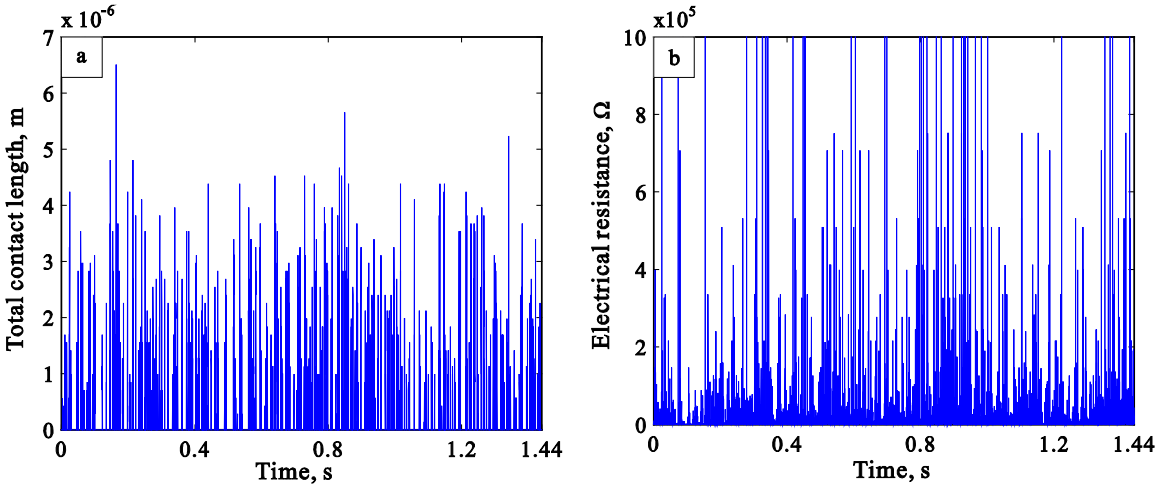

Fig. 5.7 (a) Contact length over time, data extracted from MDR simulation; (b) electrical resistance over time from experiment data. Parameters: 800 N, 100 r/min and 40 °C.

5.3 Measurement

We used a twin-disc test rig (Fig. 5.8) to validate the results obtained from simulation. Two identical cylinders (radius $R = 0.05$ m, width $L' = 0.01$ m, roughness 0.2 μm) are pressed together and rotated at identical speeds, such that pure rolling occurs. Synthetic lubricant is constantly fed into the contact zone. We used Mobilgear SHC XMP 320, because it widely used in highly loaded wind turbine gear boxes. Its properties can be seen in Appendix A. The whole test setup can be heated to give stationary temperature for the rollers and the injected oil.

We measured the electrical resistance between the two rollers for a range of operating parameters: The normal force was varied from 100 to 1600 N, rotation speeds from 86 to 200 r/min and temperatures from 40 to 80 °C.

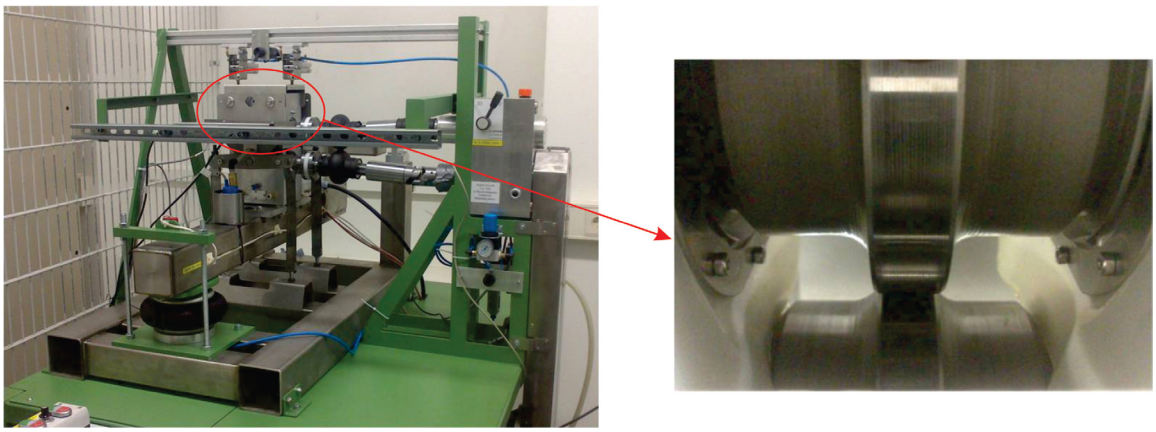

Fig. 5.8 Experimental setup. The left hand side shows the overall test rig. Inside the aluminum block, there are two rollers, driven by external drive shafts. The lower block can be lifted pneumatically to exert a normal force. The right hand side shows a picture of the two rollers in contact without lubricant.

Fig. 5.7(b) shows a typical sample of the time-dependent resistance measurement. It can be seen that the contact condition rapidly changes from states of good conductivity to very high resistance.

In order to compare results quantitatively, we used the classical approach of contact probability [110]. We calculated the percentage of time, for which the electrical resistance was measured to be below 100 Ω. Whenever this is the case, we consider the surfaces to be in contact and the electrical current can flow through the contact spots, otherwise they are separated by a lubricant film. We compare this probability of contact to the simulated probability of boundary layer breakthrough from the 1D model.

5.4 Results

There are totally 125 operation cases in both simulation and measurement. Fig. 5.9 (a) shows the simulated breakthrough probability as a function of the temperature. In Fig. 5.9 (b) the experimental contact time probability for the same scenarios are shown. For reason of clarity, not all cases are included. It can be seen that the contact probability increases with temperature and load but decreases with rotation speed in both investigations. Fig. 5.10 gives a direct comparison for the probability of boundary layer breakthrough between simulation and measurement. Good agreement can be found qualitavely and quantitatively in most cases.

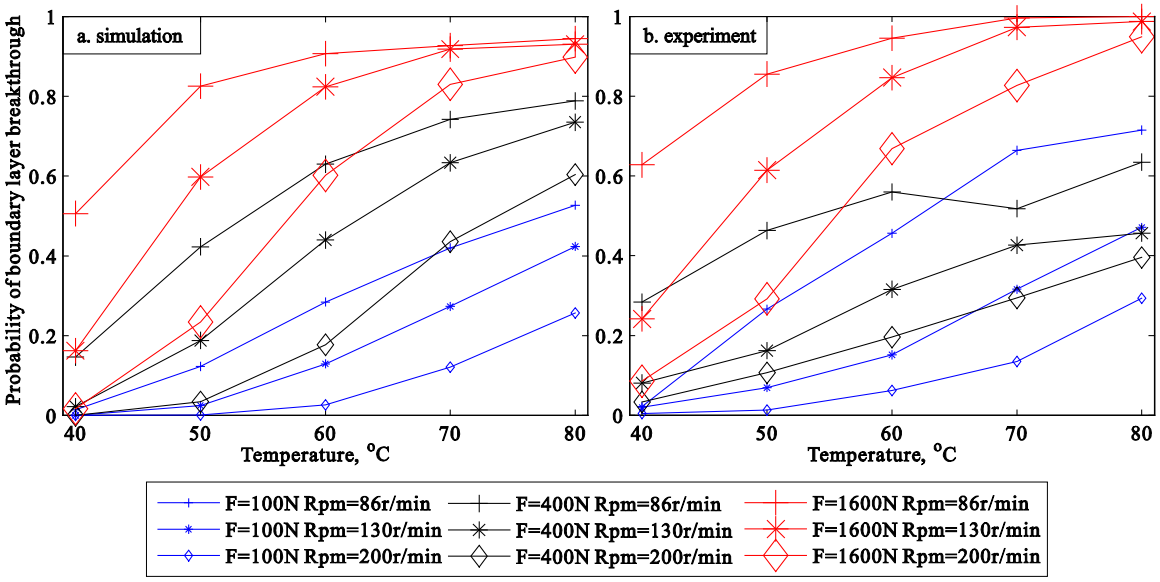

Fig. 5.9 Comparison of boundary layer breakthrough between (a) simulation and (b) experiment.

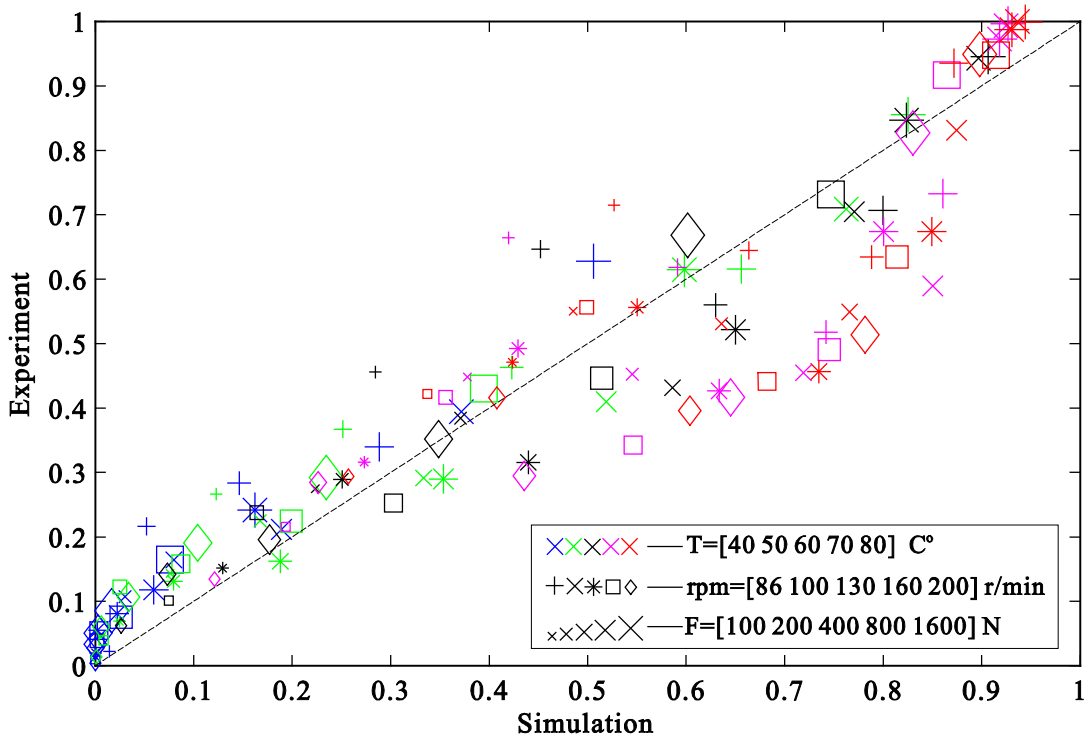

Fig. 5.10 Comparison of boundary layer breakthrough with all data.

5.5 Summary

The MDR was used to simulate the process of lubricated rolling contact between rough surfaces. A novel criterion for the breakthrough of the chemical or physical boundary layer was introduced, based on the assumption of perfectly plastic material behavior. Using this criterion, the breakthrough probability under different working conditions was

predicted and compared to experimental findings. The results obtained show good agreement.

Chapter 6 Fretting Wear

This chapter presents the study of another tribological problem, fretting wear in the framework of the MDR. We deal with rotationally symmetric profiles. Due to oscillations with small amplitude, sliding occurs at the boundary of the contact area while the inner parts of the contact area may still stick. In a recent paper, Dimaki et. al. [1] proposed a numerically exact simulation procedure based on the method of dimensionality reduction (MDR). This drastically reduced the simulation time compared with conventional finite element simulations. The proposed simulation procedure requires carrying out the direct and the inverse MDR transformations in each time step. This is the main time consuming operation in the proposed method. However, solutions obtained with this method showed a remarkable simplicity of the development of wear profiles in the MDR-space.

Now we utilize these results to formulate an approximate model, in which the wear is simulated directly in the one-dimensional space without using integral transformations. This speeds up the simulations of wear by further several orders of magnitude.

The work in this chapter appears in the paper [62] (Li, Q., Filippov, A. E., Dimaki, A. V., Chai, Y. S. & Popov, V. L. Simplified simulation of fretting wear using the method of dimensionality reduction. *Phys. Mesomech.* 17 (2014)). My contribution to [62] (in accordance with the content of this chapter) is the following: Popov VL, Filippov AE and Li Q proposed the simulation procedure in section 6.4 including Eq. (6.11) to Eq. (6.15). Dimaki AV and Li Q designed the initial program code. Li Q carried out the numerical calculation and prepared figures including Fig. 6.1 to Fig. 6.3. Popov VL and Li Q contributed in preparing the manuscript [62]. All authors of [62] reviewed the manuscript [62].

6.1 Introduction

Fretting wear occurs in contacts subjected to oscillations with small amplitude. It is one of the causes for malfunctioning of engineering components, for example, coupled flanges, gears or bearings on a shaft. In theoretical modeling of wear, very often an equation is used which states that the wear volume ΔV is proportional to the normal force F_N, the relative tangential displacement u_x of the contacting bodies and inversely proportional to the hardness σ_0:

$$\Delta V = k\frac{F_N u_x}{\sigma_0}. \tag{6.1}$$

This wear equation was suggested already in 1860 by Reye [43], and was later derived and experimentally justified for abrasive [45] and adhesive wear [46] (derivations see

also in [10]). To describe the detailed changes of form due to wear, the wear law (6.1) is often formulated as local relation

$$\Delta h(x,y) = k\frac{p(x,y)u_x(x,y)}{\sigma_0}, \tag{6.2}$$

where Δh is the linear wear, $p(x,y)$ the local pressure and $u_x(x,y)$ the local relative displacement.

Application of the local rule (6.2) requires solving the contact problem for any current configuration. The main part of the literature on theoretical modeling of fretting wear is devoted to numerical solution of the contact problem using finite element or boundary element programs (see e.g. [49]) and implementation of the Reye-Archard-Khrushchov law in them. In the case of rotationally symmetric profiles, the simulation can be substantially speeded up by solving the contact problem with the MDR [108] as it was done in [1]. In the paper [1], the iterative procedure for the simulation of wear based on the exact MDR-based solution of the three-dimensional contact has been presented. In this procedure, the contact problem is solved for the one-dimensional equivalent system, which is then transformed back to three-dimensions to calculate wear. This requires applying the direct and inverse MDR-transformation in each step of simulation. The resulting procedure is orders of magnitude faster than the corresponding boundary-element programs, but still too slow to be used as an interface in larger dynamical programs. In the present study we suggest an even simpler approximate method in which the solution of the contact problem and the calculation of wear are both carried out in the one-dimensional space.

We first briefly recapitulate the main steps of the method of dimensionality reduction, then analyze the numerically exact solutions obtained in [1] and suggest an empirical procedure for imitating them directly in the one-dimensional MDR-space. Finally, the resulting wear profiles obtained by the numerically exact method of [1] and the simplified method proposed are compared.

6.2 MDR for rotationally symmetric profile

The main steps of the MDR are described in Chapter 1. Given a rotationally symmetric three-dimensional profile $z = f(r)$, the equivalent one-dimensional profile $g(x)$ can be determined by Eq. (2.4). The inverse transformation is given by Eq. (2.5).

The profile $g(x)$ is pressed to a given indentation depth d into an elastic foundation consisting of independent springs with spacing Δx whose normal and tangential stiffness is given by

$$k_z = E^*\Delta x, \quad k_x = G^*\Delta x, \tag{6.3}$$

We assume that the contacting materials satisfy the condition of "elastic similarity" $(1-2\nu_1)/G_1 = (1-2\nu_2)/G_2$ which guarantees the decoupling of the normal and tangential contact problems [2]. The resulting vertical displacements of springs are given by $u_z(x) = d - g(x)$. The contact radius a is given by the condition $u_z(a) = 0$ or

$$g(a) = d\,. \tag{6.4}$$

If the normal displacement of a single spring is equal to $u_z(x)$ and tangential displacement to $u_x(x)$, then the normal and tangential spring forces are equal to

$$\Delta F_z = E^* u_z(x)\Delta x \quad \text{and} \quad \Delta F_x = G^* u_x(x)\Delta x \tag{6.5}$$

correspondingly. The total normal load F_N can be calculated as

$$F_N = \int_{-a}^{a} E^* u_z(x)dx = 2\int_0^a E^*[d - g(x)]dx\,. \tag{6.6}$$

If the profile is moved tangentially by $u_x^{(0)}$, the springs will be stressed both in the normal and tangential direction, and the radius c of the stick region will be given by the condition that the tangential force $\Delta F_x = k_x u_x^{(0)}$ is equal to the coefficient of friction μ multiplied with the normal force: $\Delta F_z(c) = k_z u_z(c)$ which results in the relation

$$G^* u_x^{(0)} = \mu E^* \left(d - g(c)\right). \tag{6.7}$$

As shown in [63], this result reproduces correctly the relations in the corresponding three-dimensional contact.

6.3 Limiting shape of wear profile and development of intermediate shapes

If profile is subjected to oscillations with a small amplitude, then the inner part of the contact area with the radius c given by Eq. (6.7) will sticking while the outer regions will slip [76][77][111]. In these outer regions of the contact area, wear will occur. If oscillations continue very long time, the wear profile will be tending towards a limiting shape [112]. This shape was calculated in the recent paper [60]. In particular, it was shown that the limiting form of the one-dimensional MDR-image has the form

$$g_\infty(x) = \begin{cases} g_0(x), & \text{for } 0 < x < c \\ d, & \text{for } c < x < a \end{cases} \tag{6.8}$$

and the correspondent shape of the three-dimensional profile the form

$$f_\infty(r)=\begin{cases} f_0(r), & \text{for } 0<r<c \\ \dfrac{2}{\pi}\displaystyle\int_0^c \frac{g_0(x)}{\sqrt{r^2-x^2}}\,\mathrm{d}x+\frac{2}{\pi}d\int_c^r \frac{1}{\sqrt{r^2-x^2}}\,\mathrm{d}x, & \text{for } c<r<a \end{cases}. \tag{6.9}$$

Here the subscript ∞ and 0 indicate the limiting and initial form of profile.
The contact radius in the limiting state, $a(c)$, is determined by the condition

$$\frac{2}{\pi}\int_0^c \frac{g_0(x)}{\sqrt{r^2-x^2}}\,\mathrm{d}x+\frac{2}{\pi}d\int_c^a \frac{1}{\sqrt{r^2-x^2}}\,\mathrm{d}x=f_0(a)\,. \tag{6.10}$$

Development of the profiles between the initial and the limiting states calculated using the method proposed in [1], is illustrated with one example in Fig. 6.1.

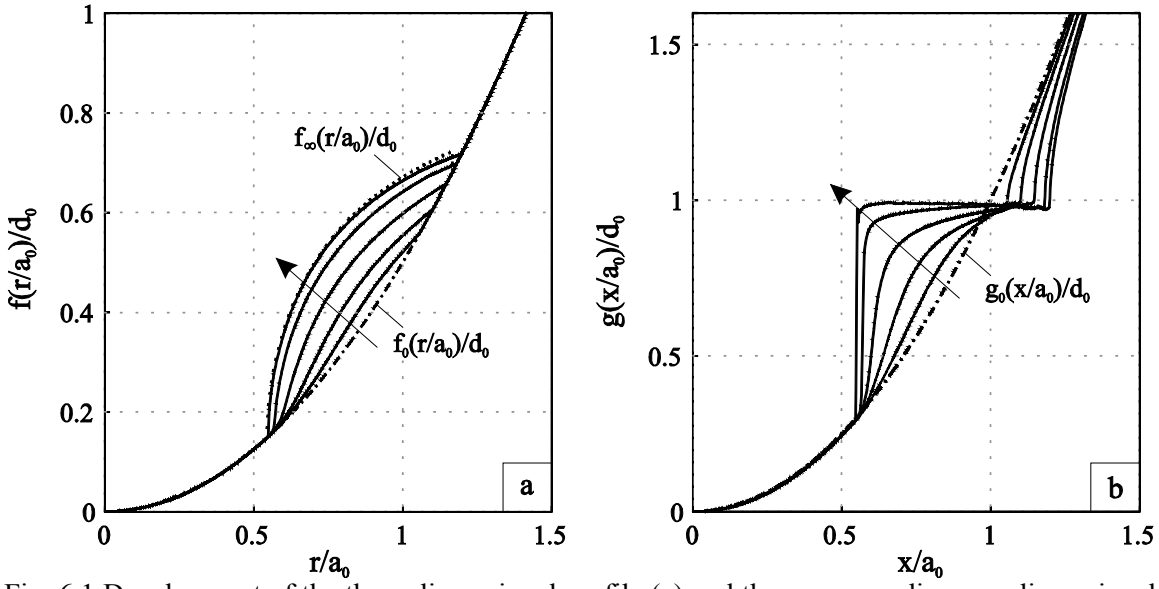

Fig. 6.1 Development of the three-dimensional profile (a) and the corresponding one-dimensional MDR-image (b) due to fretting wear under conditions of constant approach of bodies (that is the indenter is pressed into the elastic half space by the indentation depth d_0 and then oscillates horizontally at this constant height). The amplitude of oscillations was chosen such that $c=0.55a_0$ -The dimensionless number of cycles (as defined by Eq.(6.15)) was $\tilde{N}=4$, 10, 20, 36 and 70 as indicated by arrow.

6.4 Approximate rule for the worn shape

The development of the shape of one-dimensional images as shown in Fig. 6.1b looks simpler than that of true three-dimensional profile. It is easy to "mimic" this development if we note that the main tendency of the profile in Fig. 6.1b is just tending to the constant value of "d" everywhere in the interval $c<x<a$. We can try to simulate this development by the equation

$$\frac{\mathrm{d}g(x)}{\mathrm{d}\delta u_x} = -\frac{\xi k}{a\sigma_0} E^*(g(x)-d), \quad \text{for } c < x < a(c), \tag{6.11}$$

where $\delta u_x(x)$ is the relative displacement of the bodies in contact, $a(c)$ is solution of Eq. (6.10) and ξ is a dimensionless fitting parameter of the order of unity. As $E^*(g(x)-d)$ is the linear force density, and $E^*(g(x)-d)/a$ has the order of magnitude of pressure, this Eq. can be interpreted as a one-dimensional modification of the wear law (6.2). However, we would like to stress, that this equation should not be over interpreted as a real "wear equation", as we have to do with the formal one-dimensional MDR-image and not with the actual three-dimensional profile. For example, according to (6.11), the "wear rate" outside the contact radius (but inside the radius $\tilde{a}$) is non-zero, and even negative!

The procedure for the determination of the relative displacement $\delta u_x(x)$ in Eq. (6.11) is described in the following. Assume that the upper body oscillates periodically with a frequency ω and an amplitude $U^{(0)}$:

$$u_x^{(0)} = U^{(0)} \cos(\omega t). \tag{6.12}$$

As long as the tangential elastic force $\Delta F_x = k_x u_x(x)$ of a spring is smaller than the local maximum friction force $\mu \Delta F_z(x)$, the indenter sticks to the substrate; therefore, the spring displacement coincides with the displacement of the oscillating indenter. After achieving the maximum value of $\mu \Delta F_z(x)$, the tangential force does not increase further, so that the condition $\Delta k_x u_x(x) = \mu \Delta F_z(x)$ is fulfilled, and the bodies slide against each other. These conditions can be written in the form:

$$\begin{cases} \Delta u_x(x) = \Delta u_x^{(0)}, & \text{if } \left|f_x\right| = \left|k_x \Delta u_x(x)\right| < \mu f_z(x) \\ u_x(x) = \pm \dfrac{\mu f_z(x)}{\Delta k_x}, & \text{when sliding} \end{cases}. \tag{6.13}$$

This equation determines unambiguously the tangential displacement $u_x(x)$ of any spring and thus the incremental change $\Delta u_x(x)$ of this displacement at any time. The difference $\delta u_x(x) = \Delta u_x^{(0)} - \Delta u_x(x)$ is then the relative displacement of the indenter and substrate which has to be used in the one-dimensional "wear equation" Eq. (6.11). Outside the contact, $\delta u_x(x) \equiv \Delta u_x^{(0)}$.

For presentation of results, we will use the following dimensionless variables. Let us denote the indentation depth of the initial profile with d_0 and the corresponding initial contact radius with a_0. All vertical coordinates will be normalized by d_0 and the horizontal coordinates by a_0. Thus, we will use the following dimensionless variables:

$$\begin{aligned} &\overline{f} = f / d_0, \quad \overline{d} = d / d_0 \\ &\overline{r} = r / a_0, \quad \overline{x} = x / a_0 \quad . \\ &\overline{c} = c / a_0 \end{aligned} \tag{6.14}$$

The dimensionless number of cycles is defined as

$$\overline{N} = \frac{N}{N_0} \quad \text{with } N_0 = \frac{a_0 \sigma_0}{4U^{(0)} k E^*}. \tag{6.15}$$

For illustration of the procedure described by Eq. (6.11), (6.13) let us consider the cases of a parabolic and a conical indenter.

6.4.1 Case of parabolic indenter

For the case of parabolic indenter, the initial three dimensional profile is $f_0(r) = r^2 / (2R)$, where R is the curvature radius. We consider the situation when this profile is indented in an elastic half-space by the indentation depth d_0 and then oscillates at this constant height. The MDR-transformed one-dimensional profile, according to (2.4), is given by $g_0(x) = x^2 / R$. The initial contact radius is given by the condition $g(a_0) = d_0$. During the oscillation the stick region is determined by Eq. (6.7) and the contact radius is calculated as [60]

$$\overline{a}(\overline{c}) \approx \sqrt{\left(\frac{\overline{c}}{2}\right)^2 + 2} - \frac{\overline{c}}{2}. \tag{6.16}$$

Now the change of the one-dimensional profile due to wear is calculated according to Eq. (6.11) for different number of cycles and the corresponding three-dimensional profiles are calculated by the inverse MDR-transformation (2.5) . The resulted profiles are shown in Fig. 6.2 (b) and (a) by solid lines. In the same figure, the results produced by the numerically exact procedure described in [1] are shown for comparison. The best fitting with exact results is achieved for $\xi = 0.8$. One can see, that the approximate procedure reproduces very accurately results for the three-dimensional profile for any number of wear cycles – in any case with a better precision as the typical accuracy of wear experiments and of the used Reye-Archard-Khrushchov wear law.

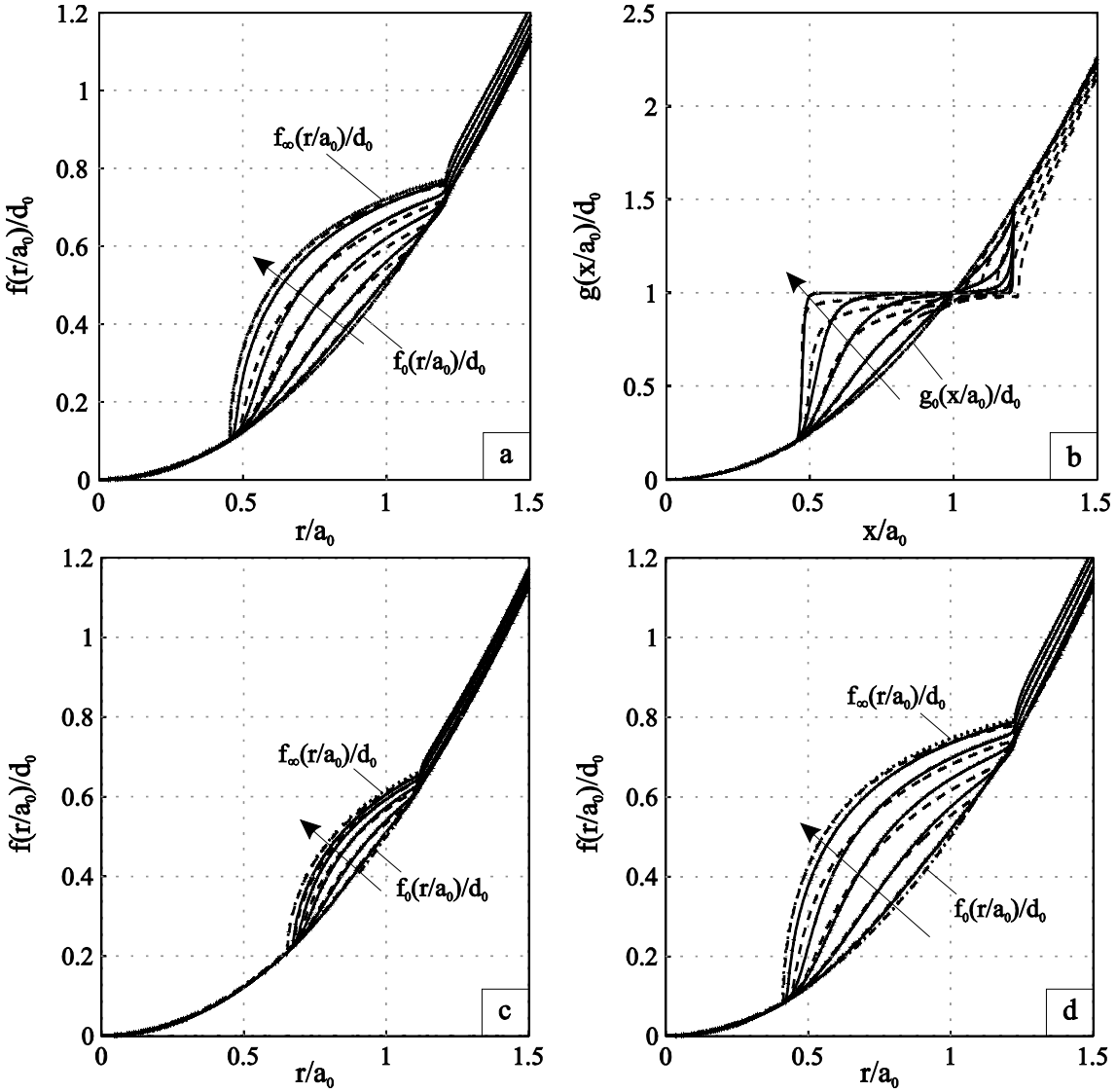

Fig. 6.2 Comparison for parabolic indenter: (a) three-dimensional profile obtained with Eq. (6.11) and subsequent inverse transformation, Eq. (2.5) (solid lines) and (b) one-dimensional profile $g(x)$ calculated according to Eq. (6.11) (solid lines) for different number of oscillation cycles with $\xi = 0.8$. The amplitude of tangential oscillation was chosen so that $c = 0.455a_0$. (c) Three-dimensional profile obtained with Eq. (6.11) with smaller amplitude of tangential oscillation $U'^{(0)} = 0.8U^{(0)}$ ($c = 0.652a_0$) and (d) larger amplitude $U'^{(0)} = 1.2U^{(0)}$ ($c = 0.41a_0$), where $U^{(0)}$ is the amplitude for the case in Fig. 6.2(a). Dashed lines are three- and one-dimensional profiles calculated with the numerically exact procedure described in [1]. The number of oscillation cycles $\bar{N} = 2$, 8, 18, 32, 72 as indicated by arrow, and the last line ($\bar{N} = 72$) in Fig. 6.2(a) (c) (d) almost coincides with the limiting profile from analytical solution (dot line) [60].

6.4.2 Case of conical indenter

For the case of conical indenter, the initial three-dimensional profile is $f_0(r) = r\tan\theta$. The corresponding MDR-transformed one-dimensional profile is $g_0(x) = \frac{\pi}{2}|x|\tan\theta$. The

initial contact radius is given by the condition $g(a_0) = d_0$. During the oscillation the stick region is determined by Eq. (6.7) and the outer wear radius $\overline{a}\left(\overline{c}\right)$ is calculated by solving equation [60]

$$\frac{\pi}{2} - \arcsin\left(\frac{\overline{c}}{\overline{a}}\right) = \sqrt{\overline{a}^2 - \overline{c}^2}\ . \tag{6.17}$$

The one- and three-dimensional profiles obtained by solving Eq. (6.11) are shown in Fig. 6.3a and Fig. 6.3b by solid lines. In the same figure, the results of numerically exact procedure of paper [1] are also shown for comparison (dash lines). As for the parabolic profile, the three-dimensional shapes obtained by the present approximate procedure reproduce with good accuracy the results obtained by the numerically exact procedure of paper [1]. However, the calculating time is reduced by the factor of 600.

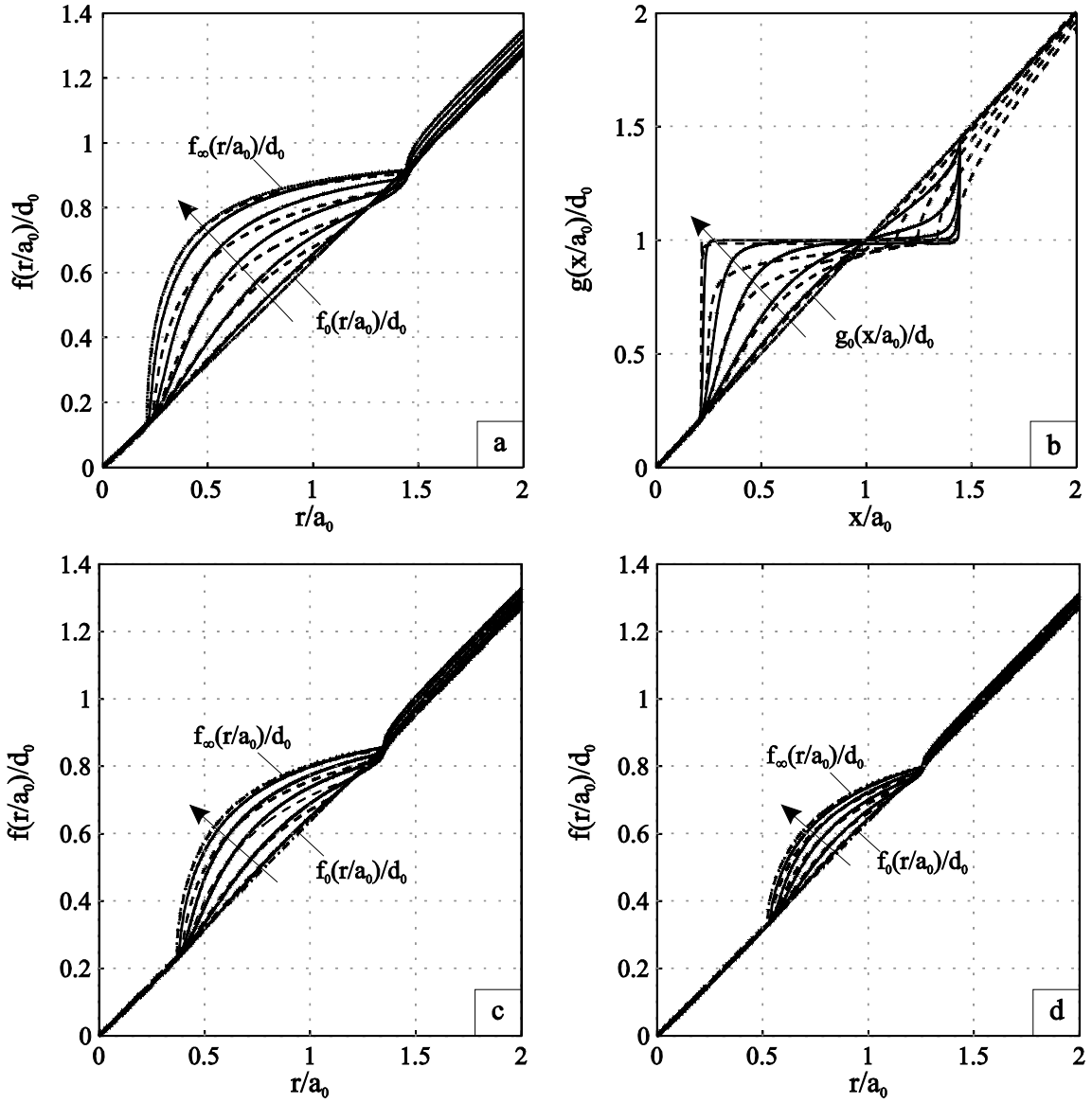

Fig. 6.3 Comparison for conical indenter: (a) three-dimensional profile obtained from $g(x)$ by the inverse transformation, Eq. (2.5) (solid lines) and (b) one-dimensional profile $g(x)$ calculated according to Eq. (6.11) (solid lines) for different number of oscillation cycles with $\xi = 0.8$. The amplitude of tangential oscillation was chosen so that $c = 0.21a_0$. (c) Three-dimensional profile obtained with Eq. (6.11) with the amplitude of tangential oscillation $U'^{(0)} = 0.8U^{(0)}$ ($c = 0.368a_0$) and (d) $U'^{(0)} = 0.6U^{(0)}$ ($c = 0.522a_0$), where $U^{(0)}$ is the amplitude for the case in Fig. 6.3 (a). Dashed lines are three- and one-dimensional profiles according to [1]. The number of oscillation cycles is $\bar{N} = 2$, 8, 18, 32, 72 as indicated by arrow, and the last line ($\bar{N} = 72$) in Fig. 6.3(a) (c) (d) almost coincides with the limiting profile from analytical solution (dot line) [60].

6.5 Summary

In this Chapter, we suggested a simplified numerical procedure for simulation of wear of rotationally symmetric profiles, which is approximately 600 times faster than the fast

MDR-based, numerically exact procedure described in [1]. Taking into account the low precision of the laws of wear, we conclude that this simplified procedure will by more than adequate for any practical simulation. Because of extreme fastness of the procedure, it can be used as a “contact and wear interface” in larger dynamic simulations.

Chapter 7 Conclusions and Outlook

7.1 Conclusions

In spite of being a relative new computational tool, method of dimensionality reduction has been developed fast and was validated for different contact problems in various analytical and numerical ways. Because of the simplicity and sharply reduced computing time, this method has been primly extended to various fields of contact mechanics and tribology. On the basis of this method, the studies of three hot topics in tribology have been presented in the thesis after a short review on fundamentals of the MDR.

We first studied the friction of elastomer in contact with a rigid rough "surface". To achieve a general law, the planar rough profile was initially considered. We have found a general law of friction giving the coefficient of friction as function of all material, loading, and roughness parameters: sliding velocity, normal load, shear modulus, viscosity, rms roughness, rms gradient and system size and form. The coefficient of friction could be formulated in a closed analytical form.

Apart from the analytical solution, a master curve procedure for the dependence on the normal force was suggested and also confirmed by the measurements in the tribological laboratory of the Department of System Dynamics and the Physics of Friction.

Further, the kinetics of the coefficient of friction of elastoemrs has been studied. The typical behavior which appears also frequently in experiments of other materials was observed: due to abrupt changes of sliding velocity, the coefficient of friction jumps at the moment of velocity changing and then relaxes to a new stationary value. Finally the dependence of jump of the friction and the relaxation time are formulated from the numerical results.

Mixed lubrication is more complicated because of both presence of both dry asperity contacts and lubricated contact in the other contact areas. We built a reduced simple model of mixed boundary lubrication which combines results from EHL and elastic rough contact of MDR. The experimental results showed good agreement with numerical solution.

At last we presented the study on fretting wear of a rotationally symmetric profile. On the basis of the results from Dimaki et. al [1] who give exact numerical procedures allowing fast simulation using the MDR, we put forward an even much faster approximate model.

7.2 Future work

The contribution to study and application of MDR in contact mechanics is growing, for example recently published research on partial-slip friction of rough surface, shakedown limits for elastic rolling contact [114] etc. There are still lots of possibilities in the frame

of the MDR, but we address here only some that are directly related to the topics in this thesis.

In the thesis, the elastomer was modeled with Kelvin body which has only one single relaxation time. In real elastomers, the relaxation occurs over several orders of magnitude of time. A better model of viscoelasticity is so-called Prony series which consists of a spring and a series of Maxwell elements assembled in parallel.

One more factor of effect on friction of elastomer can be also considered – temperature. In the book of Popov and Heß [63], the method is described how the local heating in contacts can be taken into account in the framework of the MDR. During the contact between elastomer and rigid body, the energy loss by normal force on the elements (dashpots) of foundation must balance the heat energy flow which can be calculated with the formulation presented in the book.

With the help of analysis of fretting wear in the previous chapter, the problem of wear under gross slip can be also studied. In this case, tangential slip differently occurs at the whole contact area. During the sliding on rigid substrate the wear shape of elastic body can be calculated with the same principles of the MDR.

Appendix A Property of Oil Used in Experiment

The oil type in experiment is SHC XMP 320 [115]. It is widely used in wind turbine especially high load unit. The property is detailed in Table A.1.

Table A.1 Property of oil used in experiment

ISO Viscosity Grade	320
cSt @ 40º C	335
cSt @ 100º C	38.3
Viscosity Index, ASTM D 2270	164
Pour Point, ºC, ASTM D 97	-38
Flash Point, ºC, ASTM D 92	242
Specific Gravity @15.6º C kg/l, ASTM D 4052	0.860
Fail Stage	10
GFT-Class	High
FZG Scuffing, DIN 51345 (mod) A/16.6/90, Fail Stage	14+
4-Ball Wear test, ASTM D 4172, mm (Mod 1,800 RPM, 20kg, 54º C, 60 Minutes)	0.25
Rust protection, ASTM D665, Sea Water	Pass
Water Seperability, ASTM D 1401,Time to 40/37/3 at 82º C, minutes	10
Foaming Characteristics, ASTM D 892,Seq. II, Tendency/Stability, ml/ml	0/0

Appendix B Solution of EHL for Line Contact

During the study of mixed lubrication in Chapter 5, we tried also to numerically solve the EHL contact. In this Appendix we present the short fundamentals. Ertel was the first one who combined the Reynolds Equation and Hertzian Contact theory and predicted the EHL oil film thickness between two rollers in1939 [116] [117]. In his approximate theory the surfaces are assumed to be parallel and a reduced pressure was employed so that the one-dimensional Reynolds equation is independent on the viscosity of lubricant. Later other researchers, Dowson and Higginson (1959, 1966) [118] [119], Houpert and Hamrock (1986) [120] and so on, developed other approaches to solve the complex EHL problem and found a more accurate solution.

B.1 Basic equations

Reynolds equation describes the relation between pressure distribution and film thickness as a function of lubricant viscosity, density and velocity in the regime of hydrodynamic lubrication. The standard form of Reynolds equation for line contact is expressed as

$$\frac{\mathrm{d}}{\mathrm{d}x}\left(\frac{\rho h^3}{\eta}\frac{\mathrm{d}p}{\mathrm{d}x}\right)=12u\frac{\mathrm{d}(\rho h)}{\mathrm{d}x}, \tag{B.1}$$

with x coordinate, h film thickness, p pressure, u the sum velocity of both surfaces in x directions, ρ lubricant density, η absolute viscosity of lubricant. In order to solve Reynolds equation, the following two boundary condition and load balance must be met: firstly, pressure and pressure derivative are zero at the edges of contact area

$$p=\frac{\partial p}{\partial x}=0\Big|_{x=x_{in},x_{out}}; \tag{B.2}$$

secondly, the integration of pressure over the whole contact area is equal to external normal force

$$F=\int p dx\,. \tag{B.3}$$

It is not easy to obtaine an analytical solution of Eq. (B.1), while two further characters, elastic deformation of contacting surfaces and pressure-viscosity effect, play an important role to high pressure on the contact area. We list these equations of

pressure - viscosity $\eta=\eta_0 e^{\alpha p}$; (B.4)

viscosity - temperature $\eta=\eta_0\exp\left[-\beta\left(T-T_0\right)\right]$; (B.5)

$$\text{density - pressure } \rho = \rho_0 \left(1 + \frac{0.6 \times 10^{-9} p}{1 + 1.7 \times 10^{-9} p} \right), \tag{B.6}$$

where η_0 is viscosity at atmosphere pressure and temperature T_0, α pressure-viscosity coefficient, β viscosity-pressure coefficient, ρ_0 density at atmosphere pressure.

The surfaces of an elastic cylinder and a rigid plane are separated by the lubricant film and the distance between them compose of the geometrical separation and the elastic deformation of cylinder as seen in Fig. B.1.

Under the assumption that the contact area is much smaller than the radius of cylinder, the geometrical gap can be simplified as

$$h(x) \approx h_0 + \frac{x^2}{2R}. \tag{B.7}$$

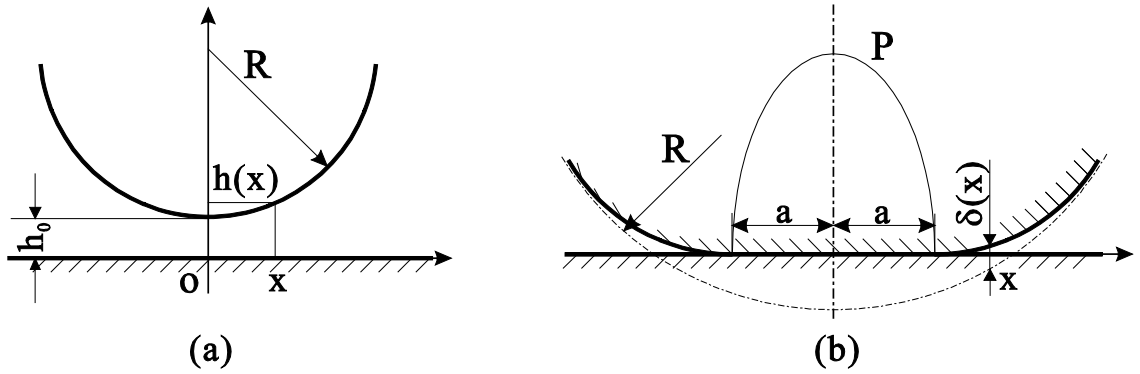

Fig. B.1 (a) Geometrical distance and (b) elastic deformation between a cylinder and a plane.

According to Hertz contact theory, the elastic deformation at point x is calculated as

$$\delta(x) = -\frac{2}{\pi E} \int_{s_1}^{s_2} p(s) In(x-s)^2 \, ds. \tag{B.8}$$

Together with (B.7) and(B.8), the oil film thickness between an elastic cylinder and an rigid plane is

$$h(x) = h_0 + \frac{x^2}{2R} - \frac{2}{\pi E} \int_{s_1}^{s_2} p(s) In(x-s)^2 \, ds. \tag{B.9}$$

Considering all the effects (B.4) - (B.6) and (B.9), with the boundary condition (B.2) and (B.3), the Reynolds equation can be solved numerically.

B.2 Numerical solution

For the simplification of analysis, the following dimensionless parameters are often proposed:

Load parameter : $W = \dfrac{w}{ERL}$ (B.10)

Speed parameter : $U = \dfrac{u\eta_0}{ER}$ (B.11)

Material parameter : $G = \alpha E$ (B.12)

Film thickness : $H = \dfrac{hR}{a^2}$. (B.13)

Thus the dimensionless film thickness can thus be written as a function of the three parameters

$$H = f\left(W, U, G\right). \tag{B.14}$$

With definitions of the other dimensionless parameters $P = \dfrac{p}{p_0}$, $X = \dfrac{x}{a}$, $\overline{\eta} = \dfrac{\eta}{\eta_0}$, $\overline{\rho} = \dfrac{\rho}{\rho_0}$, the basic equations in dimensionless form are written as following.

a. Reynolds equation (B.1)

$$\frac{d}{dX}\left(\frac{\overline{\rho}H^3}{\overline{\eta}}\frac{dP}{dX}\right) = \frac{3}{4}\frac{\pi^2 U}{W^2}\frac{d\left(\overline{\rho}H\right)}{dX} \tag{B.15}$$

with boundary condition: $P = \dfrac{\partial P}{\partial X} = 0\Big|_{X=X_{in},X_{out}}$.

b. Load balance (B.3)

$$\int P dX = \frac{\pi}{2}. \tag{B.16}$$

c. Lubricant viscosity (B.4)

$$\overline{\eta} = e^{\alpha p_0 P}, \tag{B.17}$$

d. Lubricant density

$$\overline{\rho} = 1 + \frac{0.6\times10^{-9} p_0 P}{1 + 1.7\times10^{-9} p_0 P}. \tag{B.18}$$

e. Film thickness (B.9)

$$H\left(X\right) = H_0 + \frac{1}{2}X^2 - \frac{1}{2\pi}\int_{S_1}^{S_2} P\left(S\right) In\left(X - S\right)^2 dS. \tag{B.19}$$

The elastic deformation $\overline{\delta}\left(X\right)$ in discrete form can be calculated numerically as

$$\overline{\delta_i} = -2\sum_{j=1}^{N} K_{ij} P_j , \tag{B.20}$$

With matrix

$$K_{ij} = \left(X_{i+0.5} - X_j\right)\left(\ln\left|X_{i+0.5} - X_j\right| - 1\right) - \left(X_{i-0.5} - X_j\right)\left(\ln\left|X_{i-0.5} - X_j\right| - 1\right)$$
$$= \Delta X \cdot \left\{(i-j+0.5)\left[\ln\left(\left|i-j+0.5\right| \cdot \Delta X\right) - 1\right] - (i-j-0.5)\left[\ln\left(\left|i-j-0.5\right| \cdot \Delta X\right) - 1\right]\right\}.$$

Observe from Reynolds equation that ρ , η and h have an influence on pressure. Normally the lubricant density changes not much with pressure, maximum by 33%, in some simulations its influence was neglected. But viscosity varies by several orders of magnitude as lubricant through the contact area, and h^3 in equation lets the pressure be very sensitive to variation of film thickness. For these reasons it is difficult to get convergence of solution and more and more accurate numerical methods were developed, for example Forward Iterative method [121], Inverse Solution method [122], Newton-Raphson method, Multigrid method [123] and Effective Influence Newton method [124] [125]. The main procedures of numerical simulation with these methods are shown in Fig. B.2.

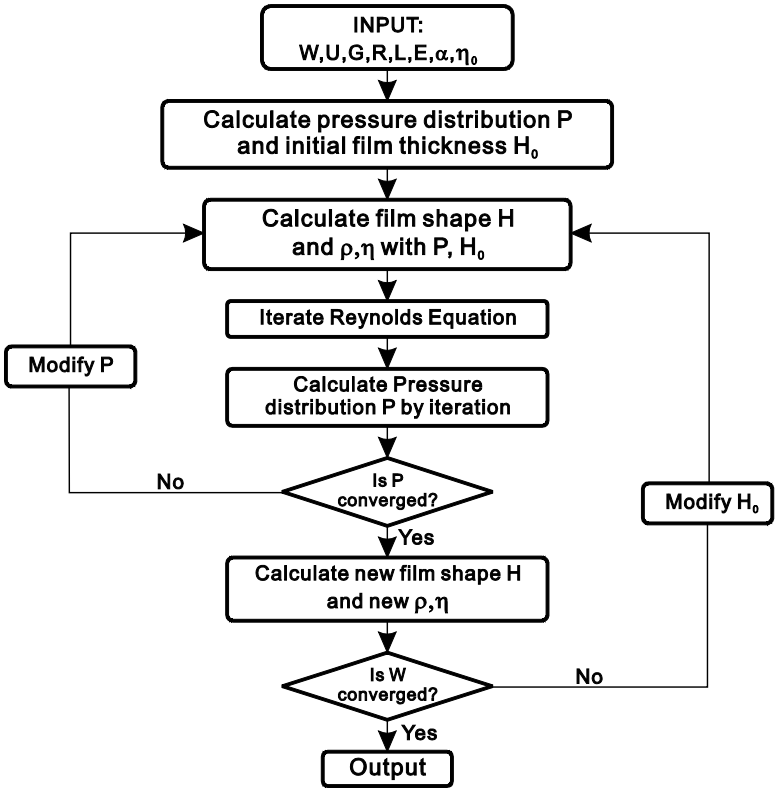

Fig. B.2 Flow chart of program.

Using Newton-Raphson method we programmed EHL line contact in Matlab. Fig. B.3 is the result for one case. From that It is found that oil film thickness h_0 over the Hertzian area is not constant, it is almost uniform but at the outlet edge has a decrease, the minimal thickness h_{min} is about 75% of central thickness h_0, where the pressure rises abruptly. These two EHL typical characters, thickness decrease and pressure spike at the outlet, were also proved by many experiment.

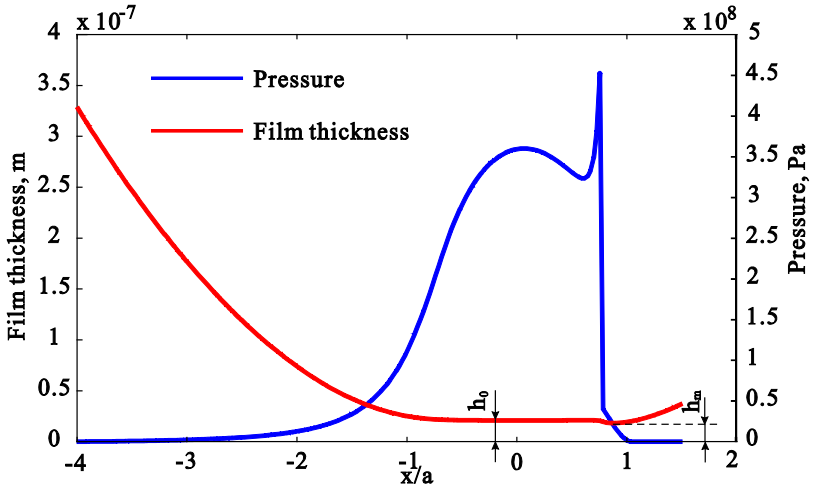

Fig. B.3 Film thickness and pressure distribution for EHL line contact.

(a) Formulas of film thickness

From curve fitting of many groups of numerical results, the formula of dimensionless film thickness as a function of dimensionless load, speed and material parameter was proposed by many researchers, such as Dowson-Higginson, Wymer and Hamrock-Jacobson etc. A widely used one set from Pan and Hamrock (1989) [107] is formulated as following:

Minimum film thickness in

$$\text{dimensionless form} \quad H_{\min} = \frac{h_{\min}}{R} = 1.714 W^{-0.128} U^{0.694} G^{0.568} \tag{B.21}$$

$$\text{dimensional form} \quad h_{\min} = \frac{1.806 \alpha^{0.568} (\eta_0 u)^{0.694} R^{0.434}}{(w/L)^{0.128}} \tag{B.22}$$

Central film thickness in

$$\text{dimensionless form} \quad H_0 = \frac{h_0}{R} = 2.929 W^{-0.166} U^{0.692} G^{0.470} \tag{B.23}$$

$$\text{dimensional form} \quad h_0 = \frac{2.992 \alpha^{0.470} (\eta_0 u)^{0.692} R^{0.474}}{(w/L)^{0.166} E^{0.056}} \tag{B.24}$$

From these relations above it can be seen noted that the film thickness is significantly affected by rotation speed and viscosity of lubricant, but slightly by load, and the elasticity effect is very weak. The film thickness is almost uniform over the Hertzian contact area. The area of decrease of thickness is very small and so that it was neglected in our simulation.

Reference

[1] Dimaki, A. V., Dmitriev, A. I., Chai, Y. S. & Popov, V. L. Rapid Simulation Procedure for Fretting Wear on the basis of the method of dimensionality reduction. *Int. J. Solids Struct*. (2014).

[2] Johnson, K. L. *Contact Mechanics*. (Cambridge University Press, Cambridge, 1985).

[3] Hertz, H. Über die Berührung fester elastischer Körper. *J. für die reine und Angew. Math*. 92, 156–171 (1882).

[4] Johnson, K. L., Kendall, K. & Roberts, A. D. Surface energy and the contact of elastic solids. *Proc. R. Soc. London A*. 324, 301–313 (1971).

[5] Derjaguin, B., Muller, V. & Toporov, Y. Effect of contact deformation on the adhesion of particles. *J. Colloid Interface Sci*. 53, 314–326 (1975).

[6] Tabor, D. The hardness of solids. *J. Colloid Interface Sci*. 58, 145–179 (1977).

[7] Maugis, D. Adhesion of spheres: The JKR-DMT transition using a Dugdale model. *J. Colloid Interface Sci*. 150, 243–269 (1992).

[8] Bhushan B. *Introduction to tribology*. (Wiley, New York, 2002).

[9] Dowson, D. *History of Tribology*. (Wiley, New York, 1998).

[10] Popov, V. L. *Contact Mechanics and Friction: Physical Principles and Applications*. (Springer-Verlag, Berlin, 2010).

[11] Li, Q. et al. Friction between a viscoelastic body and a rigid surface with random self-affine roughness. *Phys. Rev. Lett*. 111, 034301 (2013).

[12] Popov, V. L., Lars, V., Li, Q., Chai, Y. S. & Popov, M. Generalized law of friction between elastomers and differently shaped rough bodies. *Sci. Rep*. 4, 3750 (2014).

[13] Amontons, G. De la resistance cause dans les machines (About Resistance and Force in Machines). *Mem. l'Acedemie R. A*, 257–282 (1699).

[14] Coulomb, C. A. *Theorie des machines simple (theory of simple machines)*. (Bachelier, Paris, 1821).

[15] Bowden, F. P. & Tabor, D. *The Friction and Lubrication of Solids*. (Clarendon Press, Oxford, 1986).

[16] Archard, J. F. Elastic Deformation and the Laws of Friction. *Proc. R. Soc. London A* 243, 190–205 (1957).

[17] Ben-David, O. & Fineberg, J. Static Friction Coefficient Is Not a Material Constant. *Phys. Rev. Lett*. 106, 254301 (2011).

[18] Otsuki, M. & Matsukawa, H. Systematic Breakdown of Amontons' Law of Friction for an Elastic Object Locally Obeying Amontons' Law. *Sci. Rep*. 3, 1586 (2013).

[19] Rubinstein, S. M., Cohen, G. & Fineberg, J. Detachment fronts and the onset of dynamic friction. *Nature* 430, 1005–1009 (2004).

[20] Ben-David, O., Cohen, G. & Fineberg, J. The Dynamics of the Onset of Frictional Slip. *Science* (80-.). 330, 211–214 (2010).

[21] Amundsen, D. S., Scheibert, J., Thøgersen, K., Trømborg, J. & Malthe-Sørenssen, A. 1D Model of Precursors to Frictional Stick-Slip Motion Allowing for Robust Comparison with Experiments. *Tribol. Lett*. 45, 357–369 (2012).

[22] Greenwood, J. A. & Tabor, D. The friction of hard sliders on lubricated rubber – the importance of deformation losses. *Proc. Roy. Soc*. 71, 989–1001 (1958).

[23] Grosch, K. A. Relation between Friction and Visco-Elastic Properties of Rubber. *Proc. R. Soc. London, Ser. A, Math. Phys. Sci*. 274, 21–39 (1963).

[24] Barquins, M. & Courtel, R. Rubber friction and rheology of viscoelastic contact. *Wear* 32, 133–150 (1975).

[25] Klüppel, M. & Heinrich, G. Rubber friction on self-affine road tracks. *Rubber. Chem. Technol*. 73, 578–606 (2000).

[26] Persson, B. N. J. Theory of rubber friction and contact mechanics. *J. Chem. Phys*. 115, 3840–3861 (2001).

[27] Schallamach, A. The load dependence of rubber friction. *Proc. Roy. Sic. London B*, 65, 657–661 (1952).

[28] Thurston, R. H. Friction and Lubrication-Determination of the Laws and Co-efficient of Friction by New Methods and with New Apparatus. *Trübner Co.,* Ludgate Hill, London (1879).

[29] Stribeck, R. Die wesentlichen Eigenschaften der Gleit- und Rollenlager. *Zeitschrift des Vereins Dtsch. Ingenieure* 36, 1341–1348 (1902).

[30] Gümbel, L. Das Problem der Lagerreibung. *Mitteilungsblatt des Berliner Bezirksvereins Dtsch. Ingenieure* 5, 87–104 and 109–120 (1914).

[31] Dowson, D. Transition to Boundary Lubrication from Elastohydrodynamic Lubrication. *ASME* 229–240 (1969).

[32] Wang, Y. S., Wang, Q. J., Lin, C. H. & Shi, F. H. Development of a Set of Stribeck Curves for Conformal Contacts of Rough Surfaces. *Tribol. Trans*. 49, 526–535 (2006).

[33] Li, Q. & Pohrt, R. Mixed and Boundary Lubrication in Rolling Contact: Experiment and Simulation. *FACTA Univ. Ser. Mech. Eng.* **11,** 123–131 (2013).

[34] Spikes, H. A. Miex lubrication - an overview. *Lubr. Sci*. 9, 221–253 (1997).

[35] Tallian, T. E. The theory of partial elastohydrodynamic contacts. *Wear* 21, 49–101 (1972).

[36] Johnson, K. L., Greenwood, J. A. & Poon, S. Y. A simple theory of asperity contact in elastohydro-dynamic lubrication. *Wear* 19, 91–108 (1972).

[37] Patir, N. & Cheng, H. S. Application of Average Flow Model to Lubrication Between Rough Sliding Surfaces. *ASME J. Lubr. Technol*. 101, 220–230 (1979).

[38] Zhu, D. & H. S. Cheng. Effect of Surface Roughness on the Point Contact EHL. *ASME J. Tribol*. 110, 32–37 (1988).

[39] Patir, N. & Cheng, H. S. An Average Flow Model for Determining Effects of Three-Dimensional Roughness on Partial Hydrodynamic Lubrication. *ASME J. Lubr. Technol*. 100, 12–17 (1978).

[40] Greenwood, J. A. & Tripp, J. H. The Contact of Two Nominally Flat Rough Surfaces. *Proc. Inst. Mech. Eng*. 185, 625–633 (1970).

[41] Jiang, X. F., Hua, D. Y., Cheng, H. S., Ai, X. L. & Lee, S. C. A Mixed Elastohydrodynamic Lubrication Model With Asperity Contact. *ASME J. Tribol*. 121, 481–491 (1999).

[42] Wang, W. Z., Liu, Y. C., Wang, H. & Hu, Y. Z. A Computer Thermal Model of Mixed Lubrication in Point Contacts. *ASME J. Tribol*. 126, 162–170 (2004).

[43] Reye, T. Zur Theorie der Zapfenreibung. *Der Civil*. 4, 235–255 (1860).

[44] Archard, J. F. Contact and Rubbing of Flat Surfaces. *J. Appl. Phys*. 24, 981–988 (1953).

[45] Khrushchov, M. M. & Babichev, M. A. Investigation of wear of metals. *Russ. Acad. Sci*. (1960).

[46] Archard, J. F., Hirst, W. The Wear of Metals under Unlubricated Conditions. *Proc. R. Soc. Lond. A* 236, 397–410 (1956).

[47] Ko, P. L. Experimental Studies of Tube Frettings in Steam Generators and Heat Exchangers. *J. Press. Vessel Technol*. 101, 125–133 (1979).

[48] Fisher, N. J., Chow, A. B. & Weckwerth, M. K. Experimental Fretting Wear Studies of Steam Generator Materials. *J. Press. Vessel Technol*. 117, 312–320 (1995).

[49] Lee, C. Y., Tian, L. S., Bae, J. W. & Chai, Y. S. Application of influence function method on the fretting wear of tube-to-plate contact. *Tribol. Int*. 42, 951–957 (2009).

[50] Collier, J. P. et al. Mechanicsms of Failure of modular prostheses. *Clin. Orthop. Relat. Res*. 285, 129–139 (1992).

[51] Antler, M. Survey of contact fretting in electrical connectors. *Components, Hybrids, Manuf. Technol*. 8, 87–104 (1985).

[52] Rajasekaran, R. & Nowell, D. Fretting fatigue in dovetail blade roots: Experiment and analysis. *Tribol. Int*. 39, 1277–1285 (2006).

[53] Ciavarella, M. & Demelio, G. A review of analytical aspects of fretting fatigue, with extension to damage parameters, and application to dovetail joints. *Int. J. Solids Struct*. 38, 1791–1811 (2001).

[54] Popov, V. L. & Psakhie, S. G. Numerical simulation methods in tribology. *Tribol. Int*. 40, 916–923 (2007).

[55] Geike, T. & Popov, V. L. Mapping of three-dimensional contact problems into one dimension. *Phys. Rev. E*. 76, 036710 (2007).

[56] Geike, T. & Popov, V. L. Reduction of three-dimensional contact problems to one-dimensional ones. *Tribol. Int*. 40, 924–929 (2007).

[57] Heß, M. On the reduction method of dimensionality: the exact mapping of axisymmetric contact problems with and without adhesion. *Phys. Mesomech*. 15, 264–269 (2012).

[58] Heß, M. *Über die exakte Abbildung ausgewählter dreidimensionaler Kontakte auf Systeme mit niedrigerer räumlicher Dimension*. (Cuvillier Verschlag, Göttingen, 2011).

[59] Pohrt, R. & Popov, V. L. Contact stiffness of randomly rough surfaces. *Sci. Rep*. 3, 3293 (2013).

[60] Popov, V. L. Analytic solution for the limiting shape of profiles due to fretting wear. *Sci. Rep*. 4, 3749 (2014).

[61] Li, Q., Dimaki, A. V., Popov, M., Psakhie, S. G. & Popov, V. L. Kinetics of the coefficient of friction of elastomers. Accepted. *Sci. Reports* (2014).

[62] Li, Q., Filippov, A. E., Dimaki, A. V., Chai, Y. S. & Popov, V. L. Simplified simulation of fretting wear using the method of dimensionality reduction. *Phys. Mesomech.* 17 (2014).

[63] Popov, V. L. & Heß, M. *Methode der Dimensionsreduktion in Kontaktmechanik und Reibung. Eine Berechnungsmethode im Mikro- und Makrobereich*. (Springer, Berlin, 2013).

[64] Popov, V. L. & Heß, M. *Method of Dimensionality Reduction in Contact Mechanics and Friction*. (Springer, Berlin, 2014).

[65] Popov, V. L. & Heß, M. Method of Dimensionality Reduction in Contact Mechanics and Friction: a User's Handbook. I. Axially-symmetric Contacts. *Facta Univ. Ser. Mech. Eng*. 12, 1–14 (2014).

[66] Popov, V. L. Basic ideas and applications of the method of reduction of dimensionality in contact mechanics. *Phys. Mesomech*. 15, 254–263 (2012).

[67] Zhang, S. W. *Tribology of Elastomers*. (Elsevier Science, 2004).

[68] Pohrt, R., Popov, V. L. & Filippov, A. E. Normal contact stiffness of elastic solids with fractal rough surfaces for one- and three-dimensional systems. *Phys. Rev. E*. 86, 026710 (2012).

[69] Le Gal, A., Yang, X. & Klüppel, M. Evaluation of sliding friction and contact mechanics of elastomers based on dynamic-mechanical analysis. *J. Chem. Phys*. 123, 014704 (2005).

[70] Lee, E. H. Stress Analysis in Viscoelastic Bodies. *Quart. Appl. Math*. 13, 183–190 (1955).

[71] Radok, J. R. M. Visco-elastic stress analysis. *Quart. Appl. Math*. 15, 198–202 (1957).

[72] Kürschner, S. & Popov, V. L. Penetration of self-affine fractal rough rigid bodies into a model elastomer having a linear viscous rheology. *Phys. Rev. E.* 87, 042802 (2013).

[73] Argatov, I. I. & Sabina, F. J. Spherical indentation of a transversely isotropic elastic half-space reinforced with a thin layer. *Int. J. Eng. Sci*. 50, 132–143 (2012).

[74] Gao, H. J., Chiu, C. H. & Lee, J. Elastic contact versus indentation modeling of multi-layered materials. *Int. J. Solids Struct*. 29, 2471–2492 (1992).

[75] Popov, V. L. Method of dimensionality reduction in contact mechanics: heterogeneous systems. *Phys. Mesomech*. 16, 97–104 (2013).

[76] Cattaneo, C. Sul contatto di due corpi elastici: distribuzione locale degli sforzi. *Rend. dell Accad. Naz. dei Lincei*. 27, 342–348. 434–436, 474–478. (1938).

[77] Mindlin, R. D. Compliance of elastic bodies in contact. *J. Appl. Mech*. 16, 259–268 (1949).

[78] Ciavarella, M. The generalized Cattaneo partial slip plane contact problem. I—Theory. *Int. J. Solids Struct*. 35, 2349–2362 (1998).

[79] Grzemba, B., Pohrt, R., Teidelt, E. & Popov, V. L. Maximum micro-slip in Tangential Contact of randomly rough self-affine surfaces. *Wear* 309, 256–258 (2014).

[80] Rheological measurements were carried out by Ther-moplastics Testing Center of UL International TTC GmbH.

[81] Persson, B. N. J. *Sliding Friction. Physical Principles and Applications*. (Springer, Berlin, 2000).

[82] Dieterich, J. H. Time Dependent Friction and the Mechanics of Stick-Slip. *Pure Appl. Geophys*. 116, 790–806 (1978).

[83] Dieterich, J. H. Modeling of rock friction: 1. Experimental results and constitutive equations. *J. Geophys. Res. Solid Earth* 84, 2161–2168 (1979).

[84] Rice, J. R. & Ruina, A. L. Stability of Steady Frictional Slipping. *J. Appl. Mech*. 50, 343–349 (1983).

[85] Marone, C. Laboratory-derived friction laws and their application to seismic faulting. *Annu. Rev. Earth Planet. Sci*. 26, 643–696 (1998).

[86] Dieterich, J. H. & Kilgore, B. D. Direct observation of frictional contacts: New insights for state-dependent properties. *Pure Appl. Geophys*. 143, 283–30 (1994).

[87] Baumberger, T., Caroli, C., Perrin, B. & Ronsin, O. Nonlinear analysis of the stick-slip bifurcation in the creep-controlled regime of dry friction. *Phys. Rev. E*. 51, 4005 (1995).

[88] Baumberger, T. Contact dynamics and friction at a solid-solid interface: Material versus statistical aspects. *Solid State Commun*. 102, 175–185 (1997).

[89] Popov, V. L., Grzemba, B., Starcevic, J. & Popov, M. Rate and state dependent friction laws and the prediction of earthquakes: What can we learn from laboratory models? *Tectonophysics* 532-535, 291–300 (2012).

[90] Dieterich, J. H. & Kilgore, B. D. Imaging surface contacts: Power law contact distributions and contact stresses in quartz, calcite, glass and acrylic plastic. *Tectonophysics* 256, 219–239 (1996).

[91] Müser, M. H., Urbakh, M. & Robbins, M. O. Statistical Mechanics of Static and Low-Velocity Kinetic Friction. *Adv. Chem. Phys*., Ed. by Prigogine I., Rice S.A., 126, (2003).

[92] Baumberger, T., Berthoud, P. & Caroli, C. Physical analysis of the state- and rate-dependent friction law. II. Dynamic friction. *Phys. Rev. B* 60, 3928 (1999).

[93] Ostermeyer, G. P. On the dynamics of the friction coefficient. *Wear* 254, 852–858 (2003).

[94] Ostermeyer, G. P. & Müller, M. Dynamic interaction of friction and surface topography in brake systems. *Tribol. Int*. 39, 370–380 (2006).

[95] Popov, V. L. Thermodynamics and kinetics of shear-induced melting of a thin layer of lubricant confined between solids. *Tech. Phys*. 46, 605–615 (2001).

[96] Heslot, F., Baumberger, T., Perrin, B., Caroli, B. & Caroli, C. Creep, stick-slip, and dry-friction dynamics: Experiments and a heuristic model. *Phys. Rev. E*. 49, 4973 (1994).

[97] Rice, J. R., Lapusta, N. & Ranjith, K. Rate and state dependent friction and the stability of sliding between elastically deformable solids. *J. Mech. Phys. Solids* 49, 1865–1898 (2001).

[98] Filippov, A. E. & Popov, V. L. Modified Burridge–Knopoff model with state dependent friction. *Tribol. Int*. 43, 1392–1399 (2010).

[99] Popov, V. L. A theory of the transition from static to kinetic friction in boundary lubrication layers. *Solid State Commun*. 115, 369–373 (2000).

[100] Schargott, M. & Popov, V. L. Mechanismen von Stick-Slip- und Losbrech-Instabilitäten. *Tribol. und Schmierungstechnik* 5, 11–17 (2003).

[101] Canudas de Wit, C. & Ischinsky, P. Adaptive friction compensation with partially known dynamic friction model. *Int. J. Adapt. Control Signal Process*. 11, 65–80 (1997).

[102] Dupont, P., Hayward, V., Armstrong, B. & Altpeter., F. Single state elastoplastic friction models. *IEEE Trans. on, Autom. Control* 47, 787–792 (2002).

[103] Lampaert, V., Al-Bender, F. & Swevers, J. Experimental Characterization of Dry Friction at Low Velocities on a Developed Tribometer Setup for Macroscopic Measurements. *Tribol. Lett*. 16, 95–105 (2004).

[104] Popov, V. L., Starcevic, J. & Filippov, A. E. Influence of Ultrasonic In-Plane Oscillations on Static and Sliding Friction and Intrinsic Length Scale of Dry Friction Processes. *Tribol. Lett*. 39, 25–30 (2010).

[105] Filippov, A. E. & Popov, V. L. Fractal Tomlinson model for mesoscopic friction: From microscopic velocity-dependent damping to macroscopic Coulomb friction. *Phys. Rev. E*.2 75, 027103 (7AD).

[106] Braunovic, M., Konchits, V. V. & Myshkin, N. K. *Electrical Contacts Fundamentals, Applications and Technology*. (CRC Press, 2007).

[107] Pan, P. & Hamrock, B. J. Simple Formulas for Performance Parameters Used in Elasto-hydrodynamically Lubricated Line Contacts. *ASME J Tribol*. 111, 146–251 (1989).

[108] Popov, V. L. Method of reduction of dimensionality in contact and friction mechanics: A linkage between micro and macro scales. *Friction* 1, 41–62 (2013).

[109] Homola, A. M., Israelachvili, J. N., Gee, M. L. & McGuiggan, P. M. Measurements of and Relation Between the Adhesion and Friction of Two Surfaces Separated by Molecularly Thin Liquid Films. *J. Tribol*. 111, 675–682 (1989).

[110] Crook, A. W. Simulated Gear-Tooth Contacts: Some Experiments upon Their Lubrication and Subsurface Deformations. *Proc. Inst. Mech. Eng*. 171, 187–214 (1957).

[111] Jäger, J. Axi-symmetric bodies of equal material in contact under torsion or shift. *Arch. Appl. Mech*. 65, 478–487 (1995).

[112] Ciavarella, M. & Hills, D. A. Brief Note: Some observations on the Oscillating Tangential Forces and Wear in General Plane Contacts. *Eur. J. Mech. - A/Solids* 18, 491–497 (1999).

[113] Paggi, M., Pohrt, R. & Popov, V. L. Partial-slip frictional response of rough surfaces. *Sci. Rep*. 4, 5178 (2014).

[114] Wetter, R. & Popov, V. L. Shakedown limits for an oscillating, elastic rolling contact with Coulomb friction. *Int. J. Solids Struct*. 51, 930–935 (2014).

[115] www.mobil.com/USA-English/Lubes/PDS/GLXXENINDMOMobilgear_SHC_XMP.aspx?Print=yes

[116] Ertel, A. M. Hydrodynamic lubrication based on new principles. *Appl. Math. Mech*. 3, 41–49 (1939).

[117] Popova, E. & Popov, V. L. On the history of elastohydrodynamics: The dramatic destiny of Alexander Mohrenstein-Ertel and his contribution to the theory and practice of lubrication. *J. Appl. Math. Mech*. (2014).

[118] Dowson, D. & Higginson, G. R. A Numerical Solution to the Elastohydrodynamic Problem. *J. Mech. Eng. Sci*. 1, 6–15 (1959).

[119] Dowson, D. & Higginson, G. R. *Elasto-hydrodynamic lubrication: the fundamentals of roller and gear lubrication*. (Pergamon Press, 1966).

[120] Houpert, L. G. & Hamrock, B. J. Fast Approach for Calculating Film Thicknesses and Pressures in Elastohydrodynamically Lubricated Contacts at High Loads. *J. Tribol*. 108, 411–419 (1986).

[121] Mostofi, A. & Gohar, R. Oil Film Thickness and Pressure Distribution in Elastohydrodynamic Point Contacts. *J. Mech. Eng. Sci.* **24,** 173–182 (1982).

[122] Dowson, D. & Whitaker, A. V. A Numerical Procedure for the Solution of the Elastohydrodynamic Problems of Rolling and Sliding Contacts Lubricated by a Newtonian Fluid. *Proc. Inst. Mech. Eng*. 180, 57–71 (1965).

[123] Lubrecht, A. A. The numerical solution of the elastohydrodynamically lubricated line- and point contact problem, using multigrid techniques. (1987).

[124] Dowson, D. & Wang, D. An analysis of the normal bouncing of a solid elastic ball on an oily plate. *Wear* 179, 29–37 (1994).

[125] Jalali Vahid, D. Transient analysis of ehd point contacts. (2000).